Delft University of Technology

Local coupling of charge and polymer dynamics

van Eijck, L

Publication date
2006

Document Version
Final published version

Citation (APA)
van Eijck, L. (2006). *Local coupling of charge and polymer dynamics*. [Dissertation (TU Delft), Delft University of Technology].

Important note
To cite this publication, please use the final published version (if applicable).
Please check the document version above.

Copyright
Other than for strictly personal use, it is not permitted to download, forward or distribute the text or part of it, without the consent of the author(s) and/or copyright holder(s), unless the work is under an open content license such as Creative Commons.

Takedown policy
Please contact us and provide details if you believe this document breaches copyrights.
We will remove access to the work immediately and investigate your claim.

This work is downloaded from Delft University of Technology.
For technical reasons the number of authors shown on this cover page is limited to a maximum of 10.

Local Coupling of Charge and Polymer Dynamics

Local Coupling of Charge and Polymer Dynamics

PROEFSCHRIFT

ter verkrijging van de graad van doctor
aan de Technische Universiteit Delft,
op gezag van de Rector Magnificus Prof.dr.ir. J.T. Fokkema,
voorzitter van het College voor Promoties
in het openbaar te verdedigen op dinsdag 28 februari 2006 om 15.30 uur

door

Lambert VAN EIJCK

HBO-ingenieur Technische Natuurkunde
geboren te Tilburg

Dit proefschrift is goedgekeurd door de promotor:
Prof. dr. G.J. Kearley

Samenstelling promotiecommissie:

Rector Magnificus	voorzitter
Prof. dr. G.J. Kearley	Technische Universiteit Delft, promotor
Prof. dr. J. -L. Sauvajol	Université Montpellier II
Prof. dr. S. J. Picken	Technische Universiteit Delft
Prof. dr. S. W. de Leeuw	Technische Universiteit Delft
Prof. dr. L. D. A. Siebbeles	Technische Universiteit Delft
Prof. dr. I. M. de Schepper	Technische Universiteit Delft
Dr. M.R. Johnson	Institut Laue-Langevin, France

Copyright © 2006 by L. van Eijck

All rights reserved. No part of the material protected by this copyright notice may be reproduced or utilized in any form or by any means, electronic or mechanical, including photocopying, recording or by any information storage and retrieval system, without permission from the publisher: MES Grafische Bedrijven, Capelle aan den Ijssel.

Printed in the Netherlands

Contents

1 Introduction **1**
- 1.1 The demand for mobile energy . . . 1
- 1.2 Conducting polymers as solar cell materials . . . 3
  - 1.2.1 Overview of solar cells . . . 3
  - 1.2.2 Conducting polymers . . . 4
  - 1.2.3 Aim of this work . . . 5
  - 1.2.4 Approach . . . 7
- 1.3 Battery materials . . . 8
  - 1.3.1 History of batteries . . . 8
  - 1.3.2 Principle of the Li battery . . . 9
  - 1.3.3 Aim of this work . . . 11
  - 1.3.4 Approach . . . 12

2 Theory and methods **15**
- 2.1 Dynamics . . . 15
  - 2.1.1 Molecular vibrations . . . 16
  - 2.1.2 Molecular dynamical correlations . . . 17
- 2.2 Neutron scattering theory . . . 18
- 2.3 Modelling . . . 21
  - 2.3.1 Ab initio . . . 21
  - 2.3.2 Molecular dynamics . . . 25

3 Instrumental **27**
- 3.1 Direct geometry . . . 28
  - 3.1.1 IN5 . . . 29
- 3.2 Inverted geometry instruments . . . 29
  - 3.2.1 TOSCA . . . 30
  - 3.2.2 IRIS . . . 31

I Conducting Polymers **33**

4 INS as a probe of inter-monomer angles in polymers **37**
- 4.1 Introduction . . . 37
- 4.2 Computational . . . 38
- 4.3 Results and discussion . . . 39

4.4 Conclusions 41

5 Intermolecular Interactions in Bithiophene 43
5.1 Introduction 43
5.2 Density Functional Theory Vibrational Calculations 44
5.3 Results and Discussion 46
    5.3.1 Isolated Molecule Vibrations 46
    5.3.2 Periodic Model Vibrations 46
    5.3.3 Dispersion of Vibrations 47
    5.3.4 Rotational Potentials 49
    5.3.5 Directional Interactions in the Solid State 51
5.4 Conclusions 53

6 Signatures of intramolecular disorder in thiophenes 55
6.1 Introduction 55
6.2 Bithiophene cell parameters 55
6.3 Vibrational consequences of disorder 59

7 Charge transfer between thiophene rings in vibrationally excited states 65
7.1 Introduction 65
7.2 Experimental and methods 66
7.3 Discussion 67
7.4 Conclusions 68

8 Charge transfer and condensed phase dynamics 69
8.1 Introduction 69
8.2 Methods and computations 70
8.3 Discussion 71
    8.3.1 QENS and INS versus MD 71
    8.3.2 Charge transfer integral versus INS 72

II Polymer Electrolytes 77

9 The effect of nanoparticles on ionic interactions 83
9.1 Introduction 83
9.2 Experimental 85
9.3 Computational 85
9.4 Results and Discussion 86
9.5 Conclusions 92

10 Softening of the potential-energy surface on the addition of nanoparticles 93
10.1 Introduction 94
10.2 Methodology and Experiments 96
10.3 Experimental results 97
10.4 Discussion 98

10.5 Rotational dynamics 100
10.6 Extrapolation of barrier heights 101
10.7 Conclusions 102

11 Conclusions 107
11.1 Conducting polymers 107
11.2 Polymer electrolytes 109

Appendices 115

A Summary 117

B Samenvatting 121

C Dankwoord 125

D Curriculum Vitae 127

E List of Publications 129

Glossary 131

Chapter 1

Introduction

The introduction of polymers (plastic) in electrical and electronic devices as charge carrying media is on the verge of commercial exploitation. Polymers can be well tailored to meet the demands for many applications. In this chapter we address two such applications termed *conducting polymers* and *polymer electrolytes*. Of these two classes of polymers one can build "plastic electronics" or fuel cell membranes respectively, but here their properties are explained with regard to the application as (respectively) solar cell materials and battery materials. To fully exploit the benefits these polymers have, and possibly to tailor them to the specific demands of their applications, a thorough understanding is needed of the underlying principles on an atomic or even electronic level. Much scientific work has been performed, but different explanations are still debated. The essential difference with todays common use of polymers is that these new polymers are electric charge carrying, where polymers conventially are used as charge isolators.

Before going into the details of the charge transport in these types of polymers and discussing the scientific efforts made (as will be done in part I and II) we use this chapter to give an overview of the applications to place our rather "specific" scientific contributions in a broader scheme.

1.1 The demand for mobile energy

With the growing global welfare the need for energy increases and the need for mobility increases. These two trends combined, one can expect as well an increasing demand for mobile energy i.e.: either an energy reserve that is easily transported or a means of generating/converting energy while moving. One of the most common sources of mobile energy is fossil fuel and its energy content is roughly 40 MJ/kg. As the reserves of fossil fuels run out, the search for alternatives intensifies, boosted by the environmental benefits of some of the alternatives over the fossil fuels [1]. Remarkably, the fossil fuels were never very popular as 'personal' energy sources, for applications that individuals would carry with them, despite the high energy density [§] (cf. Li-ion batteries have an energy content less than 1 MJ/kg) . Instead, most of these

---

[§] the exception being the cigarette lighter

applications are fed by an electrical current and as such the battery has been the most popular 'personal' mobile source of energy.
Recent years have shown an enormous growth of mobile personal applications like mobile phones, PDAs and laptop computers and with the continuing performance improvements, the demand for more energy content will increase.

Batteries

Among the solutions to this problem are polymer based batteries, due to the low specific weight, ease of production and flexibility. Part II starts with a short introduction in batteries, where we briefly address the use of polymers in the electrolyte of batteries. A major drawback of this type of electrolyte is its low electrical conductivity and much effort has been put in improving it. By the addition of nano structured inorganic materials Croce et al. [2] have shown an increase in the conductivity of several orders of magnitude. Although similar results have been obtained for different types of electrolytes and inorganic filler materials, the underlying mechanism responsible for the improvement is still under debate. In part II we address this phenomenon and the scientific efforts that have been made to understand it. Our approach to contribute to the understanding of the increased conductivity of the polymer electrolytes is via combined neutron scattering experiments and computations and computer simulations. Using inelastic neutron scattering, quasi-elastic neutron scattering, density functional theory calculations and molecular dynamics simulations, we explain the increased conductivity as a change in the average local interactions of the charge carrier (cation) that enables more cations to contribute to the current.

Solar Cells

Returning to the demand for more light-weight energy sources, one could think of solar cells as an alternative for batteries, or as a supplement to extend the operation cycle of the battery. Except for a restricted number of pocket calculators the conventional solar cell is not being used as such, with one of its deficits being its specific weight and cost (related to the inherent stringent production requirements). With the discovery of conducting polymers in the 1970s [3], a potential substitute for these conventional solar cells was found. Although the efficiency of these polymer based solar cell applications is still well below that of the conventional cell, the flexibility and ease of processing polymers in general might initiate the use of this type of flexible solar cells in mobile applications. The research in this field of materials science is boosted even more by the potential of these polymers to act as semiconductors for electronic devices. Again the performance is still well below that of conventional silicon based technology, but the benefits of low cost and ease of production [§] will open up possibilities for disposable electronics, that are not achievable at the moment. A very recent example of a commercial application is the flexible display based on solution-processed organic transistors by Philips [4] and organic thin-film electronics [5]. One other device is the organic light emitting diode (OLED) that too has found its use in commercial applications and operates on the reverse processes of a organic

---

[§] in solution these semiconducting polymers can be used to manufacture electronic devices with an inktjet-type printer

solar cell. In the diodes charge is injected to generate light upon recombination and the major difficulty is to stimulate this recombination. Oppositely, in solar cell the photo-generated exciton is dissociated with the help of materials of different electron affinity and the migration of the separated charges is of major concern.
Unlike conventional silicon based semiconductors, polymers are rather soft and consequently a charge on the chain will distort the local structure of the chain. The coupling between the charge and the polymer distortion implies that the charge mobility is significantly influenced by disorder in the system. In part I we concentrate on conformational disorder in models of conducting polymers using similar experimental and computational methods as described above.

1.2 Conducting polymers as solar cell materials

Light harvesting is not unique to man-made solar cells, but is the very basic mechanism behind plant growth called photosynthesis. The generation of an electrical current or potential from light is called photovoltaics and is quite different from photosythesis, though it is based on photoexcitation as well.

1.2.1 Overview of solar cells

To generate an electrical current from solar light the photon needs to create an excited state in the solar cell and this electrical potential energy needs to be transported to whatever device the solar cell is connect to. Quantum mechanics dictates that the photon energy should match the separation between the ground and excited state of the atom that absorbs the photon. In solids the atomic energy states transform to energy bands and the separation between the bands is called the band gap in case of semiconductors or insultating solids [§].
Conventional solar cells are built from a pair of semiconductors (*p*- and *n*- type) that generate a depletion zone when brought into contact (figure 1.1). When an excitation is generated (by light) in this zone, the intrinsic electric field in the zone separates the excited electron from its excitation site (the hole). In turn, both the hole and electron need to migrate to electric contacts of the solar cell.

The discovery of the photovoltaic effect dates back to 1839, when the French scientist Antoine-Cesar Becquerel observed that illumination of one of two electrodes in an electrolyte generates an electrical current. However, the efficiency was very low and the only purpose that was found for it (for a rather long time) was in light-measuring devices.
The first use of a solar cell as an power generating device was after Czochralski managed to build a silicon single crystal and the efficiency at that time was some 4%. The effort that needs to be made to build this type of cell is unfortunately too great for these cells to be economically attractive for many applications, with its efficiency of around 15 %. With the invention of the Grätzel cell [6] a new life began for the solar cell, as this type of cell can be built without the complications of clean-room conditions, that are indispensable in silicon technology. This type of cell separates

---

[§] The band gap is absent in metals

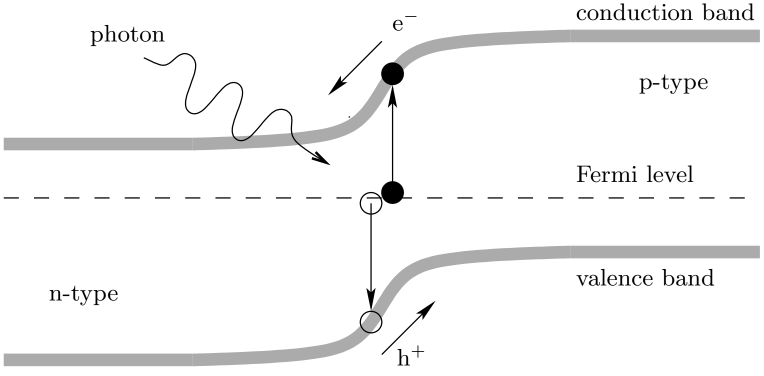

Figure 1.1: The principle of light harvesting in solar cells is the generation of an electron-hole pair by the absorption of a photon. The charge particles (the electron e^- and the hole h^+) are separated by an intrinsic electric field of the depletion region, depicted as a sloping electrical potential. Via the n and p-type semiconductors these charges are then lead to the solar cell electrodes.

the different functions that a solar cell performs, by dedicating the light harvesting to a dye, much like green plants do, and forcing the resultant excited state to dissociate, using a blend of different materials. The dye is dissolved in an electrolyte together with nanoparticulate TiO_2, where the latter absorbs an excited electron from the dye, thereby initiating the dissociation. The electrolyte, likewise, absorbs the hole of the dye and transports the positive charge to the opposite electrode. Electron transport takes place via contact pathways of the nanoparticles that thus need to take up a large volume fraction of the cell. The major benefits of the Grätzel cell with its large TiO_2 fraction is the resulting large internal surface area, where the exciton dissociation takes place. This type of cells, with an efficiency of around 10 % are comparatively easy to produce.

Derived from this type of cell is the polymer based solar cell. Here the electrolyte and the dye are replaced by a π-conjugated polymer that generates the exciton and transports the hole after exciton dissociation at the polymer-nanoparticle interface. In turn, the nanoparticle can be replaced by an electron-accepting polymer. One of the benefits of using polymers in solar cells is that by synthesis of side groups to the polymer backbone, its spectral sensitivity towards light harvesting can be tuned, and many attempts are being made to build efficient solar cells using polymers [7, 8, 9, 10].

1.2.2 Conducting polymers

The Nobel prize 2000 for Phyisics was awarded to Shirakawa, McDiarmid and Heeger for the discovery and the development of conducting polymers [11]. It was nearly thirty years before, in the 1970s, that the −accidental− discovery of conducting polymers was made by Shirakawa and colleagues: the conductivity of polymers with a particular electronic orbital structure ranges from the well known insulator regime of classical polymers, to conductivity values that almost equal that of copper! Polyacetylene was the first conducting polymer discovered by Shirakawa [3] and it possesses a conductivity that ranges over more than 14 orders of magnitude, depending on the concentration of the doping added. In the pristine state, conducting polymers will have a band gap comparable to the classical semiconductors that are used in modern electronic intergrated circuits. This band gap is a direct consequence of the Peierls distortion [§]: the polymer is a quasi-one dimensional chain that is more stable when the carbon atoms in the polymer backbone rearrange from equidistant atoms into closer pairs that repeat at twice the original periodic distance. Considering that polymers are relatively easy to produce, without the cumbersome requirements of a cleanroom environment, these polymers in the semi-conducting state are of specific interest as a substitute to the commonly used silicon based semiconductors. Since the discovery a lot of scientific effort is made in order to understand the fundamental differences between classical solid state semiconductors and conducting polymers. Much of the terminology and models are therefore borrowed from solid state physics, even though polymers are soft condensed matter. As an example, the generation of an electron-hole (e-h) pair in solar cells in classical semiconductors results in separation of the two opposite charges, where in the polymer the e-h pair binds as an exciton that does not yet contribute to the desired photo current. The processes that need to be considered for the conducting polymer in photovoltaic devices are thus not merely the generation of e-h pairs (excitons), but also the transport of excitons to a charge transfer complex, the subsequent e-h dissociation at the complex and the transport of the separated charge (i.e. the hole mobility when considering the polymer). The theoretical models that describe the latter transport are either coherent bandlike transport (derived from the solid state physics) or transport by charge tunneling or hopping. The transfer rate for the latter can then be calculated using the Marcus equation (see part section I) if the bandwidth of the electronic level is known of the particle (electron or hole) under consideration.

1.2.3 Aim of this work

After the photo-induction of an electron-hole pair and its transport and dissociation, the conductivity is determined by the charge carrier mobility. In solar cells the dynamics of the polymer chain will have a large impact on the polaron mobility, much like the effect of oligomers dynamics in plastic electronics. The synthesis of functional side chains to the polymer backbone impedes a proper crystallisation, and one should regard the determined charge transfer rates [12, 13] on idealized perfect crystals as an upper limit. The intermolecular and intramolecular charge transfer will be restricted by both static disorder due to crystal imperfections or poor crystallinity, and dynamic disorder at finite temperatures.

The effect of disorder is reported by Grozema et al. [14] as a deviation of the individual monomers on a chain from the chain planar structure, via the intermonomer dihedral angle. Their calculations are confirmed by mobility measurements on polythiophene (pT) and poly-phenylenevinylene (pPV) for which they claim the highest measure mobility of pPV to be caused by its planar rigidity. One may then expect the fluctuation of the intramolecular charge transfer to couple strongly to the normal modes of vibration that include the internal coordinate of the intermonomer dihedral.

[§] In the 1950s, long before the discovery of conducting polymers, Rudolf Peierls predicted that a 1 dimensional metal is an isolator or at best a semiconductor.

To investigate the coupling of the charge transfer to this and all other normal modes of vibration, we investigate the charge-transfer integral (CTI) with respect to the extreme conformations of these modes (chapter 7) using density functional theory (DFT) and then proceed with a more realistic model by including the neighbouring molecules. The molecular conformations are now determined from molecular dynamics (MD) simulations, after adaptation of the force-field parameters, and include the effect of neighbouring molecules.
To make these calculations tractable we choose polythiophene and its oligomers as a model system. In figure 1.2 we show the shorteeffect of only two thiophene monomers: bithiophene. Figure 1.3 shows the crystal structure of bithiophene, displayed along the common main axis of the molecules, in order to highlight the closest contacts between the individual molecules. Π-conjugated molecules often condense in a herringbone type crystal, similar to bithiophene (2T), and the intermolecular charge transfer in these materials is expected to depend strongly on the coupling neighbouring molecules as shown in figure 1.3. We find the corresponding bond path in chapter 5 and address vibrational modes that are concerned with this specific hydrogen in chapter 6.

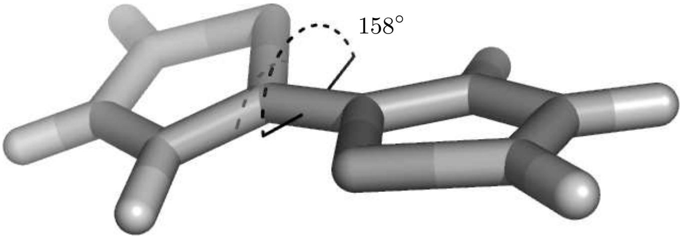

(a) The two pentagons (of one sulfur and four carbons) are twisted by 20−30° when the molecule is isolated from its environment. The corresponding electron orbital coupling between the rings will therefore be weakened, leading to reduced conductivity.

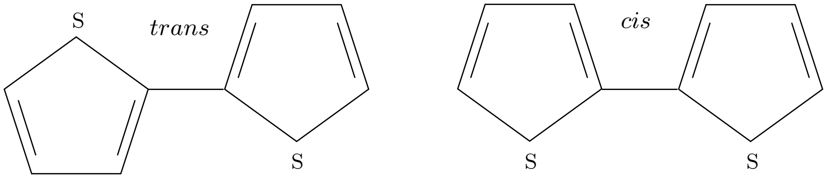

(b) Two minimum energy structures (*trans* and *cis*) of bithiophene.

Figure 1.2: The smallest oligomer of polythiophene consisting of two thiophene units: bithiophene.

The coupling in these type of materials via the hydrogens clearly demonstrates the need for a thorough investigation of the normal modes of vibration that are concerned with this specific hydrogen and it obviates the need inelastic neutron scattering (INS) that is particularly sensitive to hydrogen displacements (section 2.2).
To investigate the static disorder in these materials, we perform DFT vibrational calculations on a single molecule and in the crystalline state, that we compare with the INS spectra. We show the sensitivity of the normal modes to the intermonomer dihedral angle in chapter 4 and continue in chapter 6 to investigate the deviations from

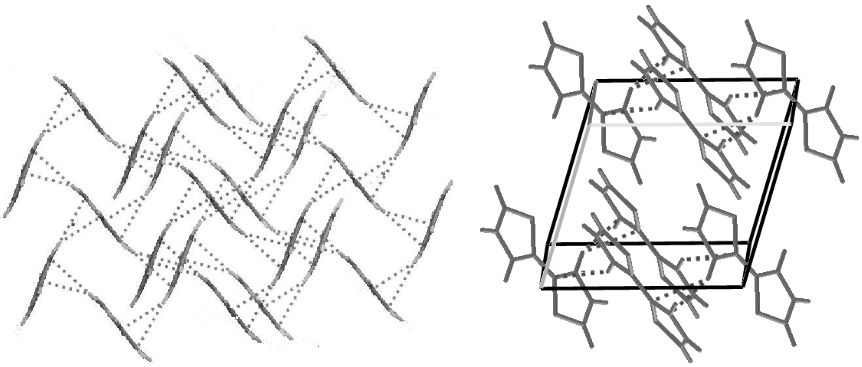

(a) The closest contact between bithiophene molecules as seen along the direction of both molecular planes

(b) One unit cell with bithiophene molecules and their closest contacts. The intermolecular contacts are related to the p_z orbitals on the carbon atoms.

Figure 1.3: Two views on the intermolecular closest contacts of bithiophene. In **(a)** the herring bone packing of the molecules is clearly shown and **(b)** shows which atoms are involved in an intermolecular contact: one hydrogen is in contact with two carbons of the neighbouring molecule.

the crystal structure, as apparent from our INS spectra. The calculated vibrational spectrum of polythiophene shows a rather remarkable agreement with the observed spectrum, when the consecutive monomers are oriented in a *cis* manner with sulfur atoms on the same side, rather than the XRD derived linear chains of *trans* oriented monomers.

1.2.4 Approach

First we determine the sensitivity of the DFT vibrational calculations to the intermonomer angle of thiophene based materials (chapter 4). To make these calculations tractable, we substitute the polymer with its oligomers: bithiophene (2T), quaterthiophene (4T). To improve the spectral agreement for the soft vibrational modes, we perform calculation on the crystal structure of 2T, and include the dispersion of phonons (chapter 5). The intermolecular bonding is analysed in terms of charge density bondpaths as described by Bader [15]. One of the difficulties of the DFT approach to incorporate the non-bonded dispersion interactions is shown in chapter 6, where we calculate the cell parameters at 0 K by DFT and show how sensitive the low energy vibrational modes are to these parameters. The higher energy modes above 600 cm^{-1} of 2T and pT are not well reproduced by the DFT calculation based on the crystal data. The alignment of neighbouring monomers with respect to each other appears to be responsible for the spectral agreement in this region, and from our finding we suggest possible disorder. The validity of this hypothesis was tested only very recently, and we discuss our findings.

In the next two chapters (7, 8) we address the effect of disorder on the CTI. The charge transfer is estimated by the calculation of the bandwidth of the higest occupied molecular orbital (HOMO). We estimate the bandwidth by calculating the splitting of the highest occupied level when two molecules (fragments) are brought into proximity. As the π orbitals of the molecules overlap, the new electronic states develop of which the energy levels depend on the constructive or destructive interference of the corresponding wavefunctions.

For bithiophene the CTI is determined "statically" from the conformational extremes of the molecule in each of its normal modes of vibration. These calculations suggest, that the effect of disorder should be accounted for in a more overall approach than by merely considering the intermonomer dihedral angle [14]. Thus we proceed in chapter 8 to calculate the dynamical disorder at finite temperatures by including the effect of neigbouring atoms in molecular dynamics simulations. These dynamics are again compared to observed INS spectra, and the coupling of the CTI to specific vibrational modes is presented.

1.3 Battery materials

Part II of this thesis concerns the molecular dynamics in the electrolyte of a battery, and how these dynamics influence the eventual performance of a battery. The subject is focussed on a study of the effect of nanoparticulate TiO_2 on the dynamics, and to put this research in a broader scheme, we present here a short overview of batteries in general, and continue to state the question that we address in this part of the thesis and our approach to find the answer.

1.3.1 History of batteries

At the end of 18^{th} century, many scientists were attracted to the unexplained forces that were collected under the term *electricity* while they were demonstrated in various famous experiments of that time. Among those scientists were Luigi Galvani and Allesandro Volta. One famous experiment on the muscle contraction of a frog leg with static electricity, was performed by Galvani himself and it made him conclude that he had discovered *animal electricity* [§]. His colleague and friend Alessandro Volta took up this theory at first, but while experimenting on the phenomenon, he became increasingly convinced that the observed electricity was not generated by the "biology" of the frog leg. One of his remarkable experiments involved a "setup" of four live humans:

[§] though the term *animal electricity* was also used in investigations around that time on the electricity generated by the torpedo fish and electric eel

Excerpt from a letter of Volta to Vassalli:

Four insulated individuals form a human chain, the first placing his finger on the tip of the second's tongue, the second likewise touching the uncovered eyeball of the third, and the third and fourth holding between them in their wet hands a freshly skinned and gutted frog. The first individual holds in his wet hand a sheet of zinc, the last a sheet of silver. When the metal sheets make contact, the electrical circuit is completed; the second individual immediately detects an acid taste on the tip of his tongue, a flash of light appears in the eye of the third individual and the leg of the frog convulses violently. In the words of Volta, "ecco dunque il fluido elettrico"!

Volta concluded that the frog leg, like the people in the chain, were not causing the electricity, but merely sensing or responding to it. He later showed that he could generate electricity too, by replacing the frog leg with an electrolyte. With that experiment he created the first electrical battery [§].
The battery was called a *voltaic pile* and it was for the first time that experiments could be done with a constant source of electricity. Because of that, it gave an enormous boost to the ongoing research on electricity and it sparked a new field in science now called electrochemistry.

1.3.2 Principle of the Li battery

The same principle of the voltaic pile by Volta based on two different metal electrodes holds for the operation of modern batteries. The battery delivers an electrical current to an external load, by generating an exactly balanced internal current of opposite charge through the electrolyte. This electrolyte should thus be an ionic conductor and an electronic insulator simultaneously. It also provides the connection between the two electrodes: the cathode and the anode. The source of energy of an electrical battery is a chemical potential: the cathode-anode-electrolyte system is brought out of its chemical equilibrium that can only be regained by creating an electrical current. In the classical example of a car battery (figure 1.4) the cathodes are lead plates and the anodes lead dioxide and the electrolyte is a diluted sulfuric acid. The chemical reactions at respectively the anode and the cathode are:

$$\begin{aligned} Pb(s) + {SO_4}^{2-}(aq) &\xrightarrow{discharge} PbSO_4 + 2e^- \\ PbO_2 + {SO_4}^{2-}(aq) + 4H^+ + 2e^- &\xrightarrow{discharge} PbSO_4 + 2H_2O. \end{aligned}$$

At full discharge both the cathode and the anode would be covered with $PbSO_4$ and the electrolyte would contain only water. This battery type is cheap to manufacture but relatively heavy (energy content 0.13 MJ/kg) and if one would replace the gasoline tank (approximately 40 MJ/kg) of a car with this type of energy storage, the vehicle would become too heavy. So as the fossil fuel reserves are running out, the search effort

---

[§] In Khujut Rabu, near Baghdad, a vessel was found just before WWII that is approx. 2000 year old, and it is suggestively named the *Baghdad Battery*. A replica has been built and it generates a voltage between 0.5 and 2 V, However, the application of the vessel as a battery has never been confirmed.

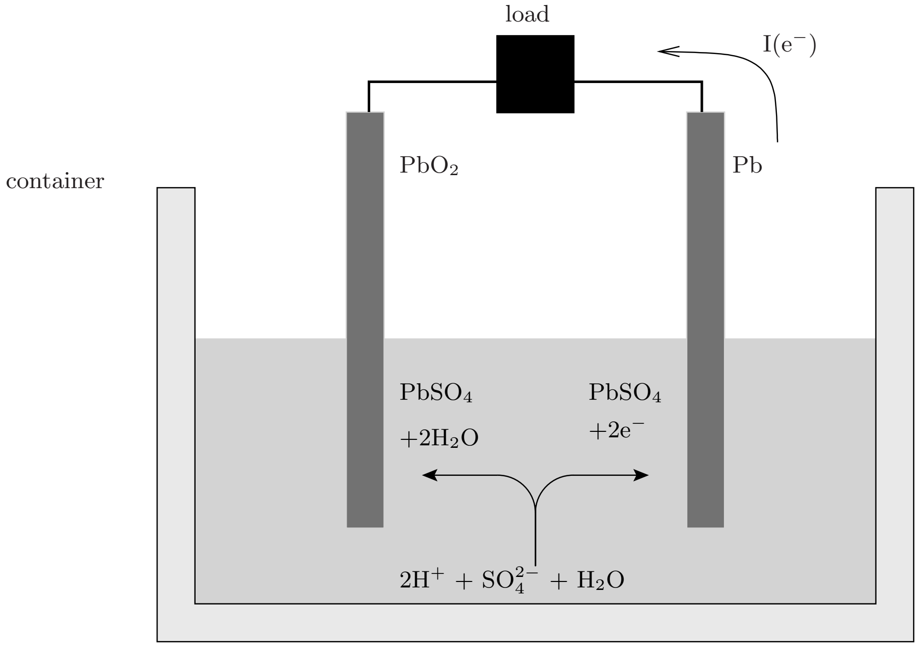

Figure 1.4: Principle of a lead acid battery. The SO_4^{2-} in the electrolyte depletes to form $PbSO_4$ as the battery is discharged to provide the load current.

for alternative energy storage methods increases and batteries are a viable option if the energy content per kilogram can be increased to compare with the energy density of fossil fuels. Although this goal is not yet achieved, lithium battery technology has improved the specific energy density of batteries significantly as lithium is the lightest metal and has the greatest electrochemical potential. The work on lithium batteries by G. N. Lewis dates from 1912, but it was much later (1970s) that the first commercial applications were produced, albeit that these batteries were not rechargeable. Because metallic lithium was used as an anode material these batteries had to be handled with caution, and since the 1990s these metallic lithium batteries are therefore replaced by lithium ion batteries. As an example of the chemistry involved in these type of batteries, below the chemical reactions during a discharge is shown for a lithium-ion CoO_2-C battery (resp. the anode and cathode):

$$\begin{aligned} Li_xC_6(s) &\xrightarrow{discharge} C_6 + Li^+ + e^- \\ Li_{1-x}CoO_2 + e^- + Li^+ &\xrightarrow{discharge} LiCoO_2 \end{aligned}$$

Apart from use in automotive applications, batteries are of great interest to the manufacturers of mobile electronic equipment, like cell phones and laptop computers. As these types of equipment are often in closer proximity to the consumer, compared to automotive applications, the demands on the battery concerning safety, heat production and temperature are more stringent. Still the energy density by mass should be high for these applications, while the size and shape flexibility should conform the (esthetic) design of the apparatus. In this respect the use of polymer-based solid electrolyte batteries could fulfill future demands of mobile consumer applications, as the polymer typically has a low specific mass, is easily tailored to meet the mechanical and processability requirements and has an elasticity that prolongs the lifetime of its contact area with the electrodes, as these undergo deformations or phase transformations during cycling. A solid polymer electrolyte consists of a (lithium) salt dissolved in a polymer that is in a solid or glassy state at operation temperature. The major drawback of polymer electrolytes is the poor ionic conductivity, which can be partly overcome by reducing the electrolyte thickness and increase the contact surface area. At the time of writing this thesis, the low conductivity of polymer electrolytes still hinders the commercial exploitation of polymer based all-solid lithium ion batteries. In general it can be said that the use of polymer electrolytes that solidify at room temperature inherently depresses the ionic conductivity, as ionic mobility is governed by the segmental mobility of the polymer host that ”propels” the ion through the polymer matrix. A compromise adaptation of the all-polymer electrolyte could be a mixture of a gel-like or liquid polymer that transports the ions through a matrix of either a rigid cross-linked polymer host matrix, or a filler host ”matrix”, that ensures the mechanical rigidness of the electrolyte. In search of a suitable filler material that does not significantly reduce the ionic conductivity, a rather recent discovery has been made that by addition of nanoparticulate inert filler material of only a few weight percent, the conductivity of the polymer electrolyte unexpectedly *increases* significantly! The explanation of the mechanism behind this increase in conductivity has been the subject of a considerable amount of scientific effort, since the discovery of the phenomenon, and it is also the subject of part II of this thesis, where we will discuss the phenomenon in more detail.

1.3.3 Aim of this work

The mechanism behind the increase of the conductivity upon addition of nanoparticulate filler material (termed *nanoparticles*) has been investigated for many different combinations of polymers, dissolved salts and filler particles since the first report on the phenomenon [2], and from the observed trends some conclusions were made. The increase in conductivity could for instance be partly attributed to a reduction of the electrolyte crystallinity, a solid state phase that exhibits low ionic conductivity. But even in the fully amorphous polymer electrolytes the phenomenon has been observed and an explanation needs to be sought in the interactions between the polymer, the dissolved ions and the nanoparticle. A typical polymer electrolyte consists of polyethyleneoxide (PEO) and a lithium salt like LiTFSI ($Li^+(CF_3SO_2)_2N^-$) of which the lithium cation Li^+ is the mobile species and the anion is chosen to be a large polarisable molecule so as to avoid ion pairing with the mobile cation. To study the interactions between these electrolyte constituents, we choose a model system that contains these interactions, but simplify it to enable us to complement our measurements with calculations.

In our work on polymer electrolytes in part II we seek to understand the increase in conductivity via the changes in the interactions of the polymer, the cation (being the mobile charge carrier) and the anion on addition of the nanoparticle. The interaction between the polymer and cation can often be described by a coordination number, that counts the number of bonds between the cation and the ether oxygens that are typically in the polymer chain. The maximum coordination number is 6 [16], which means that the bonded interactions between the cation and polymer are local. The aim of this work is thus to probe these local interactions, with and without the nanoparticle and, if possible, to explain the effect of the nanoparticle on the conductivity in terms of these interactions. Since polymer electrolytes are mostly amorphous, direct structure determination by x-ray or neutron diffraction is difficult or impossible. The local average dynamics can however still be measured and this enables us to monitor the local interactions. We choose inelastic and quasi elastic neutron scattering (INS and quasi-elastic neutron scattering (QENS) respectively) as a probe for the dynamics in the polymer electrolyte; an experimental technique that is easily complemented with calculations (both DFT and MD) on the dynamics of the molecular system. The combination of inelastic neutron scattering and DFT calculations will furthermore enable us to find a molecular conformation that corresponds to the observed vibrational dynamics and it will give us an estimate of the sensitivity of the vibrational spectrum to changes in the local molecular conformation.

Although the interest in the ionic conductivity of polymer electrolyte is in the range of ambient temperatures, we cool our samples such that dynamics we are studying are not obscured in our observed spectra by signals due to translational diffusion. Only the local dynamics are studied like vibrations, librations and rotational diffusion, and these will report the changes in the local environment, which in turn will have an impact on the eventual ionic conductivity. The INS and QENS experiments combined with DFT and MD calculations on a model system polymer electrolyte reveals that the nanoparticle softens the local potential energy landscape of the cation and yet leaves the polymer local conformation almost unchanged.

1.3.4 Approach

In amorphous or poorly crystalline materials structure determination by x-ray or neutron diffraction is mostly not possible. But when the molecular dynamics of the individual molecules are studied, it can be shown (as will be done in chapter 4 and chapter 9) that the vibrational normal modes below 1000 cm^{-1} are sensitive to the conformation and environment of the molecule. We make use of this sensitivity by direct comparison of calculated and observed vibrational spectra: the observed spectra are inelastic neutron scattering spectra and the calculations are done on a model system of different conformations. The calculated spectra are obtained as described in section 2.1.1 by conversion of the Hessian matrix of the model system to the normal mode coordinate system of the molecule via the Hellmann-Feyman forces. These forces can be calculated accurately using DFT though the computations are very demanding, so we choose the model system accordingly such that the analysis is feasible by DFT.

Similarly we combine QENS (section 2.2) with molecular dynamics calculation (section 2.3.2) to investigate dynamics on the picosecond time scale. The MD calculations are done using classical mechanics in a force-field description. The force-field parameters are optimized by DFT calculation on the model system obtained from the DFT/INS analysis.

Using the approach of experiments combined with calculations described above, we seek to understand the changes in the interactions between the polymer, cation and anion on a local scale. This local scale is determined by the number of coordinating atoms surrounding the cation (e.g. two PEO chains coordinate each with three of its oxygens to the cation.) To study these local interactions, the polymer PEO is substituted with its oligomer di-glycol-methyl (diglyme) (enabling DFT calculations) that contains 3 ether oxygens and the conformation of the oligomer-cation compound is found using the DFT/INS analysis (chapter 9). The calculated INS spectrum shows a marked sensitivity to the oligomer conformation, and yet the TiO_2 nanoparticle had little influence on the observed INS spectrum above 350 cm^{-1}, from which one can conclude that the oligomer conformation is not significantly altered by the addition of the nanoparticles. These observations are consistent with the QENS experiments on the oligomer, that revealed only a slight dependence of the oligomer dynamics on the addition of nanoparticles. Proceeding with the cation, we determine its dynamics and local conformation with and without the nanoparticle, but to benefit from advantages of the neutron scattering technique we use a deuterated oligomer instead and exchange the lithium cation by a pseudo-alkali ion, ammonium. To make the combined DFT calculations less time consuming, we substitute the anion with iodine. In this manner, the cation dynamics are probed via the incoherent neutron scattering from it hydrogens, as the contribution to the total incoherent cross section from all other atoms is negligible. The observed INS spectra show a considerable shift of the peaks towards lower frequencies, and the trend was reproduced by removing the charge on the model system in the calculations.

Chapter 2

Theory and methods

The approach taken in this thesis as described in chapter 1 is based on several techniques that are outlined in this chapter. For conducting polymers as well as for polymer electrolytes the molecular dynamics are studied at different timescales. In this chapter we divide the dynamics in approximately femtosecond (10^{-15} s) and picosecond (10^{-12} s) events, so that we can apply two distinct theories to describe these dynamics. The former timescale can be conveniently described as harmonic vibrations (section 2.1.1) and the latter by the van Hove time correlation functions (section 2.1.2). The theory of neutron scattering is described in section 2.2 and using different instrumentation, both the picosecond and femtosecond dynamics can be measured. The measured spectra can be compared to calculated spectra that result from molecular modelling, where we make use of harmonic approach for the fs timescale or calculate the time correlations of molecular dynamics simulations (the ps timescale). The method to obtain the fs molecular dynamics from a model system in a parameter-free manner is by *ab initio* calculations of the electronic structure as described in section 2.3.1. These calculations are still too demanding for the current computing facilities, when one wants to use this approach to calculate the ps dynamics of a model system that covers the Q-range of quasi elastic neutron scattering instruments (see chapter 3). The more classical method of force-field molecular dynamics simulation is therefore chosen to describe ps dynamics of our model systems. The force-field itself can be adapted using DFT calculations, as was done for the conducting polymers.

2.1 Dynamics

Two types of molecular dynamics are addressed in this chapter: molecular vibrations, which are periodic by nature and can be modelled from a single molecule and relaxational dynamics, that are typically modelled using a cluster of molecules and which can be either periodic or non-periodic. Different kinds of vibrational spectroscopy are used to probe the former, and the observed spectra can be compared with calculated spectra. In section 2.1.1 the classical approach of calculating these spectra is outlined that assumes the periodic motions of the atoms to be harmonic. This enables a description of the molecule in terms of 'beads and springs' and the molecule is assumed to be completely isolated from its environment §. To address the relaxational dynamics, the same 'beads and springs' description is complemented with intermolecular interactions to simulate the dynamics of a cluster of molecules. The methods of simulation are discussed in section 2.3.2 and the analysis of resulting simulated molecular dynamics is addressed in section 2.1.2.

2.1.1 Molecular vibrations

To calculate the frequencies and intensities of the vibrations of a single molecule, a harmonic interatomic potential is assumed. The model of the molecule consists of beads that are connected with springs and in the harmonic approximation, the spring-force is linearly dependent on the displacement from its equilibrium length. This approximation holds for small atomic displacements. A thorough discussion of methods to calculate molecular vibrations can be found in [17], so only a short summary is given in this section.

The coordinate system of choice to describe the vibrations is aligned with the molecule, such that its origin is on the center of mass of the molecule and all rotations and translations of the molecule are canceled out with respect to this coordinate system. We transform the N Cartesian coordinates to 3N mass-weighted coordinates by multiplying with the square-root of the corresponding mass and naming them sequentially $q_1 \ldots q_N$. The kinetic and potential energy of the whole molecule in that coordinate system then becomes:

$$2T = \sum_{i=1}^{3N} \dot{q}_i^2 \,, \quad 2V = \sum_{i,j=1}^{3N} f_{ij} q_i q_j \tag{2.1}$$

in which the f_{ij}'s are the force constant given by

$$f_{ij} = \left(\frac{\partial^2 V}{\partial q_i \partial q_j} \right)_0 \,, \quad f_{ij} = f_{ji} \tag{2.2}$$

Then Newton equations of motion for the molecule becomes

$$\frac{d}{dt} \frac{\partial T}{\partial \dot{q}_j} + \frac{\partial V}{\partial q_j} = 0 \quad , j = 1, 2, \ldots 3N \tag{2.3}$$

These equations can be solved non-trivially yielding a cosine oscillation of the coordinates: $q_i = A_i cos(\lambda^{1/2} t + \varepsilon)$, where A_i is the amplitude of the oscillation of coordinate q_i, $\lambda^{1/2}$ its frequency and ε its phase. A striking feature of the solutions is that they may be grouped according to their $(\lambda_k, \varepsilon_k)$ pairs. Each of the coordinates q_i in a group k vibrates around its equilibrium with a frequency and phase identical to the other coordinates, but with its particular amplitude A_i. The molecule as a whole thus vibrates with one frequency $\lambda_k^{1/2}$, which is called a normal mode of vibration, and any intra molecular vibration can be expressed in the complete set of $k = 3N - 6$ † normal modes.

---

§ although the intermolecular interactions can also be taken into account within the harmonic approximation

† $k = 3N - 5$ for linear molecules

Since the normal modes are calculated using the potential and kinetic energy of the molecule, it is often more convenient to rewrite the coordinate system into internal coordinates, that are built from the internal conformation of the molecule, consisting of bond lengths, angles between two bonds of one atom, and dihedral angles. Doing so, the kinetic and potential energy terms can be expressed as:

$$2T = \sum_{tt'} \left(G^{-1}\right)_{tt'} \dot{S}_t \dot{S}_{t'} \ , \quad 2V = \sum_{tt'} S_t S_{t'} \ , \quad t, t' = 1, 2, \ldots, 3N-6 \tag{2.4}$$

where S_t are the internal coordinates and $(G^{-1})_{tt'}$ are the coefficients of the inverse of matrix **G** that relates the internal coordinates to the molecular conformation and the atomic masses. Similarly the **F** matrix contains the force constants linking the internal coordinates.

To find the normal modes of vibration and the frequencies the secular equation needs to be solved:

$$\left|\mathbf{F} \ - \mathbf{G}^{-1} \, \lambda\right| = 0 \tag{2.5}$$

yielding the k modes described in internal coordinates and their frequencies λ_k. In the work of this thesis these equations are solved to find the INS spectrum from DFT calculations. The Hessian as extracted from the latter serves as an input the calculate the force constant matrix **F** of the molecule.

2.1.2 Molecular dynamical correlations

In condensed matter the forces on the molecules are not only internal as neighbouring molecules or atoms interact. When we include these interaction (and thus the neighbouring molecules), the molecular dynamics will often contain an anharmonic and non-periodic component, that cannot be analysed in the approach of section 2.1.1. A more general approach introduced by Léon van Hove [18] considers only correlations in space and time of the particles in an animation of the dynamics. To generate such an animation a computer simulation of the dynamics is needed, that includes all inter and intra molecular interactions and in which the kinetic energy of the simulation model is determined by thermodynamics as will be briefly discussed in section 2.3.2. In this section we address the method of analysing the molecular dynamics in such complex systems of molecules that are held by intra molecular forces as described in section 2.1.1 and coupled with Coulomb forces and Van der Waals forces. The molecular dynamics simulation will result in a *trajectory* in time with a particular time step Δt of all the coordinates $\mathbf{r_N}$ of the atoms in the model. The particles for which the correlations are calculated are typically the individual atoms of the molecules and the description of vibrational normal modes in terms of internal coordinates is absent. Similar calculations can be done for the molecules as a whole or fragments of the molecules in the model, which can yield *orientational* correlation functions. For this type of correlation function the deformations of the molecule in the simulation should be small, so that one can assume an average conformation that can be fitted to the (slightly) distorted molecule. The fit is done for all time steps in the trajectory and the orientation of the fitted molecule can then be analysed with correlation functions as described by Van Hove. In addition to the analysis of the vibrational dynamics, harmonic and anharmonic, this approach will therefore also yield the slower dynamics that are concerned with molecular orientation as just discussed and translations and deformations of the molecules in the model. Another benefit of this approach in the work of this thesis is that these correlation functions can be converted into neutron scattering spectra as will be shown in section 2.2.

The general expression of the correlation function, G, in time, t, and space, $\mathbf{r}$, is:

$$G(\mathbf{r},t) = N^{-1}\left\langle \sum_{j,j'=1}^{N} \int d\mathbf{r}' \cdot \delta(\mathbf{r}+\mathbf{R_j}(0)-\mathbf{r}')\delta(\mathbf{r}'-\mathbf{R_{j'}}(t)) \right\rangle , \tag{2.6}$$

where the integers j, j' run over all N particles at the positions $\mathbf{R}$ and $\langle \dots \rangle$ stands for the thermodynamic average. In a simulation of the molecular dynamics as will be discussed in this thesis, we do not model quantum effects and the simulations are run in a thermodynamic equilibrium, so that the average is taken over the ensemble of the simulation and equation (2.6) can be rewritten to:

$$G(\mathbf{r},t) = N^{-1}\left\langle \sum_{j,j'} \delta\left(\mathbf{r}+\mathbf{R_j}(0)-\mathbf{R_{j'}}(t)\right) \right\rangle . \tag{2.7}$$

Both the inter-particle or distinct correlations $j \neq j'$ and the self-correlations (per particle) $j = j'$ are taken into account, that can be written separately: $G = G_d + G_s$, so that correlations due to a periodicity in the model (both dynamic and static) can be excluded from the self-part: the autocorrelation function G_s. This separation is convenient to calculate (from the simulation) the incoherent and coherent contributions to a neutron scattering spectrum as will be discussed in the section below on neutron scattering theory section 2.2, that deals with the neutron scattering function $S(\mathbf{Q},\omega)$ [§]. As a preparation for inclusion of equation (2.7) in $S(\mathbf{Q},\omega)$, the *particle density operator* ρ or $\rho_{\mathbf{Q}}$ is introduced, that can be expressed in real and reciprocal space coordinates:

$$\rho(\mathbf{r},t) = \sum_j \delta\{\mathbf{r}-\mathbf{R_j}(t)\} \,, \tag{2.8}$$

$$\rho_{\mathbf{Q}}(t) = \sum_j e^{-i\mathbf{Q}\,\cdot\,\mathbf{R_j}(t)} \,, \tag{2.9}$$

such that equation (2.7) can be written in the reciprocal coordinates:

$$I(\mathbf{Q},t) = N^{-1}\left\langle \sum_{j,j'} e^{-i\mathbf{Q}\,\cdot\,\mathbf{R_j}(0)}\; e^{i\mathbf{Q}\,\cdot\,\mathbf{R_{j'}}(t)} \right\rangle . \tag{2.10}$$

This is the *intermediate scattering function* $I(\mathbf{Q},t)$ that relates the correlation function $G(\mathbf{r},t)$ to the neutron scattering function $S(\mathbf{Q},w)$.

2.2 Neutron scattering theory

Neutron scattering is a complementary technique to light scattering for many different photon energies, as NMR and infrared up to x-ray photon energies. The fundamental properties of the neutron make it a very suitable probe in condensed matter and solid state research, due to the fortunate combination of its wavelength and energy that both overlap with typical length and time scales of interest to this field of research. Neutrons are generated by releasing them from the nucleus of an atom and need to be retarded from sub-relativistic velocities to roughly 100 m/s to be of use in neutron scattering experiments as described here. The energy E_n of these *thermalized* neutrons is $\sim$ 25meV or less and their wavelength λ is ~ 1 Å or more. These properties can be expressed as:

[§] The vector $\mathbf{Q}$ will be introduced in section 2.2

$$E_n = \frac{|\mathbf{p}|^2}{2m_n}, \qquad \mathbf{p} = \hbar\,\mathbf{k_n}, \qquad |\mathbf{k_n}| = 2\pi/\lambda,$$

where m_n is the neutron mass, $\hbar$ is Diracs constant, $\mathbf{p}$ is the momentum of the neutron and $\mathbf{k_n}$ is the neutron wave vector. Neutrons scatter from the nucleus of an atom and are therefore insensitive to optical selection rules in infrared and Raman spectroscopy where scattering occurs from the electrons. Scattering from the nucleus also simplifies the calculation of scattering intensities in simulated spectra. As chapter 3 will address the experimental basics of neutron scattering, the following short theoretical discussion of neutron scattering will be based on a simplified scattering scheme of a monochromatic incoming neutron flux $\Phi(\mathbf{k_0})$, that impinges on a sample. The scattered neutrons are analysed in energy and scattering angle by a detector as shown in figure 2.1. For a more detailed description of the theory of neutron scattering see e.g. [19].

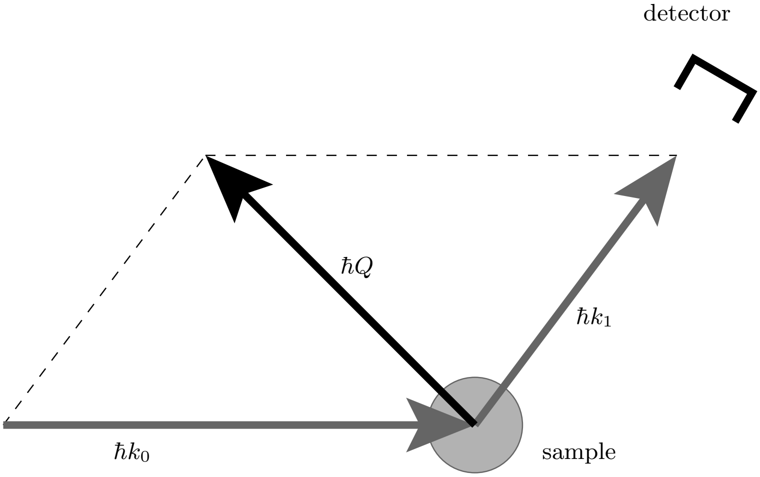

Figure 2.1: The principle of neutron scattering. A monochromatic neutron flux with momentum $\hbar\,\mathbf{k_0}$ impinges on the sample and a fraction of the neutrons scatter, leaving the sample with momentum $\hbar\,\mathbf{k_1}$. Analyzing the energy and angle of scattering of the neutrons is done with a detector as will be described in chapter 3. When these variables are known, the energy transfer E and momentum transfer $\hbar\mathbf{Q}$ can be calculated.

The wavelength of the neutrons is five orders of magnitude greater than the size of a nucleus and the scattering event then will yield a spherical scattered wave. As the sample-detector distance is typically ten orders of magnitude larger than the scale on which the scattering event takes place, the Born approximation can be used, that assumes the scattered neutrons again as plain waves. To compare the neutron scattering experiments with simulations of the sample, we first define the scattering event from the point of view of the sample. The momentum and energy transfer to the sample is given by:

$$\hbar \mathbf{Q} = \hbar \left(\mathbf{k_0} - \mathbf{k_1} \right), \tag{2.11}$$

$$E = \frac{\hbar^2 \left(|\mathbf{k}_0|^2 - |\mathbf{k}_1|^2 \right)}{2m_n}. \tag{2.12}$$

In an experiment the detected neutron intensity I is measured in certain range $d\Omega dE_1$:

$$I = \Phi(\mathbf{k_0}) \cdot \left(\frac{d^2\sigma}{d\Omega dE_1} \right) d\Omega dE_1, \tag{2.13}$$

where σ is the cross-section and $d^2\sigma / d\Omega dE_1$ is the *double differential cross-section*, that depends on the interaction of the neutrons with the sample: the scattering event causes a transition of the system $\{neutron, sample\}$ from its initial state $\{\mathbf{k_0}, \Lambda_0\}$ to its final state $\{\mathbf{k_1}, \Lambda_1\}$, and the transition probability W is expressed by the *Fermi's Golden Rule*[§]:

$$\sum_{\substack{\mathbf{k_1} \\ \text{in } d\Omega}} W_{\mathbf{k_0},\Lambda_0 \to \mathbf{k_1},\Lambda_1} = \frac{2\pi}{\hbar} \rho_{\mathbf{k_1}} \left| \langle \mathbf{k_1} \Lambda_1 \mid V \mid \mathbf{k_0} \Lambda_0 \rangle \right|^2, \tag{2.14}$$

where $\rho_{\mathbf{k_1}}$ is the scattered neutron density of states and V is neutron potential due to scattering centers in the sample. The transition probability as stated here is combined with the *Fermi pseudopotential* to express the neutron-sample interaction per transition in terms of the double differential cross-section:

$$\left(\frac{d^2\sigma}{d\Omega dE_1} \right)_{\Lambda_0 \to \Lambda_1} = \frac{|\mathbf{k_1}|}{|\mathbf{k_0}|} \left(\frac{m}{2\pi\hbar^2} \right)^2 \left| \langle \mathbf{k_1} \Lambda_1 \mid V \mid \mathbf{k_0} \Lambda_0 \rangle \right|^2 \cdot \delta(E_{\Lambda_0} - E_{\lambda_1} + E_0 - E_1) \tag{2.15}$$

$$V(\mathbf{R}) = \frac{2\pi\hbar^2}{m} \, b \, \delta(\mathbf{R}). \tag{2.16}$$

The strength of the pseudopotential $V(\mathbf{R})$ is defined as a 'scattering length' b and is centered on the atom position $\mathbf{R}$. The scattering length is a complex number that depends on the spin state of neutron as well as the spin state(s) of the atom(s) involved and differs per nuclear isotope. In an experiment the observed distinction is not made per transition $\Lambda_0 \to \Lambda_1$ and per scattering length b, but rather as an average over these plus the deviation from the average. The mathematics for the needed conversions is rather involved, so only the result is given here:

$$\left(\frac{d^2\sigma}{d\Omega dE_1} \right) = \frac{|\mathbf{k_1}|}{|\mathbf{k_0}|} \left(\frac{1}{2\pi\hbar} \right) \sum_{jj'} \overline{b_{j'} b_j} \int \left\langle e^{-i\mathbf{Q} \cdot \mathbf{R_{j'}}(0)} \, e^{i\mathbf{Q} \cdot \mathbf{R_j}(t)} \right\rangle e^{-i\omega t} \, dt. \tag{2.17}$$

[§] Fermi's Golden rule treats the neutron-nucleus interaction using perturbation theory and assumes that the neutron de Broglie wavelength is much larger than the interaction range of the nuclear potential for the neutron.

This function contains the intermediate scattering function equation (2.10) that is the pair correlation function in reciprocal space. Recalling that the correlation function $G(\mathbf{r}, t)$ can be separated in a distinct and self part, the double differential cross-section can be separated accordingly:

$$\left(\frac{d^2\sigma}{d\Omega dE_1}\right) = \frac{\sigma_{coh}}{4\pi}\frac{\mathbf{k_1}}{\mathbf{k_0}}\,N\,S_{coh}(\mathbf{Q}, w) \; + \; \frac{\sigma_{inc}}{4\pi}\frac{\mathbf{k_1}}{\mathbf{k_0}}\,N\,S_{inc}(\mathbf{Q}, w). \tag{2.18}$$

$$S_{coh}(\mathbf{Q}, \omega) = \frac{1}{2\pi\hbar}\int_{-\infty}^{+\infty} N^{-1}\left\langle \sum_{j\neq j'} e^{-i\mathbf{Q}\cdot\mathbf{R_{j'}}(0)}\; e^{i\mathbf{Q}\cdot\mathbf{R_{j'}}(t)}\right\rangle e^{-i\omega t}dt, \tag{2.19}$$

$$S_{inc}(\mathbf{Q}, \omega) = \frac{1}{2\pi\hbar}\int_{-\infty}^{+\infty} N^{-1}\left\langle \sum_{j} e^{-i\mathbf{Q}\cdot\mathbf{R_{j}}(0)}\; e^{i\mathbf{Q}\cdot\mathbf{R_{j}}(t)}\right\rangle e^{-i\omega t}dt, \tag{2.20}$$

$$\text{where} \qquad \sigma_{coh} = 4\pi(\overline{b})^2 \qquad \text{and} \qquad \sigma_{inc} = 4\pi\left\{\overline{b^2} - (\overline{b})^2\right\}. \tag{2.21}$$

The total double differential cross-section is a sum of two types of scattering events: the neutron either scatters coherently from a collection of atoms as described by equation (2.19), or incoherently from a single atom, equation (2.20). Equation (2.13) shows how to measure the double differential cross-section, which can also be calculated from molecular dynamics simulations as explained in section 2.1.2 and this section.

2.3 Modelling

To understand more of the observation from the neutron scattering experiments, we combine them with calculations done using different models. The calculations should reproduce the measured results and the models that are selected need to be generically applicable and yet contain a minimum of adjustable parameters. These models can for instance be based on the theory of harmonic vibrations as described in section 2.1.1 for which we would need to know the force constants and the equilibrium bond lengths, bond angles, etc.. In section 2.3.1 a theoretical method called Density Functional Theory is summarized, that can be used to obtain these force constants and equilibrium geometries. This approach has become applicable only recently, as it is computationally a very demanding. Therefore most existing databases of equilibrium geometries and force constants (termed: *force-fields*) are derived from experiments like neutron and x-ray diffraction, thermodynamic measurements and Raman and infra red spectroscopy. We will now focus on the theoretical approach, as it enables us to calculate many more molecular properties besides the force-field parameters as just discussed.

2.3.1 Ab initio

Intra molecular dynamics as discussed in section 2.1.1 idealizes the chemical bonds as springs connecting the nuclei. This model spring is one dimensional and its force is

linear dependent on deviation from its equilibrium length, implying that the chemical bond it describes cannot be broken. According to quantum mechanics the chemical bonds of a molecule exist as a result of a classical Coulomb potential between the nuclei and the electrons, and a non-classical exchange potential. The bond is now visualized as an increase in electron density between the nuclei.
In the beads-and-springs description of an oxygen molecule O_2 in rest, the two oxygen atoms are bonded by a spring that exerts no force. In quantum mechanics the molecule in rest is described by a balance of attractive and repulsive forces. Instead of the three particles in classical approach, we now use all $N_e = 12$ electrons plus two nuclei $N_n = 2$ to describe to molecule and we need to take into account the interactions between all 14 particles. The equilibrium conformation of the molecule is found by minimizing the total energy E of the ensemble of 14 particles with respect to their coordinates. The eigenvalue E of the molecule described by the eigenfunction Φ and the Hamiltonian $\mathcal{H}$ is calculated from the time-independent Schrödinger equation:

$$\mathcal{H}\Phi = E\Phi \tag{2.22}$$

where the Hamiltonian $\mathcal{H}$ is the sum of the kinetic energy operators $\hat{T}$ of all particles and the potential energy terms $\hat{V}$ of the interactions between all particles:

$$\mathcal{H} = \sum^{N_e} \hat{T}_e + \sum^{N_n} \hat{T}_n + \sum_{a=1}^{N_e} \sum_{b>a}^{N_e} \hat{V}_{e-e'} \sum_{c=1}^{N_n} \sum_{a=1}^{N_e} \hat{V}_{e-n} + \sum_{d=1}^{N_n} \sum_{c>d}^{N_n} \hat{V}_{n-n}, \tag{2.23}$$

where the subscripts n, e denote respectively nuclear and electronic contributions or interactions. For the example of the oxygen molecule all interactions between the 14 particles need to be taken into account via the potential V, which means that the Schrödinger equation is coupled via the operator $\hat{V}$ and cannot be solved analytically. Many *ab initio* techniques are developed to give an approximate solution and DFT is a very succesful one. The essential benefit of using *ab initio* methods to describe the molecule and possibly the interactions with its neighbourhood, is that, in principle, it contains no adjustable parameters since it is based on the theory of quantum mechanics and on equation (2.22).

Hartree-Fock theory

As DFT is partially based on the Hartree-Fock method of solving the many electron problem, first a short summary of that approach is given. To solve equation (2.22), several approximation are made, like the Born-Oppenheimer approximation that regards the nuclear and electronic coordinates independent, since the nuclear mass is typically more that 2000 times larger than that of an electron. Therefore we assume the nuclear coordinates fixed and focus only on solving the electronic part of the wavefunction: Ψ. To approximate the many body interactions between the electrons, the force exerted on electron n_i is averaged by calculation of the Coulomb potential caused by the electrons $n_{j \neq i}$ at the position of the electron n_i. Now that the Coulomb potential for electron n_i is determined, the electronic Hamiltonians are decoupled [§] and the wavefunction can be expressed as a product of one-electron wavefunctions

---

[§] assuming that the $n_{j \neq i}$ electrons do not interact

$\chi(\mathbf{x}_i)$ (the *Hartree product*), each dependent *only* on one electronic coordinate $\mathbf{x}_i$. To fulfill the requirement of antisymmetry upon exchange of two arbitrary electron coordinates (the Pauli principle), the Hartree product is written as a Slater determinant. The following equations are expressed in atomic units ($\hbar = m_e = e^2 = 1$), so that the prefactors in the Schrödinger equation can be omitted for clarity. The Hartree-Fock equation for a single electronic wavefunction in atomic units is stated:

$$f(i)\,\chi(\mathbf{x}_i) = \varepsilon_i\,\chi(\mathbf{x}_i), \tag{2.24}$$

where ε_i is the one-electron energy and the *Fock operator* $f(i)$ the corresponding one-electron Hamiltonian:

$$f(i) = -\frac{1}{2}\nabla_i^2 - \sum_{c=1}^{N_n} \frac{Z_A}{|\mathbf{r}|_{iA}} + v^{HF}(i), \tag{2.25}$$

in which the potential energy contributions contains only the nuclear attraction and the averaged electron-electron interaction via the *Hartree-Fock potential* $v^{HF}(i)$ as described above. The total energy of the molecule is the sum over all one-electron energies that are calculated using equation (2.24). Since the interactions between all electrons are included per electron via the averaged potential $v^{HF}(i)$ and via the antisymmetry condition using the Slater determinant, the Hartree-Fock equations are solved in an iterative process, until self consistency is achieved between each wavefunction $\chi(\mathbf{x}_i)$ and each potential $v^{HF}(i)$: The self consistent field (SCF) method. The Pauli principle is fulfilled using a Slater determinant, that contains the one-electron molecular orbitals (in *unrestricted* Hartree-Fock calculations) or two-electron molecular orbitals: the *restricted* Hartree-Fock equations, when each molecular orbital is forced to contain two paired electrons. The molecular orbitals have no general mathematical description and are therefore built from a set of atomic orbitals, that are centered on the nuclei of the molecule: the *basis set.*

To calculate the molecular equilibrium conformation, use is made of the variation theorem, that states that the exact ground state of a molecule is the conformation of the lowest total energy E_0 and that any other conformation will thus result in a total energy $E > E_0$. The best ground state conformation for a given basis set $\{\chi_i\}$ is found by minimizing the total energy to the minimum energy for that basisset: $E_0^{\{\chi_i\}} > E_0$. Besides increasing the basis set size to lower the energy, one can include corrections to the averaged electron-electron correlations by multi-determinant techniques like *configuration interaction* or by applying Möller-Plesset perturbation theory. The major problem for these extensions to the Hartree-Fock theory is that the number of calculations needed to find the minimum energy expands with the number of particles N up to N^7 for some correction approaches. On the other hand, it should be noted that the validity of many computational approaches, like DFT described below, is determined from Hartree-Fock based calculation complemented with these corrections.

Density functional theory

An alternative to calculate the ground state energy of the molecule, that is computationally less demanding, is based on *Density Functional Theory* DFT that states that the electronic ground state energy $E[\rho]$ is uniquely defined by the electron density:

$$\rho(\mathbf{r}) = \sum_{i=1}^{N_e} \left|\chi_i(\mathbf{r})^{KS}\right|^2 . \tag{2.26}$$

The theory DFT is based on the theorem from 1964 by Hohenberg and Kohn [20] , that proves this functional relation between the ground state energy and the electron density, but does not provide the functional, except for a uniform electron gas: a functional that is frequently applied in computational chemistry as the local density approximation (LDA). A year later Kohn and Sham [21] published the Kohn-Sham equations, which are similar to the Hartree-Fock equation (2.24). Within the Born-Oppenheimer they are written as:

$$\left\{ -\frac{1}{2}\nabla^2 - \sum_{c=1}^{N_n} \frac{Z_A}{|\mathbf{r}|_{iA}} + \int \frac{\rho(\mathbf{r}')}{|\mathbf{r}_{e-e'}|}\, d\mathbf{r}' + V_{XC}(\mathbf{r}) \right\} \chi_i(\mathbf{r}) = \varepsilon_i\, \chi_i(\mathbf{r}). \tag{2.27}$$

Now the electron-electron repulsion is calculated from the densities instead of the wavefunctions, as is the potential V_{XC}, that describes the exchange and correlation contributions to the one-electron energy ε_i. In the Hartree-Fock approach the exchange contributions is fully incorportated via the Slater determinant, but the correlation contributions is absent, unless the approach is extended by multi-determinant or perturbation theory calculations. In DFT the exchange-correlation potential is determined by

$$V_{XC} = \frac{\delta E_{XC}[\rho]}{\delta \rho(\mathbf{r})} \tag{2.28}$$

and apart from the electron-electron potential corrections, it also contains the corrections to the kinetic energy due to the neglect of electron correlation.

The major benefit of DFT over the Hartree-Fock method is that the correlation approximation made in Hartree-Fock is incorporated via an expansion in the Slater determinant (scaling as $N!$), which is completely omitted in DFT by use of the potential described in equation (2.28). The calculation of exchange and correlation energies is, however, still based on the local density or (local) density gradient approximations, and as result the exchange energy is underestimated [22].

The choice of molecular electron orbital sets still has to be made: the most common options are atomic orbitals, that are centered on the nuclei, or plane waves used for periodic systems that are completely delocalised. The advantage of using atomic orbitals is that they have a clear physical meaning in the molecule as opposed to plane waves and the number of orbitals used to describe the molecule is significantly less. However, the DFT methods based on plane wave orbitals have evolved to overcome most of its disadvantages compared to the former option. When describing all electrons of a system, the strong fluctuations of the wavefunction in the vicinity of the nucleus can only be taken into account by plane waves if the number of wavefunctions is large. This problem has been circumvented by the introduction of a *pseudo potential* in the core region, that allows the use of nodeless wavefunctions in that region. One can argue that the use of pseudo potentials in DFT introduces a parameterisation in a method that is regarded as *ab initio*. Some resemblance with semi-emipirical method becomes apparent, if not the applicability of the pseudo potentials is kept as generic as possible.

2.3.2 Molecular dynamics

Classical molecular dynamics calculations are based on Newton's equations of motion, where the forces are determined by intra and inter molecular force constants between the atoms of a chosen model system. Kinetic energy is distributed over the atoms according to the Maxwell-Boltzmann statistics and after a certain time interval (typically 1 fs) all coordinates are saved to a trajectory and all forces are recalculated, thereby generating new atomic velocities. The force constants are tabulated in a *force-field* database that contains equilibrium bond-lengths, bond-angles, torsional angles and the corresponding force constants. Non-bonded interactions are included as Lennard-Jones, Buckingham or H-bond potentials. The chosen model contains approximately several hundreds to a thousand atoms, that are placed in periodic boundaries, such that the model size (typically $20-30$ Å) corresponds to the **Q**-range covered by the instruments (see chapter 3).

The combined bonded and non-bonded interactions define the potential energy of the system that is balanced with the kinetic energy using a particular thermostat. In this work we use the NVT canonical ensemble to simulate the dynamics as they occur in our experiments. The resulting trajectory of atomic coordinates is the input for the calculation of the auto-correlation function that is converted to the neutron scattering spectrum. The inherent discrepancy between the calculated and measured neutron scattering spectra are caused by the Born-Opperheimer approximation that is used in the simulation. Even if the force constants would be recalculated during the simulation via *ab initio* methods, this approximation explicitly isolates the molecular dynamics from the quantum mechanical treatment of the electronic subsystem. Ideally, one would include the nuclear motion in the quantum mechanical calculation, but to do so one would need to evaluate the nuclear potential energy surface at every timestep of the simulation.

Chapter 3

Instrumental

Molecular dynamics in this work were measured using neutron scattering. By choosing this technique we are mainly probing the dynamics of the hydrogens in our system, since the incoherent scattering cross section of hydrogen for neutrons is on average more than a factor of 20 times larger compared to other elements in our systems. Substitution of hydrogen by its isotope deuterium leaves the molecule chemically nearly unaltered, yet the incoherent scattering cross section of deuterium is 20 times smaller. The substitution of hydrogen by deuterium is termed 'selective deuteration' and enables us to measure the dynamics of particular parts or molecules of our systems. Since all our systems are soft condensed matter or are in solid state, it must be mentioned though, that dynamics of the hydrogenated or protonated parts are coupled to the dynamics that are 'invisible' to neutrons. Hydrogen will thus report not only the dynamics of the molecule it is part of, but also the changes to the molecular dynamics due to the environment of the molecule.

Since the number of neutrons sources for science is small, so is the number of neutron scattering instruments, and each instrument is uniquely designed to meet certain criteria specific to a field of research. The instruments *can* however be grouped according to the underlying principle of operation. For the spectrometers that are of concern here, two such groups exist: the *direct geometry* setup and the *inverse geometry* setup, both based on the principle of time-of-flight (TOF). The choice between these is mainly dependent on the type of neutron source that the instrument is designed for. At the time of writing this thesis one newly built reactor-type source is in operation, and three spallation-type sources are being built worldwide. The trend for future neutron sources is in favour of the latter, as improvements in brilliance of the spallation-type neutron source seem to be ongoing and the comparable small amount of radioactive waste makes it socially more acceptable. In this chapter the principle of operation of the two types of spectrometers for inelastic neutron scattering is discussed, together with some specification for the instruments on which the experiments were done. Depending on the instrument design the spectrometer can be used to measure the atomic or molecular dynamics in different energy ranges of a spectrum. Figure 3.1 is a descriptive example of an inelastic incoherent neutron scattering spectrum and shows how the different regions of such spectra probe different dynamics. For the purpose of this thesis measurements were done on two QENS

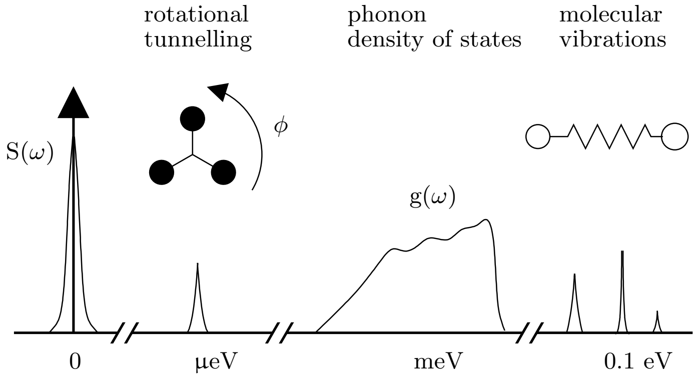

Figure 3.1: An illustrative spectrum showing the different dynamical ranges that are typically covered by inelastic neutron scattering techniques. The x-axis is cut three times for clearness. The intensity in different ranges is not to scale.

spectrometers (one direct, and one inverse geometry) to probe the µeV dynamics as discussed in section 2.1.2, and on one inelastic [§] neutron scattering (INS) spectrometer for the analysis of vibrations as discussed in section 2.1.1. These instruments measure the neutron flux on a set of detectors that surround the sample. The data then need to be converted to $S(Q,\omega)$ and the procedures and software for this conversion are provided by the specific institute. The following two sections will discuss the principle of operation of the instruments.

3.1 Direct geometry

Using neutrons to probe molecular dynamics requires that the energy loss of the neutron in the scattering event is measured, and therefore the energy before and after scattering event must be determined. The incoming neutron beam is chopped in pulses and since neutrons from the source have a velocity of several hundreds m/s, their energy can be measured by the TOF principle. In the setup of the direct geometry only neutrons with a specific energy are selected (using a chopper) to impinge on the sample and the scattered neutrons are labeled according to their time of arrival. As all flight path distances are known, so are the velocities and hence the energies of the scattered neutrons. Besides the energy transfer to or from the neutron, the momentum transfer is of interest. Since the energy and direction of the impinging neutron flux are known, so is k_0 in equation (2.11) and k_1 is determined by the scattering angle and the energy of the scattered neutron as depicted in figure 2.1.

[§] the term *inelastic* scattering is confusingly used to distinguish it from quasi-elastic scattering for which the neutron too scatters inelastic, but with much less energy transfer. In this thesis the same (confusing) convention is used.

3.1.1 IN5

The time-of-flight spectrometer IN5 at the Institute Laue Langevin in Grenoble, France is built on a cold-neutron source and by use of 6 choppers the incoming neutron flux can be selected both in energy and spectral profile. The scattered neutrons are detected using 90 detector groups in an angle range of 15° to 133°. The chopper system was set to yield an energy resolution of 16 μeV (full width at half maximum (FWHM)) and a momentum and energy tranfer range of $0.3 < Q < 1\text{Å}^{-1}$ and $0.17\mu\text{eV} < E < 250\text{meV}$. All measurements were supplemented with a vanadium and empty can measurement for data treatment, background corrections and fitting purposes.

3.2 Inverted geometry instruments

In inverted geometry instruments the TOF principle is used to determine the energy of the neutron similar to section 3.1. The main difference between direct and inverted geometry setups is that in the latter the TOF technique is used to determine the neutron energy *before* scattering. In the inverse geometry scheme no selection is done on the energy of the incoming neutrons and after scattering from the sample, the neutrons are selected by an analyser to allow only neutrons with a particular k_1 to be detected. Again, all neutron flight path distances are known, so that the time

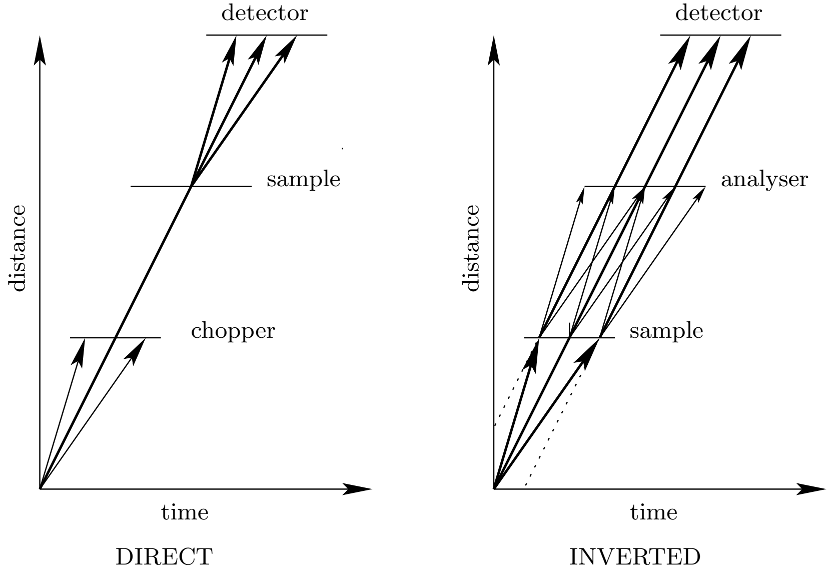

Figure 3.2: One dimensional neutron flight paths to show the principle of operation of the direct and inverse geometry instruments. The time and distances of the neutron flight paths start at the neutron pulse burst and end at the detection of the neutron. In the direct geometry k_0 is defined and k_1 measured by time of flight; in the inverse geometry the situation is reversed (k_0 is measured).

of detection can be converted to obtain the k_0 of the detected neutron. The energy selection of the analyser is realised by Bragg-reflection from a crystal combined with a beryllium filter to remove higher orders.

3.2.1 Tosca

The Tosca spectrometer at the Isis spallation neutron source in Didcot, UK is designed to measure molecular vibrations as described in section 2.1.1. It uses the inverse geometry setup and integrates over the whole incoming neutron momentum range $0.5 < k_0 < 35\text{Å}^{-1}$, thereby yielding high counting rates. The principle of operation is shown in figure 3.3.

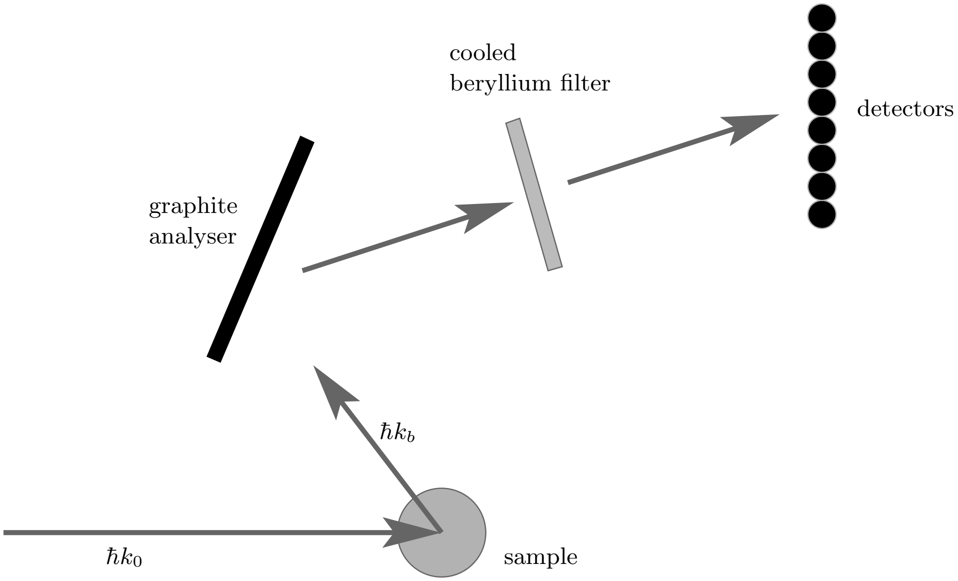

Figure 3.3: Principle of operation of the Tosca spectrometer at Isis. The flight paths of the detected neutrons are set, so that the time of flight determines the kinetic energy of the neutrons, prior to scattering from the sample. The principle here is shown for backscattering ($\hbar\mathbf{k}_b$), but also applies for forward scattering. The analyser defines the energy of the reflected beam and the beryllium filter removes higher order reflections from the analyser crystal.

As the momentum transfer equation (2.11) will be nearly proportional to k_0, the vibrational peaks at higher energies in the observed spectra will contain an increasing amount of phonon wings (see section 2.2). The correction of the observed spectrum for the incoming neutron flux, yields a vibrational density of states, although the distribution of phonon wings is not account for.

3.2.2 Iris

For the picosecond timescale dynamics the Iris QENS spectrometer at Isis is built using a cold-neutron moderator to enable the measurement of energy transfers on a μeV scale. The principle of operation is the same as for Tosca, except for the momentum transfer integration and the scattering angle of the analyser: an array of 51 analysers is set in backscattering geometry around the sample to gain maximum resolution in energy selection and to determine the momentum transfer Q corresponding to energy transfer. The resulting instrumental ranges are $0.3 < Q < 1.8\mathring{A}^{-1}$ and $-0.4 < E < 6.6$meV with an energy resolution of 17 μeV. As with the QENS measurements on the IN5 spectrometer, the measurements are supplemented with an empty can and vanadium measurement for later data correction and data fitting.

Part I

Conducting Polymers

Conducting polymers

The Peierls distortions in quasi-1D systems like polymer chains induces a single-double bond sequence in the chain, which in turn causes a bandgap near the electronic Fermi level. The effect of the Peierls distortion is quite significant since the inter-atomic bonding is quasi-1D (cf. 3D in solid state crystals) and for the same reason a charge on the chain will also induce a significant geometric relaxation of its molecular surrounding. When a photogenerated exciton thus dissociates, the transport of both charges will be hindered, as the conformational relaxation generates a local potential energy minimum [§] unless the residence time of the charge on a particular site is much less than the time needed to generate nuclear relaxation. The conformational relaxation localises the charge and it returns the band-like description of the electronic energy levels to a local orbital description. The transport of the charge cannot be described as a coherent process then, but as a charge hopping from site to site, given to a good approximation by the Marcus equation

$$k_{ET} = \frac{4\pi^2}{h}\frac{1}{\sqrt{4\pi k_B T}}J^2\left(-\frac{\lambda}{4k_B T}\right) \tag{3.1}$$

where h and k_B are the Planck and Boltzmann constants, T is the temperature, λ the reorganisation energy and J the charge transfer intergral (CTI). The CTI goes over into a continuous band when an infinite chain of particles is taken, and the bandwidth can be estimated from the splitting of levels using a dimer. As mentioned by Brédas et al. [23] the residence time of the charge is then inversely proportional to the bandwidth W:

$$\tau \approx \frac{h}{W} \approx \frac{2}{3}\frac{10^{-15}}{W} \tag{3.2}$$

where W is given in eV.

The bandwidth W is a measure of the electronic coupling between two units, and as such a measure of the tunneling probability. In our work in this part of the thesis we have estimated the bandwidth W from the splitting of the highest occupied molecular orbital (HOMO) of two dimers, when they are brought into proximity.

As shown in figure 3.4 the wavefunctions corresponding to the HOMO levels of the two dimers can interfere constructively or destructively and this interference results in new orbital levels that are non-degenerate.

[§] the transport of a charge resembles a train that deforms the track it is on by its weight, and therefore will continuously ride 'uphill'

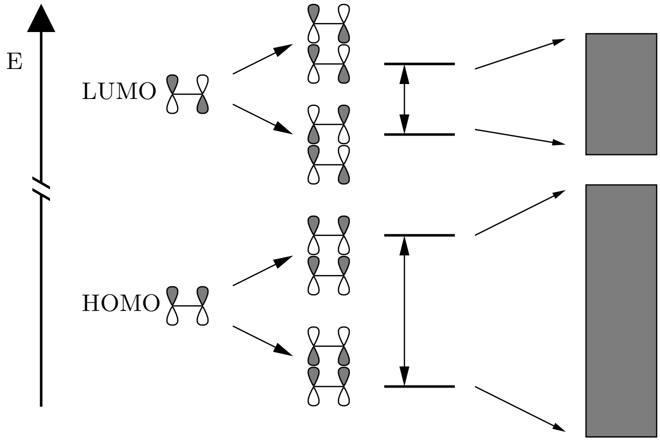

Figure 3.4: The combination of molecular π orbitals into a dimer generates new orbital levels that are non-degenerate, because different combinations are possible. With an increasing number of participating molecules, these discrete levels turn into continuous band. The degeneracy can be understood considering the wavefunction symmetry of π orbitals: combining wavefunctions by constructive overlap yields the lower energy level of two possibilities.

The band model description of conducting polymers is based on a perfect infinite crystal, which in practice is disturbed by static and dynamic disorder. Several approaches are possible to probe the effect of disorder on the CTI, such as the assumption that the delocalisation of the polaron is defined by the defect-defect distance on a chain. This approach has been taken by Grozema et al. [14] who determined the polaron mobility taking dynamic disorder into account of intermonomer dihedral of an isolated finite chain. More recently, Meisel et al. [12] have determined the self-trapping energy of a polaron on an infinite isolated chain, and determined from DFT the conjugation length. The self-trapping energy is much lower than $k_B T$, and plays no role in practice. The effect of neighbouring polymer chains in a perfect infinite crystal is investigated by Ferretti et al. [13] and Puschnig et al. [24], both suggesting that the inter-chain coupling is largest in a herringbone type crystal of the same symmetry of HT-quaterthiophene [25].

We address the effect of disorder, by calculating the change in the intra-chain CTI in dynamically disordered conformations. As a first attempt, the deformations of an isolation molecule are used as in an input, that are derived from DFT vibrational calculations (chapter 7). We then proceed to a more realistic model of the dynamics by creating a crystal supercell and determining the dynamics at finite temperature, whereby we include the anharmonic effects due to neighbouring molecules in the crystal (chapter 8). From these dynamics the time dependence of the CTI is calculated for intramolecular transfer and the Fourier transform is compared with the vibrational spectrum of the calculated and observed dynamics. Only certain vibrational normal modes have a distinct effect on the CTI and we compare our findings with polaron binding energies reported in literature.

Chapter 4

INS as a probe of inter-monomer angles in polymers

published in: *Appl. Phys. A 75, S496 (2002),*
L. van Eijck, L. D. A. Siebbeles, F. C. Grozema,
I. M. de Schepper and G. J. Kearley

Abstract

The angle between monomers in conjugated polymers plays an important role in their conductivity. The vibrational spectrum is sensitive to this angle and can be used to probe the distribution of angles in poorly crystalline systems. We show that the INS spectrum is correctly calculated for bithiophene and shows the molecule to be planar in the solid – in agreement with crystallographic measurements. Poor agreement between observed and calculated spectra in the 700 cm^{-1} region may be due to dynamic coupling, but this does not detract from the angle-sensitivity of the spectra.

4.1 Introduction

It is well known that the conduction of electrons or holes along conjugated polymers is via the overlap of π systems along the chain, and that this overlap is sensitive to the angles, ϕ , between conjugated rings containing the systems. The rotational potentials V(ϕ) for isolated chains, or oligomers, are easily obtained from first-principles calculations, and can be used to obtain a thermal distribution of ϕs which provide insight into the conductivity of isolated molecules [26, 27]. However, this type of calculation makes assumptions about the spatial distribution of angles, and ignores solid-state effects. It is difficult to obtain these angles, ϕ, because in general these systems are poorly crystalline, but in the present study we show that vibrational spectroscopy with INS can give useful structural information. The basic idea is to use solid oligomers in which the angle is known, and then to compare the observed INS spectrum with that calculated from first principles for a variety of inter-ring angles. Because both the spectral intensity and the vibrational frequency can be calculated rather easily for INS (see [28] and references therein) this method is better suited to this type of study than the corresponding optical spectroscopies. Further, there is the possibility in future studies to eliminate the spectral contribution of certain segments by selective deuteration, which considerably enhances the power of this technique. We examine the INS spectrum of 2,2-bithiophene which was reported by [29]. These authors performed ab-initio calculations for three oligomers of thiophene in the gas-phase, but in the present work we examine the solid by using periodic density functional theory. The rotational potential, V(ϕ) of the gas-phase molecule has two equal minima at 153° and 207° and two equal sub-minima at 27° and 333° (throughout this article we refer to $\phi = 0°$ as the planar configuration with the S-atom cis to each other). In the solid state $\phi = 180°$, and clearly, although the solid-state effects are rather weak, they are enough to condense the pairs of minima into a single minimum (180°) and a sub-minimum (0°). This has measurable spectral consequences. Using a periodic model for the rotational potential, we find that the potential form is approximately parabolic at small displacements. In fact, the solid-state effects for this compound have rather little effect on the molecular vibrations which can be seen by comparing the calculated INS spectrum for both the gas-phase and periodic systems. Similarly, any anharmonicity of rotational potential seems to have rather little effect on the spectrum of the solid, the relevant modes calculated under the harmonic approximation give fair agreement with experiment.

4.2 Computational

All energy calculations were carried out using the DFT package DMOL^3 [30] on either a periodic model from the measured crystal structure [31], or a single "isolated" molecule. Localised basis sets were used, represented as a numerical tabulation: a DND double numerical basis set with polarisation functions for carbon was used. The radial extent of the integration mesh was 10 au and the angular grid was adjusted to give numerical precision of 0.0001. Due to the use of rather intensive periodic calculations we restricted ourselves to the Local Density Approximation LDA (Perdew-Wang). The vibrational spectra were calculated in the harmonic approximation using the finite displacement technique to obtain the dynamical matrix. Starting from given geometries each of the atoms in the unit cell was displaced by 0.1 Å in turn along the three Cartesian directions, a single point calculation gives the Hellmann-Feynman forces on all the atoms from which the force constants are obtained by dividing by the displacement. Positive and negative displacements were used in order to obtain more accurate central finite differences. The force constant matrix **F** was transformed to mass-dependent coordinates by the inverse kinetic-energy matrix, **G**, giving the dynamical matrix. Diagonalisation of the dynamical matrix gives the vibrational eigenvalues and eigenvectors. The program CLIMAX [32] was used to calculate the neutron spectral profile corresponding to the measured spectrum, from the normal modes. The normal vibrational coordinates are mass-weighted, the scattering cross-sections of the different atoms are taken into account, overtone and combination frequencies are included, and the recoil of molecules is incorporated by convoluting the calculated peaks with the measured phonon spectrum.

4.3 Results and discussion

The variation of the INS spectrum calculated for an isolated bithiophene molecule as a function of the angle, ϕ, between the two rings is illustrated in figure 4.1. It can be seen that the spectral profile changes smoothly as a function of ϕ in the 200 to 550 cm^{-1} spectral region.

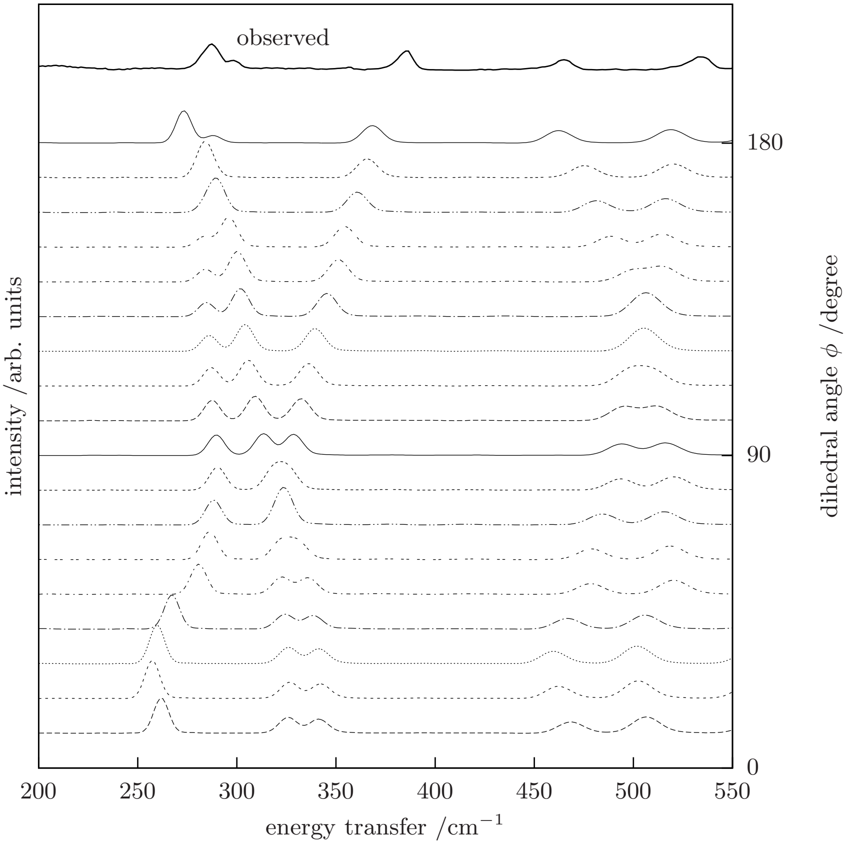

Figure 4.1: Variation of INS spectrum as a function of the inter-ring angle ϕ, as calculated from first principles. The measured INS spectrum is illustrated at the top.

There are 5 main diagnostic peaks in this region, and the modes giving rise to these are shown schematically in figure 4.2 for the minimum-energy configuration of the isolated molecule.

These modes are best described as out-of-plane ring modes and in-plane twists of the rings with respect to each other. It is easy to understand why these modes should be sensitive to the inter-ring angle ϕ. The observed INS spectrum is also shown at

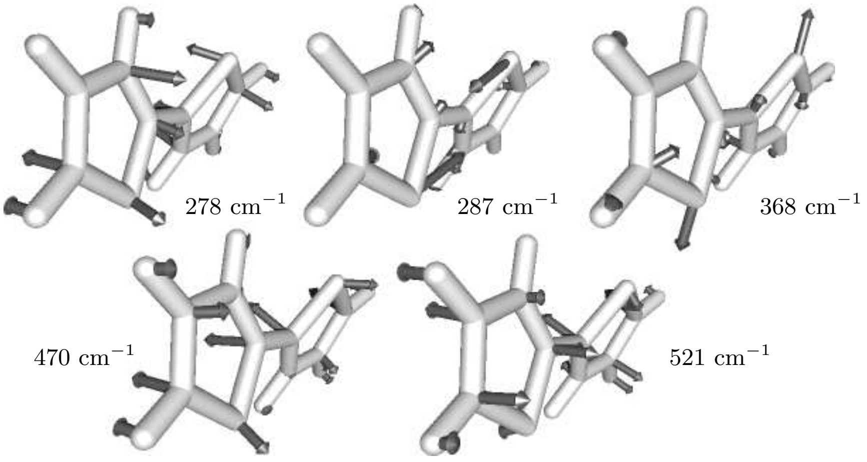

Figure 4.2: Atomic displacements (amplified for clarity) for those modes which are sensitive to the inter-ring angle ϕ and for which there is good agreement between observed and calculated spectra. For simplicity the isolated molecule modes are shown with $\phi = 27°$.

the top of figure 4.1 and it is immediately clear that the value of ϕ in the solidstate is much closer to 180° than it is to the 153° calculated for the gas-phase molecule. Basically, even using an isolated molecule approximation we can estimate ϕ to within about 10° from the INS spectrum. Although calculations for the INS spectrum in the ϕ-sensitive region below about 600 cm^{-1} agree well with the observed spectrum, much of the spectrum above this region, and particularly around cm^{-1} show poor agreement. This can also be seen in the earlier work of [29]. It is interesting to ask if this disagreement arises from intermolecular interactions, although we might expect this to be most serious for modes containing a contribution from the inter-ring torsion, which are actually calculated correctly. We have investigated this possibility by calculating the INS spectrum from the measured crystal structure using periodic DFT. The resulting calculated spectrum is compared with the observed spectrum in figure 4.3. The agreement in the 200 to 550 cm^{-1} region is slightly better than for the isolated molecule, but the agreement for modes in the 700 cm^{-1} region remains poor. We conclude that this disagreement is not due to solid state effects, and further, is unlikely to arise from anharmonicity given modes containing the torsional coordinate, which is most likely to be anharmonic, are calculated correctly.

The observed and calculated spectra of thiophene are also illustrated in figure 4.3 and again it can be seen that there is particularly poor agreement in the 700 cm^{-1} region. For both thiophene and bithiophene these modes involve large out-of-plane displacements of the H-atoms which in turn gives them high intensity in the INS spectrum. These modes are shown schematically in figure 4.4 for bithiophene. The remaining possibility for this disagreement is that there is dynamic coupling of these modes which is not present in the model. For example, long-range interactions are taken into account by the periodic DFT calculations, but limiting the periodic model to a single unit cell excludes excitations with wavelengths longer than the unit cell

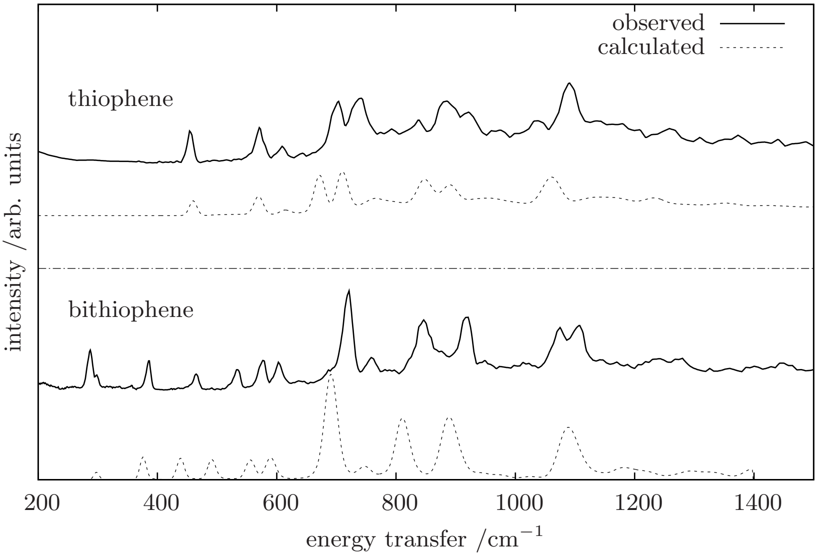

Figure 4.3: Lower spectra compare observed INS (solid line) with spectrum calculated from periodic DFT (dot-dash line) for bithiophene. Upper spectra are observed (solid line) and calculated using DFT for isolated molecule of thiophene.

dimension. Such a model would not reveal any cooperative effects. The crystal structure of bithiophene is composed of chains of molecules in which the closest approach is 2.8 Å this being via the hydrogen atoms (see figure 4.5). It is conceivable that the out-of-plane motions of these hydrogen atoms are coupled beyond the simple in-phase and out-of-phase components of the unit-cell group.

4.4 Conclusions

The spectral region below about 600 cm^{-1} is sensitive to the angle between the two thiophene rings, and the INS spectrum in this region is reproduced by a first principles calculation with no adjustable parameters. Intermolecular interactions have little effect on this region and the isolated-molecule approximation works well. It would be interesting to attempt the same analysis of other conjugated oligomers and eventually larger polymeric systems. The poor agreement between observed and calculated spectra in the 700 cm^{-1} region may arise from dynamic coupling which is not treated correctly either in the isolated molecule, or the periodic, calculation. Since this discrepancy is also present in thiophene, an experiment using isotopically dilute C_4SH_4 in C_4SD_4 could be used to further investigate these dynamics.

Acknowledgements

We are grateful to Profs. Esposti and Zerbetto for the use of the INS spectra presented in this work.

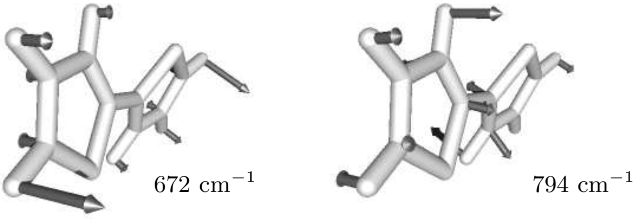

Figure 4.4: Out-of-plane modes for which there is poor agreement between observed and calculated spectra.

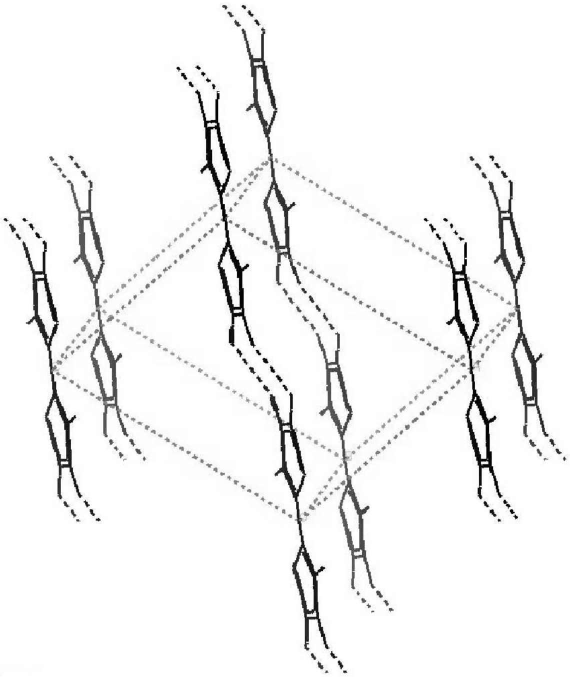

Figure 4.5: Crystal structure of bithiophene showing the closest distances between molecules in a chain (2.8 Å) as broken lines.

Chapter 5

Intermolecular Interactions in Bithiophene

published in: *J. Phys. Chem. A 107, 8980 (2003),*
L. van Eijck, M. R. Johnson and G. J. Kearley

Abstract

Intra- and intermolecular interactions in bithiophene are investigated via the measured and calculated vibrational density of states for the polycrystalline material. There is strong intermolecular interaction that hardens vibrational coordinates with respect to the isolated molecule, especially the inter-ring torsion. The torsional barrier of the isolated molecule is understood in terms of delocalization energy, nonbonded intramolecular interaction, but in the solid the barrier is dominated by intermolecular interaction. A topological analysis of the calculated electron density provides a local interpretation of intermolecular bonds that give rise to the intermolecular interactions. The results for this simple conjugated system are important for the extension to polythiophene and other conducting polymers.

5.1 Introduction

Bithiophene is of interest as a model system for conjugated polymers, in particular polythiophene [26]. The interest here arises from the long-range delocalization of the π-systems on neighboring rings that gives rise to a small HOMO/LUMO gap that can be tuned for conducting/semiconducting purposes. To understand these properties in practical systems, we need to investigate how the dynamics of a model system affect the instantaneous electronic structure of the conjugated systems. It is convenient to begin with a vibrational analysis of crystalline bithiophene, this being a comparatively well-defined system. Further, it is small enough to allow calculation of both inter- and intramolecular interactions from first principles and we can then compare the predictions with existing experimental data for structure and dynamics. First-principles calculations frequently use the isolated molecule approximation, and this can have serious consequences when the predictions are compared with experimental data for dynamics in the solid state. In vibrational analyses these discrepancies are often scaled out, but then it is impossible to assess the quality of the quantum-chemistry calculation for intermolecular interactions. In the present work we use the available INS spectra [29] as our experimental data. In this spectroscopy we are able to compare observed and calculated spectra directly because the intensities are simply related to atomic displacements and peak shapes can also be calculated. Further, INS measures the vibrational density of states, not simply the $k = 0$ (or Γ-point) spectrum, so that we are sensitive to the effects of dispersion via peak shape and spectral profile. Both local solid-state effects and dispersion reflect the intermolecular interactions and it is useful to see how well quantum-chemistry calculations are able to reproduce these. Assuming this to be adequate, the same methods (or parameters derived from these) can be used for larger polymeric systems.

5.2 Density Functional Theory Vibrational Calculations

A number of codes are now available for performing periodic DFT calculations, and these were recently assessed in the calculation of INS spectra of durene [33]. In the present work we have used VASP [34] and DMOL^3 [35], the former using plane-wave basis functions to develop the electron density, whereas the latter uses localized, numerical atomic orbitals. For both codes, more or less standard settings, with only a few modifications, were used. For most of the DMOL^3 calculations, a DND double numerical basis set with polarization functions for carbon was used. The radial extent of the integration mesh was 10 au and the angular grid was adjusted to give a numerical precision of 0.0001. All calculations with VASP were performed using the generalized gradient approximation of Perdew and Wang (PW91) for the exchangecorrelation energy and Vanderbilt-type ultrasoft pseudopotentials. The recommended energy cutoff (396 eV) for the plane wave basis set and a k-point spacing of 0.1 Å^{-1} were used. The vibrational spectra were calculated in the harmonic approximation using the direct method to obtain the forces. Starting from the equilibrium geometry, atoms in the asymmetric unit are displaced along the three Cartesian directions. For each perturbed structure, an energy calculation gives the Hellmann-Feynman forces on all the atoms from which the force constants are obtained by dividing by the displacement. The force-constant matrix $\mathbf{F}$ is then transformed to mass-dependent coordinates by the $\mathbf{G}$ matrix giving the dynamical matrix. Diagonalization of the dynamical matrix gives the vibrational eigenvalues and eigenvectors. The program CLIMAX [32] was used to calculate the neutron spectral profile, corresponding to the measured spectrum, from the Γ-point, normal modes. The normal vibrational coordinates are mass-weighted, the scattering cross-sections of the different atoms are taken into account, overtone and combination frequencies are included, and the recoil of molecules is incorporated by convoluting the calculated peaks with the low-energy phonon spectrum (either measured or calculated).

The full phonon spectrum was calculated using the program PHONON [36]. Whereas a Γ-point-only calculation is exact for a single unit cell, accurate dispersion relations require a supercell to be used that spans the range of typical interactions. When an atom at the center of the supercell is displaced, the forces on the atoms at the

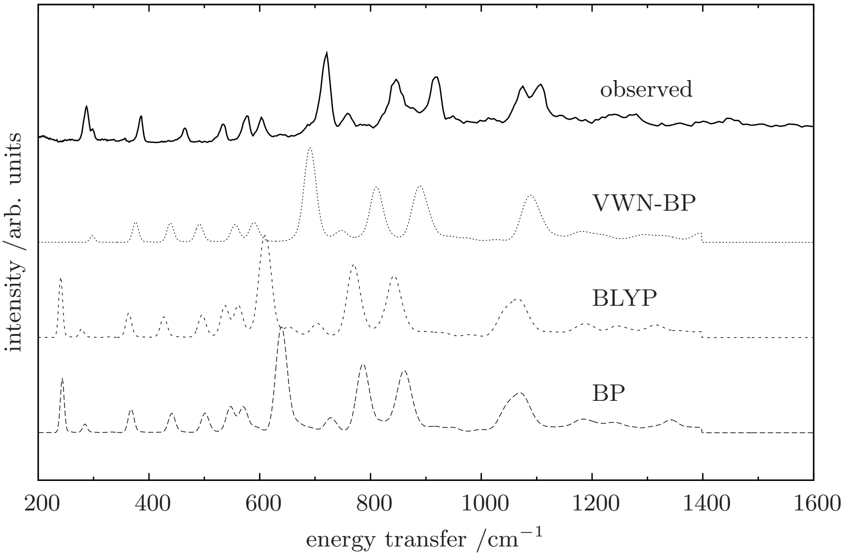

Figure 5.1: Comparison of observed INS spectrum of solid bithiophene at 20 K with calculated spectra using different functionals (DMOL^3). No scaling has been applied.

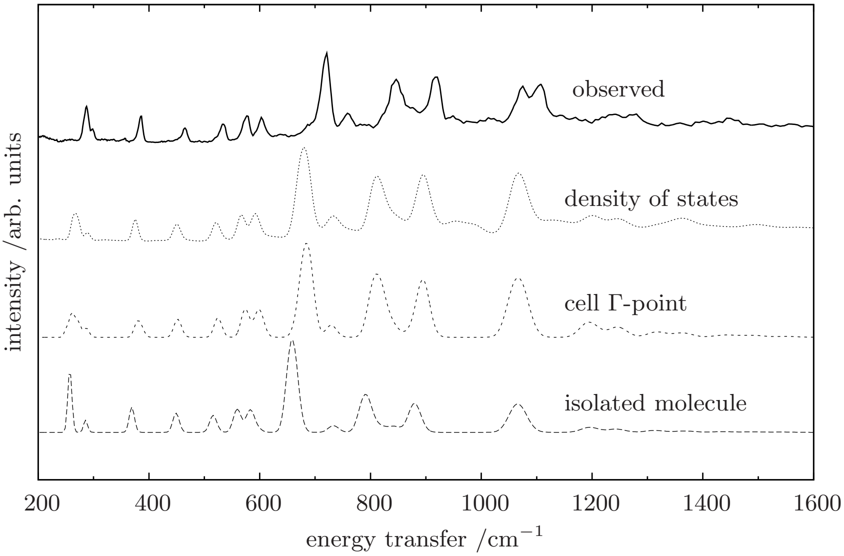

Figure 5.2: Comparison of experimental INS spectrum of solid bithiophene (20 K) with spectra calculated using DFT (VASP) with different treatment of solid-state effects.

cell boundary should be zero. For bithiophene, a $(1, 1, 2)$ supercell of dimensions $a = 8.93\text{Å}$, $b = 7.73\text{Å}$, $c = 11.46\text{Å}$, $\gamma = 73.8°$ (Kovalev setting) was used, with a factor of 1000 between the strongest and weakest force constants. The dynamical matrix is constructed for the supercell from a series of single point energy calculations on perturbed structures, as described above. To generate the density of states, the generalized dynamical matrix is diagonalized at a large number (1000) of randomly chosen points in reciprocal space. The INS spectrum is calculated as above, with up to 5 multiple phonon contributions of all inter- and intramolecular modes, included to account for overtones, combinations and molecule recoil, for the particular Q-trajectory of the instrument and convoluting with the instrument resolution function.

5.3 Results and Discussion

5.3.1 Isolated Molecule Vibrations

INS spectra of bithiophene are illustrated in figure 5.1 along with calculated INS spectra from various DFT options using an isolated molecule model. Agreement between observed and calculated data in the 250−650 cm^{-1} region is quite good, and in a previous paper [37] we showed that this spectral region is sensitive to the orientation angle between the thiophene rings. However, above 650 cm^{-1} the agreement between observed and calculated INS spectra is less satisfactory, and below 250 cm^{-1} there is little agreement. In this low-frequency region intermolecular interactions are expected to play an important role, and it is thus not surprising that agreement is poor. Nevertheless, it is surprising that the agreement in the 250−650 cm^{-1} region is better than in the region above 650 cm^{-1}, because here the vibrations are quite "hard". In the absence of strong hydrogen bonds we do not anticipate much effect from intermolecular interactions in this region. Previous authors [29] have overcome these discrepancies by using different scale factors in different spectral regions when an isolated molecule approximation is used. However, this approach effectively throws the intermolecular information away. Unfortunately, error-cancellation in DFT methods is still somewhat unpredictable, particularly for weaker long-range interactions, and it is important to test the calculations against experimental data. It is widely believed that deviations from coplanarity between the π-systems of conjugated polymers are an important factor in the conductivity of the polymer chains [14].

We will show the rotational potential of the intermonomer angle is dramatically increased in the solid state.

5.3.2 Periodic Model Vibrations

There are now a number of standard quantum-chemistry packages that allow DFT methods to be applied to periodic systems. We found that VASP and DMOL^3 gave very similar results, so in the vibrational part of this work we will refer only to results from VASP. Energy minimization of the published crystal structure [31] resulted in only small atomic displacements, the unit-cell parameters being constrained to the experimental values. This result is encouraging because it shows that the calculated potential-energy minima for the atoms correspond well with the experimental atomic positions. The experimental INS spectrum is compared with the calculated spectra

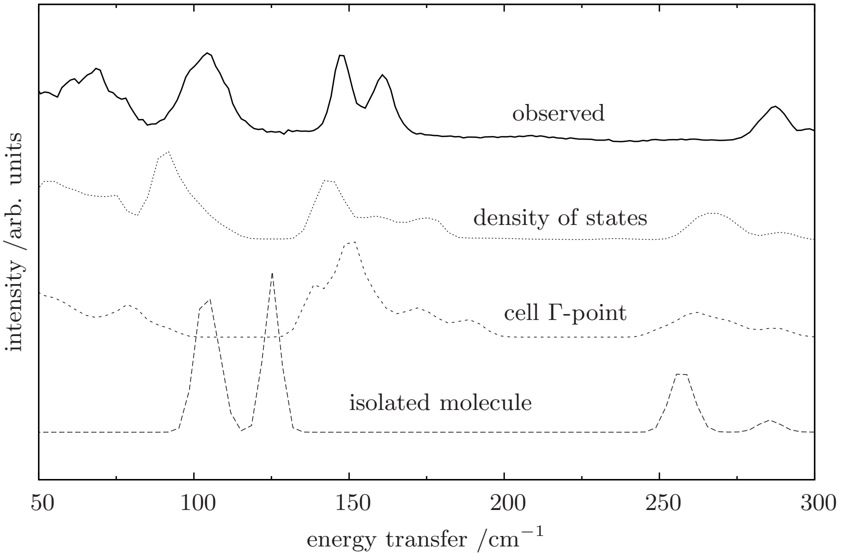

Figure 5.3: Low-energy region of the INS spectrum of solid bithiophene (20 K) compared with spectra from DFT calculations (Vasp) with different treatment for solid-state effects.

for an isolated molecule and the energyminimized periodic model in figure 5.2. It is clear from the figure that the periodic model gives a marked improvement in the agreement in the 50−250 cm^{-1} region, an expansion of this region being illustrated in figure 5.3. We conclude that the calculation seems to take reasonable account of the intermolecular interactions. Perhaps surprisingly, the periodic model also does better in the higher frequency region above 650 cm^{-1}, there being a significant upward shift of most bands toward the experimental features, and the overall agreement of intensities is also improved. Clearly, there are solid-state effects in this spectral region and we will look into these later in the paper.

5.3.3 Dispersion of Vibrations

Intermolecular interactions over longer ranges lead to dispersion, which because of the incoherent neutron scattering process leads to the measurement of a density of states in the experimental INS spectrum.

Because there is still some residual disagreement between the experimental INS spectrum and that calculated from the periodic model, it is interesting to inquire whether taking account of dispersion can reduce this disagreement. The spectrum was collected using the TFXA instrument at the ISIS facility in the U.K., which works in a so-called "inverted geometry" or fixed final-energy mode. Because the final neutron-

---

[§] These wavenumbers correspond to maxima in the density of states and are not directly comparable with the long-wavelength limit values measured by IR and Raman spectroscopies. For simplicity, however, the symmetry species are for the point group.

Table 5.1: Observed and calculated frequencies for the full solid-state calculations.

approximate assignment	obs $/\mathrm{cm}^{-1}$	calc $^{\S}/\mathrm{cm}^{-1}$
Ag ring deformation	287	269
Ag ring deformation	385	376
Ag ring deformation	758	733
Ag ring deformation	919	900
Ag CH bend	1075	1071
Ag CH bend	1075	1071
Bg ring puckering	534	523
Bg ring puckering	602	593
Bg outer CH bend	721	680
Bg CH bend	847	813
Bg CH bend	919	897
Au ring puckering	465	453
Au ring puckering	577	566
Au outer CH bend	721	680
Au CH bend	847	813
Au CH bend	919	897
Bu ring deformation	758	733
Bu ring deformation	919	897
Bu outer CH bend	1075	1071
Bu CH bend	1107	1071

energy is small compared with the energy transfer, the momentum transfer, Q, is approximately proportional to square root of the energy transfer, E, with a proportionality constant of 0.2438 for Q in $\mathring{A}^{-1}$ and E in cm^{-1}. Each spectral point is then proportional to the density of states up to the corresponding value of Q, and if the dispersion is calculated, it is straightforward to produce the predicted TFXA spectrum. The results of the "full-phonon" calculation are also shown in figure 5.2 and figure 5.3 where they are compared with both the experimental INS spectrum and the calculated Γ-point ($k = 0$) calculation. Wavenumber data are collected in table 5.1. Above 250 cm^{-1} the improvement is very slight, the modes being almost undispersed. The region below 250 cm^{-1} is shown on an expanded scale in figure 5.3. Though an improvement in this region is achieved by using a periodic model rather than an isolated molecule, there is further improvement when dispersion is also included. This is a further indication that the DFT method used in this work reproduces the vibrational effects of intermolecular interactions on those modes that are highly populated at around room temperature, and which are particularly relevant to conducting polymers.

5.3.4 Rotational Potentials

Having established that DFT at this level provides reasonable intermolecular interactions, we can now investigate the role of these interactions in more detail. The difference between the measured and calculated conductivities of isolated polythiophene chains is thought to be due to dynamic disorder and local chain defects. It seems reasonable to expect that increasing disorder of the rotational angle between monomers will play an important role in reducing the conductivity, and in real solid-state systems intermolecular interactions may make an important contribution to local rotational barriers.

Our calculation of the rotational potential using DMOL^3 for an isolated molecule agrees with that previously published [14] and has the form illustrated in figure 5.4. Although the molecule adopts a flat orientation in the crystal, in the isolated molecule the monomers are twisted by 27° with respect to each other in the minimum-energy conformation. This is a result of weak interaction of the hydrogen atoms nearest to the inter-ring bond, as is confirmed by the reduction in the inter-monomer dihedral angle when the C−C−H angles are constrained to reduce the interaction of these hydrogen atoms. In figure 5.4 we also include the rotational potential of bithiophene using only the "nonbonded" terms of an ab initio based force-field (COMPASS [38]). Here it is clear that the delocalization energy has a minimum at 0° whereas the "nonbonded" energy has a minimum at 80°, the sum of the two functions having a minimum at 27°. We have also calculated the rotational potentials of ter-, quater- and sexithiophene, and these are illustrated in figure 5.5. As the conjugated system becomes longer, the delocalization energy increases, whereas the "nonbonded" interactions are unchanged. This results in an increase of the rotational barrier with the minima shifting more toward 0° and 180° (subminimum for *cis* configuration). For crystalline bithiophene we have used a cluster model of 7 molecules to estimate the intermonomer rotational potential in the solid state. This calculation could also have been made for a periodic model using a considerably larger cell, but this would be unnecessarily time-consuming, particularly considering that nearest-neighbour inter-

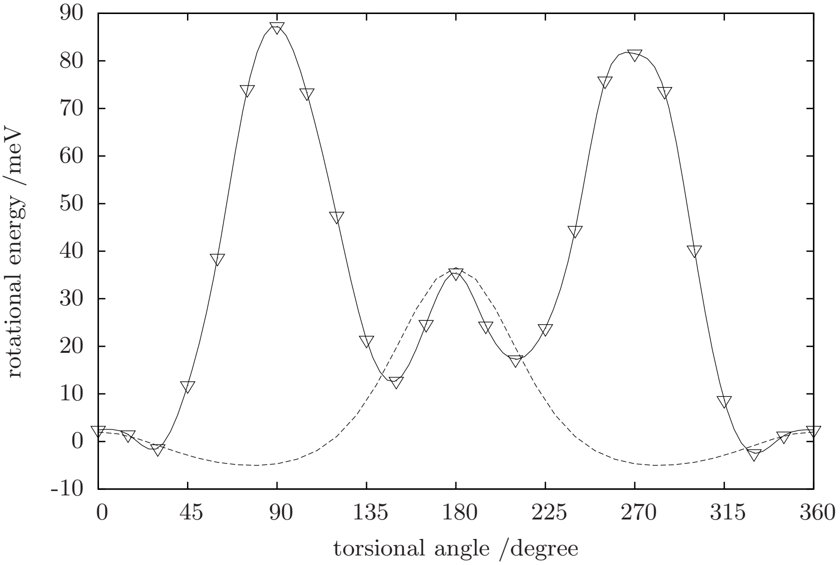

Figure 5.4: Comparison of the total rotational potential for an isolated bithiophene molecule calculated by DFT (DMol^3) (solid line), with the van der Waals contribution to this potential calculated with a force-field method (Compass) (dashed line). The DFT total potential has been shifted to the y-axis range of the Van der Waals contribution and the magnitude of the van der Waals contribution has been rescaled to the submaximum of the total potential. The lines through the calculated data points are merely a guide to the eye.

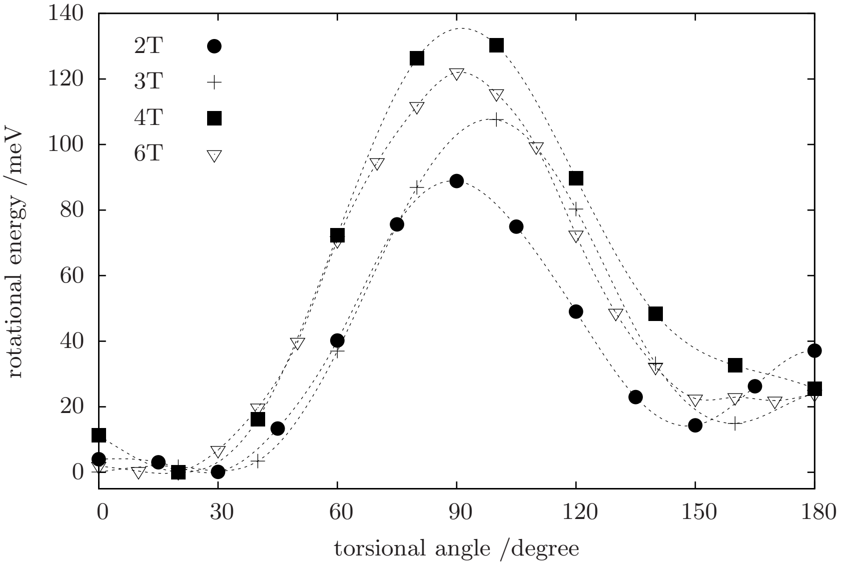

Figure 5.5: Barrier to rotation of terminal thiophene units in: bithiophene , terthiophene, quaterthiophene, and sexithiophene. These calculations were made using DFT (DMol^3) for the isolated molecules. The lines through the calculated data points are merely a guide to the eye.

actions are the most important. In this case we did not allow the structure of the cluster to relax during the rotation, which clearly leads to a falsely high total barrier. Nevertheless, the torsional force-constant taken from the curvature of the potential close to the minimum is fairly insensitive to this approximation and we find that the torsional force constant is 5 times greater in the solid state than for the isolated molecule. Even in a poorly crystalline polymer the intermolecular interactions are similar and would lead to a considerable stiffening of the rotational freedom of the chain.

5.3.5 Directional Interactions in the Solid State

The intermolecular interactions are manifest in the shifts of the vibrational frequencies in going from the isolated molecule to the periodic system. Because there are significant shifts even for modes at almost 1000 cm^{-1}, these interactions are quite strong, although they do not lead to dispersion in this spectral region. Rather than mapping out pair potentials to determine where these stronger interactions lie, we use a topological analysis of the calculated total electron density (ρ) map to determine bond paths within the formalism proposed by Bader [15]. We start by locating the critical points in the electron density, that is, where the gradient of the electron density $\nabla\rho(\mathbf{r})$ vanishes. In addition to the maxima associated with atom positions, there are also saddlepoints where the curvature is positive in one direction and negative in the two others. Saddlepoints are located somewhere between the nuclei and are usually termed "bond critical points". The next step is to identify gradient paths, i.e., curves, such that the gradient vector $\nabla\rho(\mathbf{r})$ is tangent to it in every point. Paths that originate at a bond critical point and lead to atoms can be thought of as corresponding to bonds. We perform this topological analysis on the electron density with the program FAST [39], the results for the bond critical points and the path for the model being shown in figure 5.6.

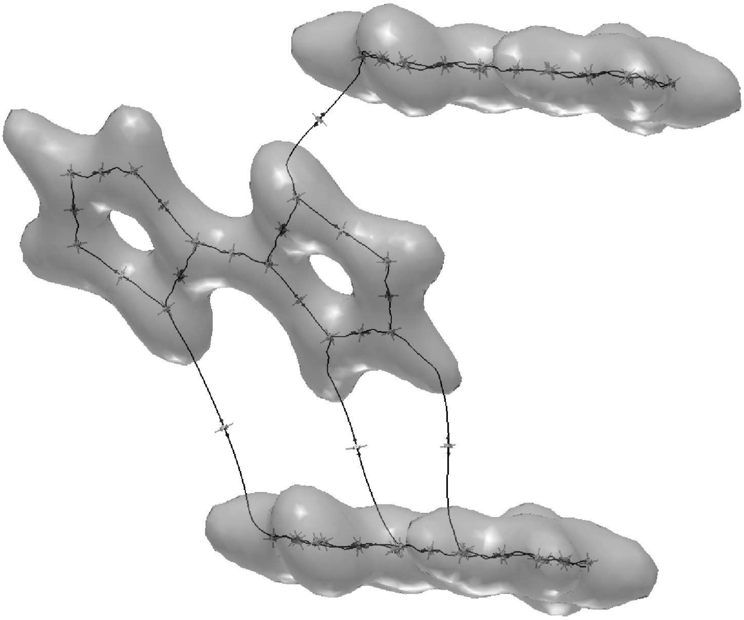

Figure 5.6: Electron density isosurface for a bithiophene cluster with the orientations as found in the crystal structure. The lines connect inter- and intramolecular critical points in the charge density according to the Bader description of "Atoms in Molecules" [15] and they define the bond paths.

We would anticipate that those vibrations that change most on going from the calculations for isolated molecule to the Γ-point calculation would involve the greatest change in the lengths of the intermolecular bonds calculated above. This expectation is fulfilled, the greatest changes in intermolecular bond-lengths being for modes observed at 721, 847, and 1071 cm^{-1}, these also being the modes for which the agreement between observed and calculated spectra is least satisfactory. The greatest intermolecular bond distortion is for the mode at 721 cm^{-1}, for which the agreement between observation and calculation is particularly troublesome. It would seem that the bond paths calculated from the electron density do indeed illustrate the most important intermolecular interactions and it may be possible to develop a force-field using these for future molecular dynamics simulations of related systems.

5.4 Conclusions

An understanding of conduction in polymers requires reliable electronic structure calculations and a reliable description of static and dynamic disorder. In the present paper we have shown that at the appropriate level, DFT is capable of reproducing the structure and dynamics of bithiophene, which is the dimeric analogue of polythiophene. We can therefore conclude that this method is suitable for structure and dynamics of larger systems and further that the calculated electronic structures are reliable. Comparisons of DFT calculations with IR and Raman spectra have the disadvantage that peak intensities vary strongly and are difficult to calculate. Comparison of frequency data alone can be risky in systems as large as bithiophene. Further, these spectroscopies measure at the long-wavelength limit and provide no information on important interactions that lead to dispersion. In the present work we have gone much further than an isolated molecule calculation, and though the agreement between observation and calculation improved considerably, the residual differences in the region above 750 cm^{-1} seem to be at the limit of the technique. For the DFT method as used in the present work, dispersive interactions are missing, and in a molecular crystal such as bithiophene this could easily be the main source of the residual error. We could of course scale these differences out, because the calculated spectral profile is rather good, but that is not the aim of the present work. The intramolecular rotational potential is very weak but this is increased considerably by the intermolecular interactions that also affect some relatively high-frequency vibrations. A convenient method of visualizing these interactions, and understanding how they affect the dynamics, is by finding bond paths in the electron-density maps of a cluster model. These could be useful in understanding local disorder that is important in the conductivity of the polymeric system.

Acknowledgment

We gratefully acknowledge F. Zerbetto for allowing us to use the INS spectrum, and L. D. A. Siebbeles for useful discussions. This work was partly financed by The Netherlands Foundation for Fundamental Research of Matter (FOM).

Chapter 6

Signatures of intramolecular disorder in thiophenes

6.1 Introduction

Chapter 4 showed the sensitivity of the 200−550 cm^{-1} range of an INS spectrum towards the inter-ring dihedral angle in bithiophene and very similar sensitivity will be shown later in this work for rather small changes in the conformation of diglyme molecules (see chapter 9). In chapter 5 the INS spectrum of bithiophene was compared with calculated spectra of the molecule in its crystal structure both at the Γ-point and including phonon dispersion. The effects of dispersion are apparent for vibrations below 300 cm^{-1}, but they do not account for the underestimation of the vibrational frequencies as observed between 700 and 1200 cm^{-1}. We have also shown by calculation that the length increase of these oligomers stabilize the molecule towards a planar conformation, which can be understood as a gain in the electronic delocalisation of the molecular π-orbital.

In this chapter we continue to examine the oligomers via their INS spectra that we compare with our calculations starting from known crystal structures. As can be expected for molecules of similar chemical composition, we see spectral resemblance, but also some trends when comparing the oligomers. Specifically we will address the region of 700−1200 cm^{-1} where the calculations underestimate the vibrational frequency for each of the oligomers. A explanation for this discrepancy could be solid-solid phase transformation below the temperatures reported by Pelletier [31]. We have thus measured the INS spectrum of bithiophene at 20 K and 90 K in order to check for spectral signatures of such a transformation. No significant differences were found between the two spectra, that could account for the differences between calculated and observed spectra.

6.2 Bithiophene cell parameters

In this chapter we will compare different oligomers and a polymer of thiophene (consisting of 2, 4, 6 and many thiophene rings) by their INS spectra. For each of these molecules a herring bone type ordering is typical, where the consecutive rings are twisted in *trans* conformation and the molecules are ordered in a $P2_1$ space group.[§] Both 2T and quaterthiophene (4T) crystalize with two slightly different densities [31, 40, 25] each and the polymer (pT) orders in two very different crystals: either a herring bone type ordering or in a helical structure [41], where the successive monomers are oriented nearly *cis* [†].

In figure 6.1 we show the observed INS spectra of three thiophene oligomers and the polymer. These observed spectra were taken at the TOSCA spectrometer below 30 K. This figure also shows the calculated spectra of isolated molecule oligomers using DMOL^3[¶] and of crystal structure polythiophene using the plane wave DFT package VASP-4.6 [34]. [‡] The large peak at 720 cm^{-1} in the observed spectrum of 2T is an out-of-plane mode where the hydrogens at the end of the oligomer chain have the largest vibrational amplitude. It appears in IR spectra at 698 cm^{-1} in the temperature range from 9 K to 290 K (see [43]). Comparing with the other observed spectra (4T, sexithiophene (6T), pT), we note that this specific mode is largely suppressed for the other oligomers (relative to the total of vibrations for each oligomer), but it reappears in the polymer, albeit less intense. This trend can be explained for the oligomers by the fact that the relative amount of “outer-ring hydrogens” is reduced for larger molecules. It contradicts, however, the pT observation of the peak in this energy region for the same reason, unless the observed mode for the polymer is not related to this specific normal mode of vibration. For bithiophene all the modes just above 600 cm^{-1} are underestimated by our calculations. Of the observed spectra in this energy range the major peaks shift slightly to lower energies with increasing chain length, but even for polythiophene a clear underestimation of the peaks at 800 and 870 cm^{-1} is evident in the calculations.

Bithiophene is a rather soft crystal with a melting temperature just above 30 °C. Pelletier has refined the crystal structure of bithiophene and reported the cell parameters in the temperature range 123−233 K as shown in figure 6.2. Another slightly denser packing (unit cell volume 382.8 Å^3 vs. 385.5 Å^3 @173 K) was reported by Chaloner [40] who allowed for a 15% phase of *cis* conformation of the two rings in his refinement. Apart from the complications that arise from the disorder while calculating the INS spectrum, the cell parameters that are needed as an input for the solid state DFT calculations are not available at 0 K. In figure 6.2 the cell parameters derived from x-ray diffraction by Pelletier are plotted, together with a linear extrapolation and two sets of geometry optimisations (including the cell parameters) using VASP. Both these DFT optimisations of the cell parameters are projected on the temperature range from 133 K to 0 K merely for plotting convenience and the data points (more than 200 optimisation steps) are not related to the temperature scale. Cell parameter determination of soft condensed matter using the DFT method is known

---

[§] The polymer adopts a similar herring bone ordering perperdicular to the molecular main axis, but the unit cell in the direction of this axis not defined

[†] The helix structure was suggested by Cui et al. [41] and will be address later on in this chapter

[¶] We used the DND numerical basisset in DMOL^3, together with the VWN local and BP nonlocal functional. The basisset cutoff was set to 5.5 Å and the Hessian was calculated from 0.05 Å displacements.

[‡] For the plane-wave calculation a energy cutoff of 500 eV was chosen together with the PBE [42] pseudo potential, automatic k-point generation and the Hessian matrix was calculated using displacements of ±0.05Å.

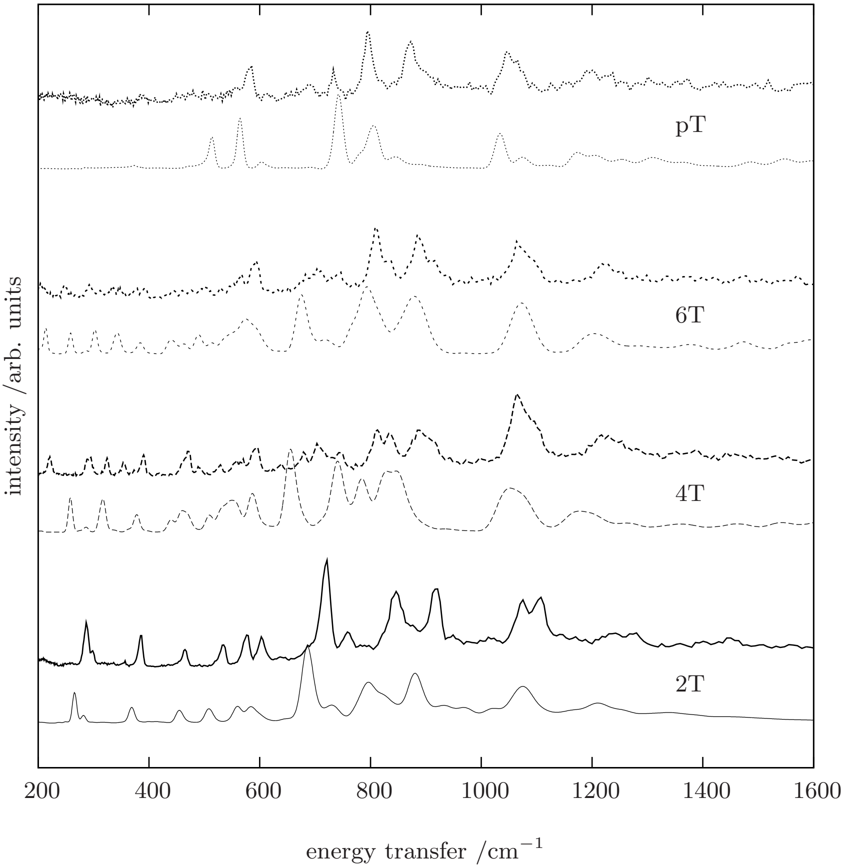

Figure 6.1: INS spectra (observed and calculated) of bithiophene (2T), quaterthiophene (4T), sexithiophene (6T) and polythiophene (pT). The observed spectra are plotted with a thick line. The calculated spectra (thin line plots) were obtained starting from the known crystal structure.

to be troublesome since the long range Van der Waals interactions are typically not accounted for correctly, yielding to both overbinding or repulsion, depending on the chosen functional [44]. According to Johnson [44] the PBE [42] functional we use in our calculations underestimates the binding energy of a T-shaped dimer of two benzene rings by a factor of two roughly. The herring bone ordering of thiophene oligomers resembles this conformation to some degree, and we should keep in mind that the intermolecular binding forces are too weak in our calculations. Without correcting for this discrepancy we proceed and optimise the atomic positions and cell parameters of bithiophene twice. Starting from exactly the same input, the two DFT optimisations yield quite different cell parameters that shrink the cell from 382.7 $\mathring{A}^3$ to 369.35 and 370.8 $\mathring{A}^3$ (cf. 372.4 $\mathring{A}^3$ by extrapolation). The DFT calculations demonstrate (within the limitations of DFT described above) the existence of at least two local minima, of which the geometries are rather similar. Underestimation of the Van der Waals binding will result in a cell that is too large, which suggest the correct cell volume at 0 K is still smaller than 369 Å^3.

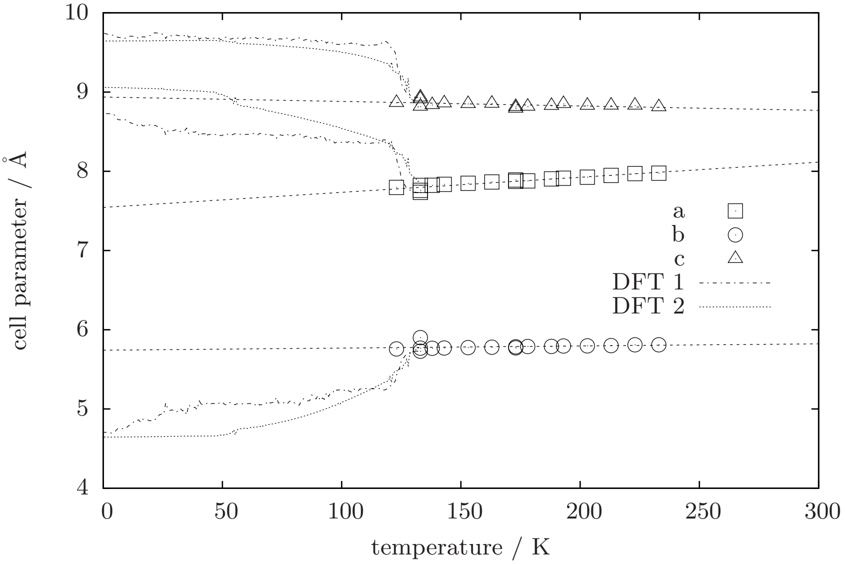

Figure 6.2: Temperature dependence of the cell parameters of bithiophene according to Pelletier [31]. The data are plotted with symbols and extrapolated linearly (dashed lines). Two approaches can be taken to estimate the cell parameters at 0 Kelvin: use the extrapolated values (straight lines) or take the DFT optimized values (dotted and dash-dotted lines). The extrapolated parameters at 0 K are (fixed) input for the Vasp vibrational calculations. The intermediate values of the DFT optimisation are plotted from 133 to 0 K, but are not related to the temperature scale.

We can expect the intermolecular forces in these different structures to have a distinct impact on the soft modes in the INS spectra, which figure 6.3 confirms. The inset of the figure shows that the effect of the lattice parameters is mostly absent for higher energies, although the crystal structure from the second DFT optimisation attempt yields a remarkably different result. What is evident from this figure is not which cell parameters are correct, but that rather small changes in the cell volume will change the INS spectrum significantly. As mentioned by Hermet et al. [45] a proper calculation of the soft modes requires an investigation of dispersion in these modes, which we do not report in our work, because of convergence problems in the optimisation of the supercell needed for phonon calculations.

To resolve the problems concerning the cell parameters, obviously one should obtain the diffraction pattern at the temperature of the INS experiments. What we *can* learn from the calculations using the cell parameters at 133 K or any parameters estimated so far, is that they can yield to quite different INS spectra (without taking dispersion into account), as shown in figure 6.3. The temperature dependence of the cell parameters as reported by Pelletier seems to suggest that the parameters at 0 K are quite different from those at 133 K as shown in figure 6.2.

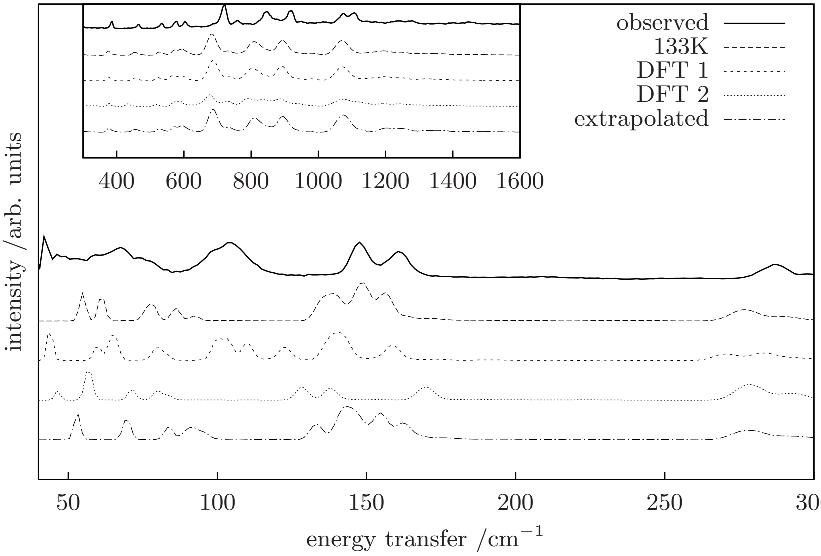

Figure 6.3: Vibrational differences due to different cell parameters. None of these spectra line up with the observed spectrum of bithiophene, but they do show the INS sensitivity to changes in cell parameters. The cell parameters are taken from: crystal data reported by Pelletier [31] (133K), DFT geometry optimisation of "atoms + cell" (DFT 1 and DFT 2) and linearly extrapolated values from the data of Pelletier (extrapolated).

In regard to the charge transfer and electron-phonon coupling in materials like oligothiophenes, we note here that the validation of our DFT calculations by comparison to INS spectra not only determines the local conformation of the molecules in poorly crystalline materials. From the same DFT calculations one can extract the electron charge density, the intermolecular coupling via phonon dispersion and the amplitude of vibrational displacements of the atoms that couple the molecules electronically. The soft modes of vibration are of interest in this respect, but also the intermolecular distances and the "intramolecular" vibrations that change the intermolecular closest contact distances. In the next section we address those "intramolecular" modes of which the peak position in the spectra is underestimated.

6.3 Vibrational consequences of disorder

Both Chaloner [40] and Pelletier [31] report of disorder in their crystals and Chaloner assigns 15% of the crystal to bithiophene in a *cis* conformation. With increasing oligomer length the isolated molecule overcomes the steric hindrance between its thiophene units as described in chapter 5 and one can expect the crystal structure to be less prone to disorder as the planarity of the molecule is forced by the gain in delocalisation of the π orbitals electrons. On the other hand, the packing of very long chains complicates a proper crystalisation of polymers in general. As Hermet et al. [45]

have reported, the low energy INS spectra of oligomers of thiophene shows a marked sensitivity towards intermolecular interactions due to the crystal packing, resulting in phonon dispersion.

Our findings in 6.2 (neglecting phonon dispersion) suggest that these interactions are rather sensitive to the cell parameters, which in case of bithiophene are significantly temperature dependent. As mentioned before, the DFT calculations are performed at 0 K, where as the "observed" parameters are obtained at 133 K and since both Chaloner and Pelletier report a certain amount of disorder from their XRD experiments, we have investigated the vibrational consequences of a *trans* to *cis* conversion of both bithiophene and polythiophene.

Returning to figure 6.1 we note that both 2T and pT calculations underestimate the modes between 700 and 1200 cm^{-1}. Unlike packing disorder due to vibrational anharmonicity or thermal disorder, this type of molecular conversion from *trans* to *cis* can be expected to influence directly the vibrational modes above 700 cm^{-1}.

In comparison, the infrared spectrum of bithiophene is recently measured in the temperature range 9−290 K by Hermet et al. [43], and it shows an intense peak that remains at 700 cm^{-1} in this temperature range, corresponding rather better with DFT calculations than the INS spectrum does. We anticipate that this up-shift in INS peak positions that is apparent for all modes above 700 cm^{-1} stems from the preparative conditions of the INS experiment at TOSCA spectrometer where samples are typically quenched rapidly to liquid nitrogen temperature, before insertion in the cryostat.

As a result of rapid cooling the rather soft crystal structure of bithiophene takes up a strain that forces intramolecular disorder or reorientations. Testing this hypothesis is rather difficult, even if we assumed a 15% *cis* contribution in a constructed supercell of bithiophene as the cell parameters would adapt to the strained conformation and the packing of *cis* to *trans* is unknown. We have taken a much simplified route and calculated only the INS spectrum of a small cell that contains one bithiophene with an inter-ring twist of 180°(resulting in *cis* conformation). Since the calculated spectrum of polythiophene also underestimates the frequencies, we have constructed a hypothetical unit cell that holds one twisted pair of an infinite chain of thiophenes in 1 dimension (the cell parameters in the perpendicular directions are 10 Å). Similar to bithiophene, we can compare the results from our proposed structure to those from crystal structure data. As can be seen from figure 5.5 the local minimum of the *cis* conformation of an isolated oligomer is shifted with respect to the 180° dihedral angle and so here too, we need to optimize the atomic positions.

By imposing the periodic cell on the molecule, we force its linearity and as a consequence the steric hindrance between hydrogens on neigbouring cells will cause the ionic optimisation to twist the pair of rings in the unit cell away from their common plane. The dihedral angle of the (local) ground state molecule (with the cell parameters fixed) is 50°, but the polymer segment does not return to its *trans*-conformation. The bidimensional crystal structure of pT, as derived by Brückner et al. [46], shows the herringbone arrangement but contains no information regarding the dimension along the molecular main axis. In their work, they have attempted to retrieve structural information regarding the chain axis, by inter-chain displacements along the chain, but they neglect the possibility of (partial) *trans* to *cis* transformation in the chain. From their bidimensional structure they propose an orthorombic unit cell with

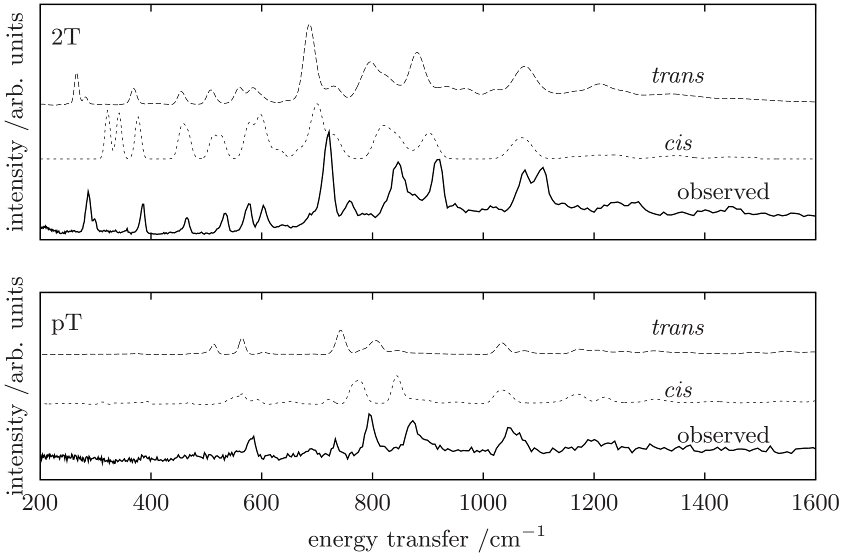

Figure 6.4: INS spectra of the *cis* and *trans* conformation of two thiophene rings in bithiophene (2T) and polythiophene (pT). These calculations were done on a unit cell that contains only one pair of twisted thiophene rings. The calculation of the twisted pT agrees significantly better than the *trans* conformation. The same can be concluded for 2T regarding the peak positions, but the intensity distribution is wrong.

a hypothetical cell parameter along the chain-axis of 7.753 Å. This unit cell serves as a starting point from which we generate a $1 \times 2 \times 2$ cell to calculate the INS spectrum, including the phonon contributions.

The resulting vibrational spectra of 2T and pT are shown in figure 6.4.

The spectra show that the observed peak positions above 700 cm^{-1} are better reproduced by the calculations when the thiophene rings are oriented (near) *cis*. Considering that these calculations are based on a rather simplified model where the twisted molecule is isolated from its crystal environment, the agreement is rather good. We notice that our model system, based on two rings, implies a *trans* to *cis* transformation of 100 % in such a small model, and as such the amount of disorder as suggested by Chaloner is 100 % instead of 15 %. Therefore our findings show only a trend in INS spectra, due to disorder. In chapter 4 we successfully demonstrated the sensitivity of the spectral region $200 < \Delta E < 500\text{cm}^{-1}$ toward the intermonomer dihedral angle. Figure 6.4 shows poor agreement in this region, confirming the conclusions of chapter 4, but for pT the spectral quality in this region is rather poor, and we focus on the region $\Delta E > 600\text{cm}^{-1}$. The spectral improvement in the case of polythiophene is quite remarkable, even though the periodic boundary conditions limits the infinite chain to remain strictly linear. Without these restrictions the steric hindrance between two rings could be removed by bending the rings on their connecting α carbons, whereby the rings remain in the same plane. Cui et al. [41] have suggested from their semi-empirical calculations that the local minimum near *cis* conformation of an

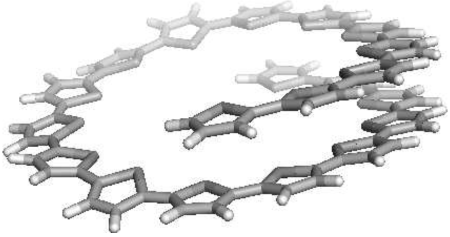

Figure 6.5: The optimized structure of a helix *cis* conformation of 20 thiophene rings.

infinite chain of thiophene would result in a helical conformation. To test whether such an conformation would result in a spectrum similar to that of the *cis* conformation of figure 6.4 we have generated a helix using 20 thiophene rings (20T) by minimising the energy with TINKER v4.2 [47] using the MM3 force-field [48]. The structure was further optimized using the PWC functional [49] and the standard double numeric basis set in DMOL^3 [50], with which the Hessian was then calculated. The resulting helix structure is shown in figure 6.5.

The model is an isolated molecule and therefore the phonon spectrum was taken from the measured INS spectrum and convoluted in CLIMAX [32] to generate from the Hessian the calculated INS spectrum as shown in figure 6.6.

The spectral agreement of the isolated molecule is not as good as for the infinite linear chain, but it does confirm the suggestion that the measured INS spectra are of a polymer in a *cis* conformation. For such large molecules (142 atoms) the DFT calculations are rather time consuming and to find the global minimum energy conformation would require either much computing resources or experimental structural information like the small angle neutron scattering (SANS) structural study of Aim et al. [51] on poly-2-butyl-thiophene. Nilsson et al. [52] have reported of similar functionalised polythiophenes and depending on the pH of the solutions, they find helix formation [§]. As mentioned by Ferretti et al. [13] one of the major concerns in planar polythiophene is the poor intermolecular overlap. Much like discotic materials for the same type of applications, the helical polythiophene would benefit from the π overlap perpendicular to the plane of each monomer (parallel to the helical screw axis), thereby creating a "short-circuit" in the helical column.

Our interest in the $\Delta E > 600\text{cm}^{-1}$ region of the spectrum is not only related to an apparent amount of disorder, but it also stems from our "atoms in molecules" investigation in chapter 5, where we found bond paths in the DFT electron density connecting a hydrogen of each molecule to a carbon on its neighbouring molecule. The intense peaks in the spectrum are related to normal modes where hydrogens are displaced out of the molecular plane, and we may expect these modes to have a large impact to the intermolecular charge transfer.

As stated in the introduction (section 1.2.3), one of the purposes of our investigations

---

[§] Although the suggested helical conformation of unsubstituted polythiophene is not the global minimum energy conformation, the effect of the sidechain synthesis could perhaps be mimicked by dissolving a cation in the polymer, which then (hypothetically) locates at the screw axis of the helix, similar to what is observed in PEO polymer electrolytes [53].

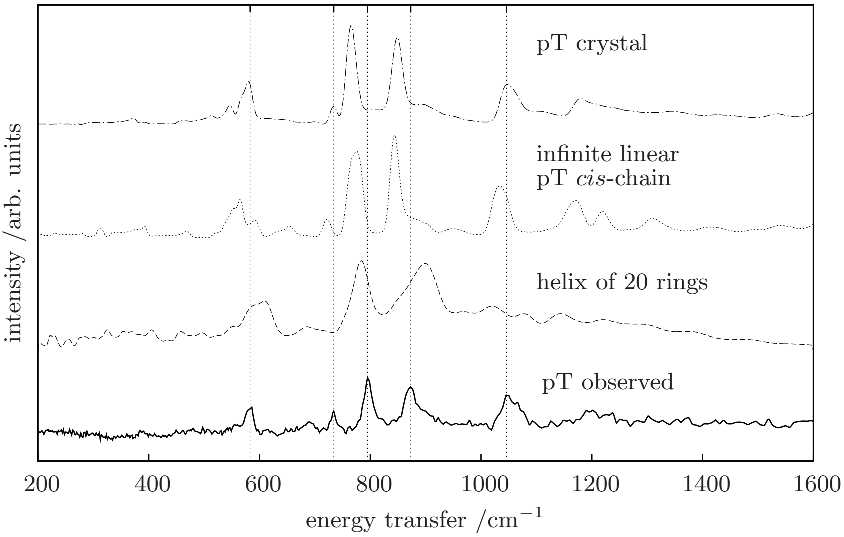

Figure 6.6: INS spectra of a helix structure of 20 thiophene ring compared with the observed spectrum. For comparison the pT *cis* conformation calculated spectrum is shown as well. The latter shows better spectral agreement, but it should be noted that the helical conformation is obtain from a course minimisation routine and likely other minima exist.

is to assess the sensitivity and applicability of the combined DFT/INS method in determining local molecular conformations. The succes of plane wave DFT codes is partly based on the use of pseudo potentials (see section 2.3.1) and we have compared different combinations of pseudo potentials with respect to the quality of the computed INS spectrum. Only very recently, we found that the "standard" pseudo potentials combined with a Monkhorst-Pack k-point scheme (1×1×1) yields a calculated INS spectrum that reproduces the observed INS spectrum remarkably well over the whole range above 300 cm^{-1}. All other calculations so far (as reported by us and others [43]) are in better agreement with the IR spectrum [43] and this led us to test the hypothesis of *trans−cis* disorder as mentioned by Chaloner [40]. The recent calculations that show excellent agreement with the observed INS spectrum completely mitigates against our suggestion of disorder, since the discrepancy is completely removed. However, the near-perfect description of the INS spectrum implies in turn a contradiction with the IR spectrum and at present no consistent conclusion can be drawn from these observations. It remains to be examined, which choice of k-point selection for the plane wave basis set is the most reliable.

Finally we would like to emphasise that the interest in a more precise spectral description in this energy region ($\Delta E > 600\text{cm}^{-1}$) stems from our investigations (prior to these recent findings) that better agreement may also be found by introducing *trans−cis* disorder. In partially disordered materials, this method could serve to find the local conformation of the molecule. As a conducting polymer, the normal modes in this energy region will effect the intermolecular charge transfer and as such a proper description of these modes is required.

Chapter 7

Charge transfer between thiophene rings in vibrationally excited states

published in: *Phys. B 350, 220 (2004),*
L. van Eijck, K. Senthilkumar, L. D. A. Siebbeles and G. J. Kearley

Abstract

The charge-transfer integral (CTI) between monomers in polythiophene is important for the electrical properties of the polymer. Torsional oscillations of the monomers are thought to play a key role in reducing the CTI, but the present study shows that other out-of-plane vibrational modes may play an even more important role between 10^{-12} and 10^{-14} timescale on which charge transfer occurs.

7.1 Introduction

Conducting polymers are π-conjugated polymers with semiconducting properties [26]. They can be used as an economic alternative for silicon based electronic devices, like transistors and solar cells. Polythiophene is a model system for conducting polymers, and in the present work we study the oligomer: bithiophene. This is appropriate because one of the key parameters in the conductivity is charge transfer between thiophene rings. This occurs on the timescale of 10^{-12} to 10^{-14} sec, which corresponds to the period of molecular vibrations. These displacements may either help or hinder the charge transfer process. We have therefore measured the vibrational displacements of the atoms using inelastic neutron scattering (INS) and characterized these in some detail using ab initio calculations [54]. These calculations provide the normal coordinates with which we determine the vibrations that are important in the charge transfer process. The main effect of the crystal lattice is to change the dihedral angle between the two aromatic rings from 27° to a planar configuration, and we have

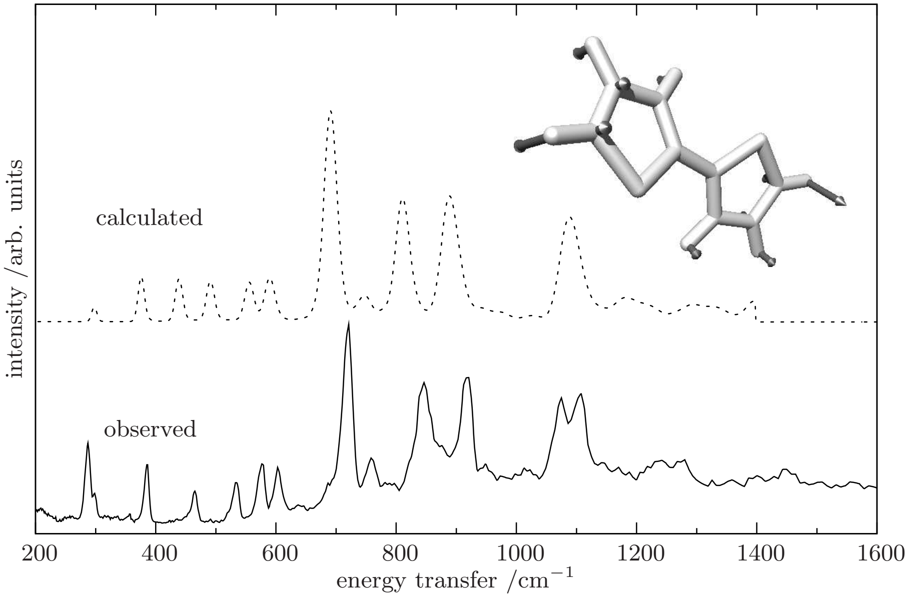

Figure 7.1: The observed and calculated spectra of bithiophene. The inset shows the molecule with its scaled atomic displacements.

recently shown the spectral consequences of changing this angle [37]. For reasons of comparison we concentrate essentially on the low-frequency modes of the gas-phase structure.

7.2 Experimental and methods

We used the vibrational spectrum reported by Esposti et al. [29] from the TFXA [55] spectrometer at ISIS. In order to obtain precise assignments to the vibrational modes we calculated the INS spectrum via ab initio methods. Atomic positions were taken from the reported crystal structure [31] and the finite displacement method (both positive and negative) was then used to obtain the dynamical matrix. This was then transformed to mass-dependent coordinates and diagonalized to obtain the vibrational eigenvalues and eigenvectors. The program Climax [32] was used to calculate the neutron spectral profile. The energy of each displaced structure was calculated using density functional theory, DMol^3 [35] with the general gradient corrected functional Perdew-Wang (1991) and a double-numeric quality basis set with polarization functions (DNP). Normal modes for the gas-phase molecular conformation were calculated in the same way. Each normal mode distorts the equilibrium structure of the molecule and for these displaced structures the charge-transfer integral is calculated. The wave function of an excess positive charge is approximately a linear superposition of the highest occupied molecular orbitals (HOMOs) on the individual thiophene rings. Hole-transport along a polymer chain can be described with the tightbinding Hamiltonian with nearest-neighbour interactions only [56, 14]:

$$\mathcal{H} = \sum_{n} \varepsilon_n(\mathbf{R}) a_n^\dagger a_n + \sum_{n,n\pm1} J_{n,n\pm1}(\mathbf{R}) a_n^\dagger a_{n\pm1}. \tag{7.1}$$

In equation (7.1) $a_n^\dagger$ and a_n are the creation and annihilation operators of a charge on the n^{th} thiophene ring, $\varepsilon_n(\mathbf{R})$ is the site-energy of the charge when it is localized at this ring and $J_{n,n\pm1}(\mathbf{R})$ is the charge-transfer integral (CTI). Both the site-energies and the CTI depend on the intramolecular and intermolecular geometrical degrees of freedom, denoted as $\mathbf{R}$. Within the framework of DFT the CTI corresponds to the off-diagonal matrix elements of the Kohn-Sham Hamiltonian of the system:

$$J_{n,n\pm1} = \langle \phi_n \left| h_{KS} \right| \phi_{n\pm1} \rangle \,, \tag{7.2}$$

with ϕ_n the HOMOon an individual thiophene ring.

The CTI was obtained with the Amsterdam Density Functional (ADF) theory program [57] by using the molecular orbitals of the individual thiophene (fragment orbitals) as a basis set in a subsequent calculation on bithiophene. ADF provides the overlap matrix, $\mathbf{S}$, the eigenvector matrix, $\mathbf{C}$, and the diagonal eigenvalue matrix, $\mathbf{E}$. The matrix elements of the Kohn-Sham Hamiltonian are obtained from $\mathbf{S}$, $\mathbf{C}$ and $\mathbf{E}$, since $h_{KS}\mathbf{C} = \mathbf{SCE}$, and consequently $h_{KS} = \mathbf{SCEC}^{-1}$. The results reported below were obtained with an atomic basis set of Slater-type orbitals (STOs) of triple-ζ quality including two sets of polarization functions on each atom. The Local Density Approximation by Vosko, Wilk and Nusair (VWN) was used together with gradient corrections of the Perdew and Wang 91 (PW91) functional for the exchange and correlation.

7.3 Discussion

The observed and calculated INS spectra were found to be in reasonable agreement. A spectrum was also recorded at 90 K (the temperature of the crystal structure determination) to ensure that residual differences between the observed and calculated spectra did not arise from structural changes (figure 7.1). The essential spectral differences between the two temperatures are from the Debye-Waller factor. We conclude that the ab initio calculation for the gas-phase structure will provide a good representation of the isolated molecule vibrations. The CTIs for selected modes are collected in table 7.1. A full analysis of these results in terms of the component orbitals goes beyond the current paper and will be given in a subsequent publication. Many of these results can be understood in fairly simple terms by considering the factors affecting the overlap of the p_z orbitals on the carbon atoms that connect the two rings. A surprising result is that the torsional mode between the 2 rings at 50 cm^{-1} has comparatively little effect on the CTI. The molecule is relatively non-planar and so the effect of the overlap of p_z orbitals between the rings improves for the mode denoted “a” in which the orientation moves towards planar, and reduces for motion in the opposite sense, “b”. The mode 128 cm^{-1} , however, distorts the ‘molecular plane’ and motion in either direction has the same effect. The more antisymmetric mode at 286 cm^{-1} also shows similar effects on the CTI, but in this case the effect is larger. The main character of the mode at 671 cm^{-1} is a symmetric ring-breathing. As the rings enlarge (a) the CTI increases considerably, and as they decrease (b) the CTI

Table 7.1: The charge-transfer integral (J) for vibrationally distorted conformations, a and b being at opposite extremities. Frequencies are calculated for the gas-phase molecule. The third column lists the absolute value of the difference in J compared to the value J_{eq} of the molecule in the vibrational groundstate conformation.

Mode /cm^{-1}	-J/eV	$\lvert J - J_{eq}\rvert$ /eV
equilibrium	1.399	0.000
1050a	1.501	0.102
1050b	1.426	0.026
671a	1.493	0.094
671b	1.410	0.011
517a	1.393	0.006
517b	1.393	0.006
463a	1.787	0.394
463b	1.336	0.063
286a	1.307	0.092
286b	1.322	0.077
128a	1.354	0.045
128b	1.328	0.071
50a	1.402	0.003
50b	1.331	0.068

also increases, but only slightly. Similarly, there is also an important component of a C$-$C stretch in the mode at 1050 cm^{-1} , and again the enlarging sense (a) causes a considerable increase in the CTI. The other mode that shows a dramatic increase in the CTI is at 463 cm^{-1}. A provisional analysis of the orbitals suggests that in this mode the displacements (shown in figure 7.1) cause an important contribution of the p$_x$ orbitals of both rings which provide $\sigma(p_x)$ overlap in addition to the π-overlap and hence increase in CTI.

7.4 Conclusions

Torsional motion between the rings is a low-energy process even in the solid state and it will tend to play an important role in charge transfer. However, if the local field distorts the inter-ring angle then small oscillations around this angle will have little effect on the charge transfer. Other out-of-plane motions have surprisingly large effects on the charge transfer and whilst it is sometimes straightforward to understand these in terms of overlap of atomic orbitals, a deeper understanding of all effects will have to await a proper analysis of the molecular orbitals.

Acknowledgement

We are grateful to Profs Esposti and Zerbetto for the use of the INS spectrum.

Chapter 8

Charge transfer and condensed phase dynamics

8.1 Introduction

The conductivity in π-conjugated polymers has been studied via the calculation of the splitting of energy levels, when two dimers are brought into proximitity (see for instance Cornil et al. [58]), resulting charge-transfer integral (CTI). The charge transfer depends largely on the hole mobility that in turn depends on the constructive or destructive overlap of the π-orbitals. Work reported by Brédas et al. [23] and Cornil et al. [58] shows systematically how dimerisation of oligothiophenes introduces a splitting of the higest occupied molecular orbital (HOMO) and the lowest unoccupied molecular orbital (LUMO). One can expect this intermolecular charge hopping to influence the overal charge mobility in a device, and in case of solar cell applications the π-overlap between long chains contributes to the polaron mobility. When both chains deform under influence of a charge on either, a polaron complex is formed that further complicates the description of charge transfer when this state turns into a local minimum.

The surface crystal structure for polythiophene was refined by Brückner et al. [46] who suggested two structures of $P2_1/a$ and $P2_1/n$ symmetry, which differ only in that the two chains per surface unit cell are shifted with respect to each other over half the repeat length of the *trans* chain in the direction of chain. Puschnig et al. [24] has calculated the bandstructure of both cells and showed that the $P2_1/a$ structure is expected to be the best hole conductor of the two, due to larger HOMO splitting in X direction near the Γ-point. These results were further supported by Ferretti et al. [13] recently, who have calculated the CTI from plane wave DFT methods. Confirming the work of Brédas and Cornil et al. in the crystal structure of pTthe largest constructive overlap of orbitals results in a large CTI. In the X direction of the crystal the molecules stack with π overlap, though the tilt of molecules reduces the overlap. In either case of the two crystals suggested by Brückner, the overlap with the other molecule (having another mirrored tilt angle) is signifantly lower.

However, both Brédas and Cornil show that the level splitting due to inter-chain interaction decreases with increasing chain length, and therefore the intra-chain charge transfer will play an important role for solar cell applications, where the polymer is used, rather then the oligomers. The intramolecular CTI is found to be bigger than the intermolecular CTI [13]. Recently Meisel et al. [12] have reported on lattice energies of localized polarons on an isolated infinite pT chain, obtained for the first time using (plane wave) DFT and correlated these energies to phonon modes obtained from IR measurements. Unfortunately, our INS data shows only a very broad feature in the region below 300 cm^{-1}, probably due to poor crystallinity of the sample.

Chapter 7 showed how the charge-transfer integral (CTI) can be influenced when the molecule (bithiophene in that case) is in either of the two extreme conformations of a certain vibrational excited state. The conformational distortions for each vibrational state were derived, by validating a DFT calculated potential energy surface (PES) via the harmonic approximation to the observed INS spectrum, after which the PES is used to calculate the amplitudes of the eigenvectors relatively. Experimental INS spectra, much like the DFT calculated spectra, report the available vibrational states up to an energy level well above the accessed level at ambient temperature, and the experiment itself is done typically below 30 K [§].

What is thus not probed in this approach, is how these states are populated when the given material is used at ambient temperature. In principle this population can be estimated by performing molecular dynamics, but the extraction of the generated dynamics is not performed in terms of the normal modes like described in section 2.1.1, but rather via the autocorrelation function G_s (section 2.1.2). In this manner any anharmonicities due to intermolecular interactions in the dynamics are included in the analysis.

The conversion of the autocorrelation function to $S(\mathbf{Q},\omega)$ then enables us to estimate the validity of the simulation by comparison to either QENS spectra or INS spectra as will be done in section 8.3.1. Independent of whether the simulation is based on force-field or ab initio methods, the equipartitioning of the kinetic energy over the atoms is implicitly classical, and hence the MD will populate states that are empty when the nuclear dynamics are treated quantum mechanically. An indication of how involved these calculations would become if the Born Oppenheimer approximation is not assumed, is given recently by Pavanello et al. [59] regarding the calculated vibrational spectrum of the very small dimer HeH^+.

8.2 Methods and computations

The molecular dynamics simulations are done with Tinker 4.2 [47] with the MM3 force-field [48], that is adapted with respect to those force constants for 5-ring dihedrals and the inter-ring torsional potential. Previously we have determined this torsional potential from DFT calculations (section 5.3.4) and here we do the same for the 5-ring dihedrals by z-matrix manipulation of the corresponding bending coordinated over a range of ± 5° using the BLYP functional [22] of Gaussian98 [60]. The resulting potential energy profiles are the input to which the force constants of the MM3 force-field are fitted. Table 8.1 shows how the parameters were adapted.

The simulations were done for 2T starting from a supercell (roughly $20\times20\times20$Å) that was build from known crystal structure data [31] and then minimized with respect

---

[§] the DFT calculated spectra here are implicitely at zero temperature

Table 8.1: The parameters of the MM3 force-field that were adapted by fitting to potentials derived from DFT calculations. The force constants (in units of kcal/mol/°) are adapted for the cos(2ϕ) and cos(3ϕ) potentials.

Internal coordinate	MM3	adapted
intermonomer C–C–C–C dihedral	10.0/2 0.0/3	0.8/2 0.0/3
intermonomer C–C–C–S dihedral	10.0/2 4.2/3	0.8/2 0.5/3
intermonomer S–C–C–S dihedral	10.0/2 4.5/3	0.8/2 0.2/3
intraring C–C–C–S dihedral	23.63/2 6.0/3	10.02/2 0.0/3
intraring C–C–S–C dihedral	29.50/2 0.0/3	13.71/2 0.0/3
intraring C–C–C–C dihedral	7.80/2 0.0/3	3.25/2 0.0/3

to the total energy. The simulations were run in the canonical (NVT) ensemble at a temperature of resp. 293 K with the non-bonded interactions included via Ewald summation. A timestep of 1 fs was used for the simulation and the trajectory (900 ps) was saved every femtosecond for comparison to INS spectra and 100 fs for comparison to the QENS spectra.

The QENS spectra are obtain from measurements on the Iris spectrometer at Isis on 2T, 4T and pT. The experiments are done at different sets of temperatures, below the specific melting temperatures of the materials, and the instrumental settings are given in section 3.2.2. The data are corrected for detector efficiency using the instrumental resolution function, converted to $S(Q, \omega)$ using the instrument specific software, and then fitted with one Lorentzian using in-house fitting routines. The DFT calculations from which we estimate the CTI were done with Gamess US [61] using hybrid B3LYP [62] functional and Pople's triple split N-311G basis set [63].

8.3 Discussion

8.3.1 QENS and INS versus MD

The MD can be validated by comparison to both QENS $S(Q, \omega)$ and INS $S(\omega)$ spectra and we start with an inspection of the quasi elastic broadening of 2T, 4T and pT. For each of these materials the quasi elastic signal is quite small, and the fitted data using one Lorentzian shows a rather small broadening (150 µeV on average). This complicates the analysis of the Q-dependence and the comparison of the different samples. In figure 8.1 we show a typical example of the quasi elastic broadening, together with the fitted widths of the different samples at the specific highest temperatures. Only for these highest temperatures we were able properly fit the data, and the data at lower temperatures gave unphysical fitting results, due to the small intensity of the broadening.

Consequently, the validation of the simulation via the calculated broadening from the MD is not feasible with the observed QENS signal and we turn to the INS spectra to test the validity of our simulations. To cover the energy range of the INS spectrum, a new trajectory is created with a timestep of 1 fs. The hydrogen trajectories of the simulations are converted to $S(Q, \omega)$ via the auto-correlation function and the result

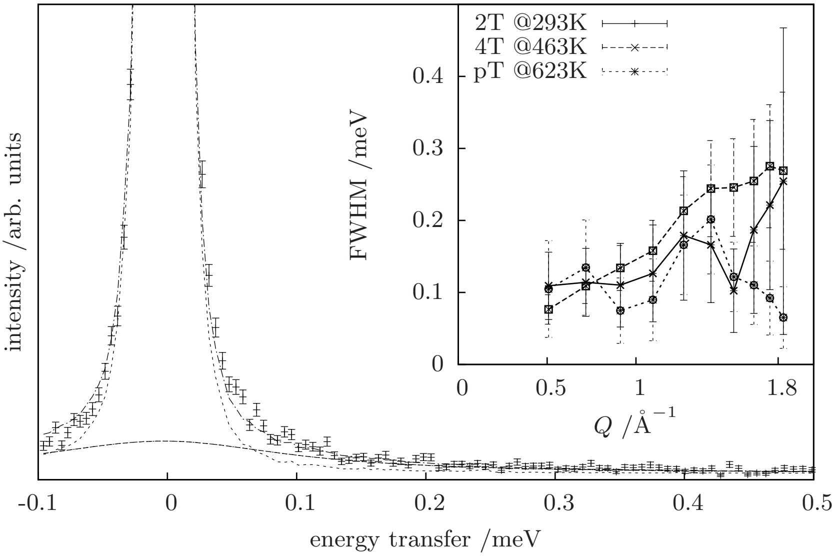

Figure 8.1: A QENS spectrum of 2T ($Q = 0.5$ Å^{-1}) showing the weak broadening typical of all (2T, 4T, pT) the fitted data. The inset shows the width (FWHM) of the broadening versus momentum transfer for each of the thiophenes at the highest specific temperature. Due to the weak broadening the error bars are rather large.

is shown in figure 8.2. As mentioned above, the distribution of the kinetic energy in the simulations in the canonical ensemble is based on classical mechanics, and as a consequence all available modes, far above $k_B T$, are occupied and one should expect discrepancies in the relative peak intensities in these MD-derived spectra, reflecting the consequences of the classical approach. We make no further attempts to line up the calculated spectra to the observed, since the aim here is to assign the specific frequency dependence of the charge-transfer integral to the calculated spectral peaks, that we in turn can now assign to the observed modes. The limiting factor in this procedure is the accuracy of the Fourier transform of the CTI, as will be shown below.

8.3.2 Charge transfer integral versus INS

To estimate the charge-transfer integral we extract several sets of conformations of one molecule from the MD trajectory, each set with a different time interval (1 fs, 10 fs), and for each conformation we calculate the molecular orbital (MO) energy levels. The energy splitting between the highest occupied molecular orbital and the one below (HOMO-1) is an estimate of the CTI ($J(t)$), with a correction for the difference orbital energies of the individual units of the dimer. Typically, this approach is taken when two (whole) molecules are placed in proximity to form a dimer and from the splitting one can estimate the degree of coupling between the molecules. Here we have taken the approach two steps further by forming a dimer from two thiophene monomer radicals, and by extraction of distorted molecular conformations

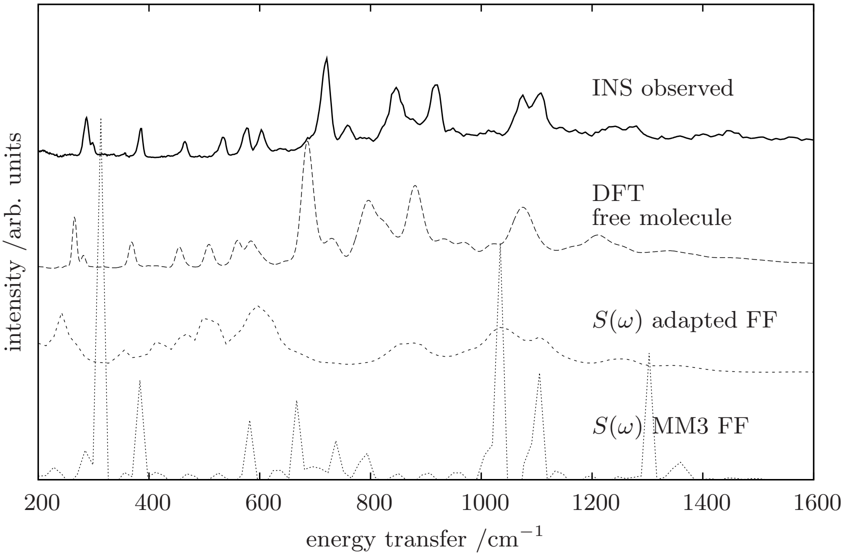

Figure 8.2: Calculated $S(\omega)$ at $Q = 1.8\text{Å}^{-1}$ compared with a free molecule DFT calculation and the observed INS spectrum. Although neither of the MD-derived spectra show very good agreement, the adapted force-field parameters do improve the correspondence with the observed spectrum. The intense mode observed at 720 cm^{-1} probably corresponds to the peaks just above 600 cm^{-1} for the adapted FF $S(\omega)$.

from our MD trajectories. These facts complicate the correction that is applied in this approximation, as some of the trajectory frames consist of molecular deformations of which individual monomers will have rather different orbital energies. When two such monomers from a single molecule have a rather different HOMO levels, the corresponding correction may exceed the splitting due to the monomer coupling, and the estimate of the CTI becomes imaginary. As a first approximation we therefore chose to omit the correction in the intramolecular CTI calculation, as it will poison our Fourier transformation. The consequences of this simplication will be addressed in later work. As shown in 5.6 the intermolecular electronic coupling of nearest neighbour molecules is between each "herring bone" pair in the crystal structure. As a comparison to the intramolecular CTI we also calculate the frequency dependence of the intermolecular coupling between two such molecules, by similar methods, but now using a subset of two neighbouring molecules from the MD trajectory.

The Fourier transform of the sets of charge-transfer integrals $J(t)$ within this limitation are compared to the observed and calculated (from MD) spectra in figure 8.3 for intramolecular charge transfer and in figure 8.4 for intermolecular charge transfer.

Considering the limited number of data points in each $J(t)$ set (intramolecular: 100 for the 10 fs set and 400 for the 1 fs set), we can only expect to make a coarse correspondence to the $S(\omega)$ of the MD and the observed spectrum. Figure 8.3 shows qualitatively, that $\mathcal{F}(J)$ couples mostly with the calculated modes at approximately 130, 300 and 820 cm^{-1}. The intermolecular $\mathcal{F}(J)$ shows a similar spectral dependence,

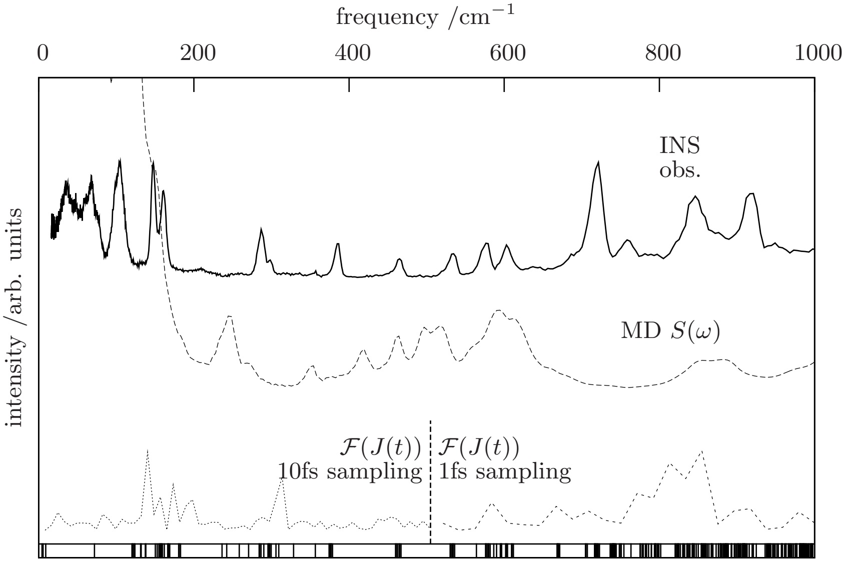

Figure 8.3: The Fourier transform of the intramolecular $J(t)$s compared to INS spectra (observed and calculated). The $J(t)$ is calculated from a set with a time interval of 10 fs between the conformations of the MD and a set with a 1 fs time interval. At the bottom of the graph the tic marks show the overtones and combinations of fundamental normal modes.

with an intense spectral feature at 180 cm^{-1} (see figure 8.4), and some contributions below 100 cm^{-1} that are absent for the intramolecular $\mathcal{F}(J)$.

The calculation of $S(\omega)$ from MD simulations via the auto-correlation function implies that we cannot relate this spectrum back to a more pictorial set of normal modes with the corresponding overtones and combinations. The spectral correspondence between the MD $S(\omega)$ and the observed and/or DFT $S(\omega)$ is not sufficient to reliably assign the peak positions to certain normal modes of vibration. Moreover, the features in $\mathcal{F}(J)$ do not line up precisely with the main nearest peaks in the MD $S(\omega)$, which suggests that the electron-phonon coupling that is being investigated is not simply related to any particular normal mode. From DFT calculations we can distinguish between the fundamental normal modes and the corresponding overtones and combinations. Although the $\mathcal{F}(J)$ in figure 8.3 and figure 8.4 are derived from the MD simulations and not from DFT calculation, we show at the bottom of these figures the overtones and combinations as derived from DFT. The coupling of J to dynamical distortions in the molecules are not necessarily related to the modes with the biggest amplitude in these figures. Indeed, one may expect small amplitude distortions or combinations of certain fundamental modes to couple stronger to the electronic states, than for instance hydrogen wagging modes. One should keep in mind that the MD simulations were done with harmonic spring-like bonds and that the corresponding electronic states were optimized self consistently from these MD extracted distorted structures. Assignment of the features in $\mathcal{F}(J)$ to a particular (set of) fundamental normal

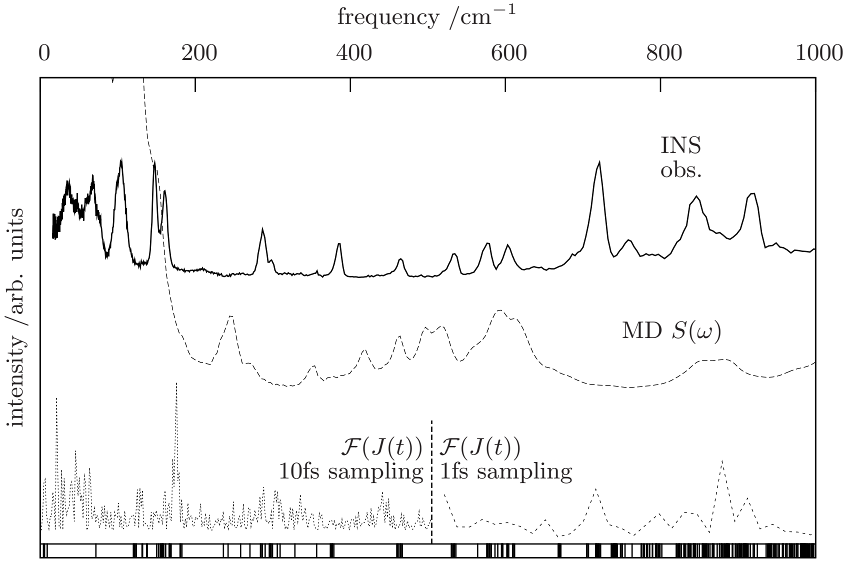

Figure 8.4: The Fourier transform of the intermolecular $J(t)$s compared to INS spectra (observed and calculated). The $J(t)$ is calculated from two data sets (1 fs and 10 fs time interval), similar to the intramolecular $J(t)$. At the bottom of the graph the tic marks show the possible overtones and combinations of fundamental normal modes.

mode(s) could improve the understanding of the results presented here, and for that a rather good spectral agreement is required, to be able to distinguish the fundamental modes from near-degenerate combinations or overtones.
One can either turn to DFT based MD simulations, or find better force-field parameters for a classical MD simulation.

Part II

Polymer Electrolytes

upon addition of TiO2 nanoparticles

Titanium dioxide (TiO_2) is very commonly used in toothpaste and paint as a pigment. It is a white inorganic semi-conductor that can be used as a photocatalyst. The typical size of the powder particles is of the order of tens of micrometers, and to create more catalytic surface the particle diameter can be reduced. Nanocrystalline (20−50 nm diameter particles) TiO_2 is often used in different fields of material science, for instance in organic solar cells (the Grätzel cell) and fuel cells (see e.g. [64]). Besides TiO_2 other metal oxides have been tested like Al_2O_3 and SiO_2 and they are generally termed *nanoparticles* or *filler*. When dispersed in a polymer electrolyte, the filler material increases the conductivity of the electrolyte up to nearly 4 orders of magnitude [2],[65] using only 10 wt% of the filler. The increase in conductivity has been observed using different electrolytes and different inorganic filler materials: Krawiec et al. [65] used Al_2O_3 as a filler and showed that the gain is an order of magnitude higher when substituting microsize ($\sim$ 10 µm) particles by nanosize particles ($\sim$ 10 nm) and the effect also depends strongly on the salt concentration as Marcinek et al.[66] observed. Part of the gain can be explained as an inhibition of crystallization of the polymer, but the effect on the ionic conductivity is still observed above the crystalline melting temperature [65] and many investigations have been initiated to improve the understanding of the mechanism behind the conductivity increase. As an example we show in figure 8.5 the effect of the nanoparticles on the fully amorphous polymer 3PEG at two different salt concentrations. From this figure one can see that the effect is dependent on the temperature, but also noticably on the salt concentration.

The salt:polymer and filler:electrolyte ratios at which the effect of the filler is most prominent is roughly 1 mol/kg and 10 wt%, respectively (depending on the chosen polymer, salt and nanoparticles). At these ratios the volumetric fraction of the filler is less than 3% and its influence on the conductivity should therefore be not restricted to the particle surface. Since the polymer electrolyte conductivity increases with the ionic diffusion rate, one could expect that an increase in the polymer dynamics would yield a higher ionic conductivity since the ions are coordinated to the polymer, typically via the ether oxygens of the polymer. However, it appears that the filler has little effect on the overall polymer dynamics as described by Karlsson et al. [67]. They estimated from their QENS experiments on the polymer dynamics of a fully amorphous polymer electrolyte a volume fraction of 5% of the polymer that is "immobilised" by the addition of the filler. The results by Karlsson are in correspondence

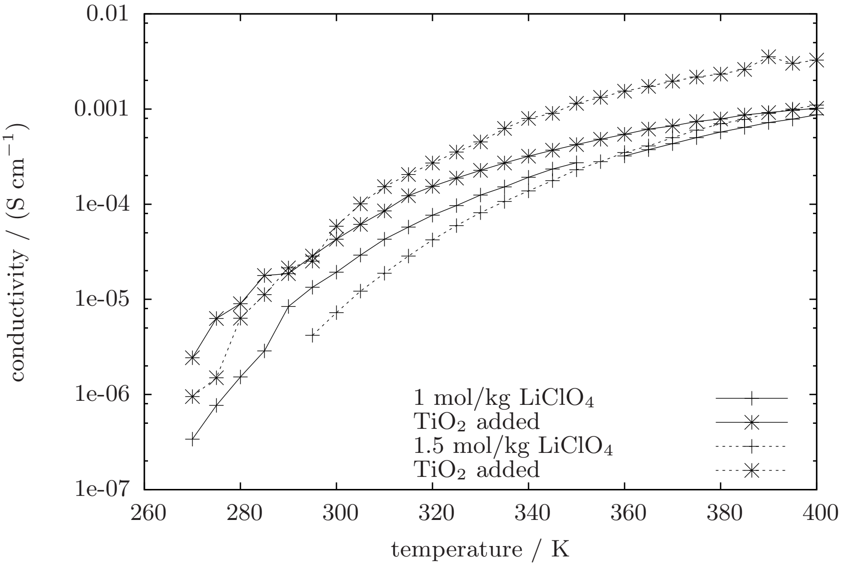

Figure 8.5: The conductivity in a fully amorphous polymer 3PEG (ethylene oxide and propylene oxide units in a 3:1 ratio) as a function of temperature (by kind permission of Dr. A.S. Best). Also shown is the effect of the addition of nanoparticulate TiO_2 at different concentrations of the salt $LiClO_4$.

with MD simulations by Kasemägi et al.[68] and Borodin et al.[69], who both simulated a polymer electrolyte and found reduced polymer dynamics near the surface of a nanoparticle. Raman investigations of the disordered longitudinal acoustic mode (DLAM) on PEO_8:$LiClO_4$ by Best et al.[70] show a slight stiffening of the polymer upon addition of the filler. The simulations tend to suggest that the nanoparticles do not provide a channel for rapid diffusion close to the interface as the ion concentration near the surface is lower than in the bulk, but the nanoparticles might reduce the mutual electrostatic interactions between the ions themselves, or their interaction with the polymer.

This tendency of the cation and anion to remain at least partly associated is referred to as "ion pairing" which is normally reduced by choosing large polarisable anions such as iodide, TFSI ($(CF_3SO_2)2N^-$) or perchlorate (ClO_4^-). For these anions ion pairing is extensively studied via Raman by Grodin et al.[71] and Edman [72] and via x-ray diffraction by Henderson et al.[73]. However Mao et al.[74] made an analysis of nearest neighbour distances via neutron scattering which strongly suggests that there is no time-average correlation between the lithium ion and the oxygen atoms of the anion for the LiTFSI salt dissolved in PEO. For the same salt a 6 fold coordination of the Li^+ by the oxygens of two diglyme molecules is suggested by Brouillette et al.[16], the diglyme molecules effectively shielding the cation. Yet in some cases, depending strongly on the sample preparation procedures and concentration ratios, the polymer does not suppress ion pairing.

In the next two chapters we describe our work on a model system of a polymer electrolyte. In the experimental work of Karlsson et al. [67] and Best et al. [70] the dynamics of the polymer were investigated and no clear effect of the nanoparticle was reported. In general these dynamics are governed by a complex of the local environment of the polymer segment combined with entanglements of the polymer chain with it self and neighbouring chains. Here we focus only on the local interactions of the cation and anion with the polymer and substitute the polymer with its oligomer diglyme (O-$[CH_2CH_2OCH_3]_2$), which enables us to perform DFT calculations on the whole molecule and a representative cluster of the model systems we study. Obviously the chain entanglement for such short sections of the polymer will be strongly reduced, and with that, its effect on the chain dynamics. Instead, one can expect the dynamics of diglyme to depend more on its local coordination *because* of the lack of entanglement.

A complementary INS/DFT analysis in chapter 9 yields the diglyme dynamics local to cation to which it is coordinated. We also find the local conformation of one diglyme with it coordinated cation. It turns out that the effect of the nanoparticle on the diglyme dynamics and conformation is negligible. From QENS experiments on the same model system we find again no effect of nanoparticle on the picosecond dynamics of diglyme.

The cation dynamics are probed using similar model system (see chapter 9) where the salt is substituted with ammoniumiodide and the diglyme is deuterated. Here the INS/DFT analysis shows that the environment of the cation softens upon addition of the nanoparticles and in our DFT calculation of the INS spectra, this trend is reproduced by reducing the charge on the model system. In our QENS data of chapter 10 no apparent broadening was observed due to the nanoparticle, but a significant increase in the quasi elastic signal triggered us to state a working hypothesis: the increased intensity in the QENS spectrum originates from cations that are immobile [§] when no nanoparticles are added. To test this hypothesis we compared our MD simulation with the librational INS spectrum and found indeed two distinct librational modes, from which we extrapolated the barriers for rotational diffusion. In agreement with our hypothesis, the highest of the two barriers would yield a characteristic time τ_2 for diffusion that is well out of range covered by the instrument. Further support for our hypothesis is found by comparison of the two librational peaks with and without the filler added: the intensities of observed librational peaks are redistributed in favour of the the slowest libration [†] upon addition of the nanoparticle.

[§] immobile within the dynamic range probed by the instrument

[†] the libration of which the rotational diffusion would be observed on the QENS instrument

Chapter 9

The effect of nanoparticles on ionic interactions

published in: *Macromolecules 37, 9591 (2004),*
L. van Eijck, A. S. Best and G. J. Kearley

Abstract

The increase in conductivity of polymer electrolytes on the addition of nanocrystalline materials has been investigated via the local dynamics of diglyme with two different salts; $LiCF_3SO_3$ and NH_4I. Local dynamics can be used as a diagnostic tool of changes to backbone conformations of the diglyme, and the dynamics of the NH_4 ion of the added salt, these being measured using inelastic neutron scattering (INS) and analysed with the assistance of Density Functional Theory (DFT) calculations. It is shown that the backbone conformation of the diglyme is little changed by the addition of salts, and/or TiO_2 nano-particles. The potential-energy landscape of the cation ($NH_4{}^+$) becomes smoother as interactions with the diglyme, and probably the anion, are reduced on the addition of nano-particles. Anion diglyme interactions seem to be weakened by TiO_2 and the cation remains coupled to diglyme.

9.1 Introduction

Polymer electrolytes, which are formed by dissolving ionic materials such as lithium iodide in polar polymers such as polyethylene-oxide (PEO), have practical advantages over liquid electrolytes in battery applications, but are limited by poor lithium-ion conductivity. Essentially, the polymer must ”solvate” the ions for them to dissolve, and this interaction constrains the back-bone dynamics of the polymer, which in turn reduces the diffusion of the ions [75]. Addition of nanocrystalline materials such as TiO_2 improves the ionic conductivity of the material by up to an order of magnitude, and despite considerable efforts, the reason for this improvement is still not clear despite having been studied by IR [66],Raman [70, 76], NMR [77] and ab initio [78]. It appears that the nano-particles have little effect on the overall polymer dynamics as described by Karlsson et al.[67], but it is not clear whether the nanoparticles provide a channel for rapid diffusion close to the interface or if they reduce the mutual electrostatic interactions between the ions themselves, or their interaction with the polymer [70]. This tendency of the cation and anion to remain at least partly associated is referred to as ”ion pairing” which is normally reduced by choosing large polarisable anions such as iodide, TFSI ($(CF_3SO_2)2N^-$) or perchlorate ($ClO_4{}^-$). For these anions ion pairing is extensively studied via Raman by Grodin et al. [71] and Edman [72] and via x-ray diffraction by Henderson [73]. However Mao et al. made an analysis of nearest neighbour distances via neutron scattering which strongly suggests that there is no time-average correlation between the lithium ion and the oxygen atoms of the anion for the LiTFSI salt dissolved in PEO [74]. For the same salt a 6 fold coordination of the Li^+ by the oxygens of two diglyme molecules is suggested by Brouillette et al. [16], the diglyme molecules effectively shielding the cation. Yet in some cases, depending strongly on the sample preparation procedures and concentration ratios, the polymer does not suppress ion pairing.

In the present work we assume that the nano-particles change the interactions between the ions and the polymer on a local scale since this enables us to simplify the system considerably by using short oligomers rather than polymers. In the present case we use diglyme, $(CH_3OCH_2CH_2)_2O$, as a convenient representation of PEO. By studying the vibrations of these oligomers with and without the nanocrystalline TiO_2 and comparing these results with ab-initio calculations we can probe any conformational changes in either the pure oligomer, or the oligomer with salt. Further, by making the approximation that an ammonium ion will substitute for lithium in these complexes, the vibrational and rotational dynamics of this ion will report on changes in the cation environment on the addition of nano-particles. This analysis is considerably simplified by using neutron scattering that reports almost entirely H-atom dynamics. By the use of selective deuteration we can study the cation and the oligomer independently. Vibrational spectroscopy can be one of the only methods to obtain structural information for the current systems. Inelastic Neutron Scattering (INS) spectra calculated using Density Functional Theory (DFT) methods have been validated a number of times and there is now a good understanding of the limitations of this method [33]. Within these limitations the method provides a robust, parameter-free method of obtaining good agreement between observed and calculated INS spectra. For systems of any complexity the structural information cannot be obtained directly from vibrational spectroscopy, but we are now in a position where we can adapt the conformation (or even contents) of a proposed model in an attempt to reproduce the main characteristics of the observed INS spectrum.

We note that the primary spectral region of interest in this study is $350-1000$ cm^{-1}. Above this region the data quality is poor. In the energy region below 350 cm^{-1} the intermolecular interactions come into play, which are difficult to incorporate in our models. Therefore we can only compare the observed spectra in this region. A previous study [79] has confirmed that the spectral region $350-1000$ cm^{-1} is significantly sensitive to conformational changes in our models.

In this paper we will present the effect of the salt and the TiO_2 nano-particles on the dynamics of both the diglyme molecule and the cation. We use a mixture of diglyme and $LiCF_3SO_3$ (LTD) to study the diglyme dynamics as this enables us to use, and even compare, known complexes from literature [80]. The effects of TiO_2 on the cation-dynamics in diglyme-salt mixtures are presented by substituting the salt with NH_4I and substituting the diglyme with deuterated diglyme. In this way we probe the dynamics of the system via the hydrogen displacements in the cation, NH_4^+. The DFT calculations of the vibrational spectra are computationally very demanding and we have therefore chosen a model for the NH_4^+ dynamics containing iodine instead of CF_3SO_3 as an anion, thereby reducing the number of normal modes to be calculated. It transpires that the backbone conformation of the oligomer is little changed by the addition of nano-particles, even though the oligomer-cation interaction is reduced [81]. These observations are consistent with a change in the charge distribution on the ions as a result of the TiO_2 surface that effectively reduced ion pairing.

9.2 Experimental

The diglyme sample was purchased from Aldrich, (anhydrous, 99+%) and used without further purification. Deuterated diglyme was obtained from Icon Isotopes Inc. with a quoted deuteration level of 98%. Nanocrystalline TiO_2 (anatase) with a particle-size of 40nm was obtained from Altair (dried for 2 days at 100°C). All handling of samples was made in nitrogen filled dry boxes). NH_4I or $Li(CF_3SO_3)$ (both obtained from Aldrich, 99+%, dried for one week at 60°C) was dissolved in the diglyme, and samples with nanocrystalline TiO_2 were prepared by mixing the TiO_2 into the electrolyte until a smooth paste was obtained. Such a consistency corresponds to approximately 66wt% TiO_2 in the composite. The sample was then spread in the flat aluminium can using a spatula, prior to being sealed and cooled to 20K using a closed-cycle helium cryostat. INS spectra were collected using the Tosca [55] at the ISIS spallation neutron source in the United Kingdom. The data were corrected and transformed to the energy-scale using standard algorithms.

9.3 Computational

All energy calculations were carried out using the Density Function Theory package DMol^3 [35] on a single "isolated" molecules, which allows an all electron calculation to be performed. Localized basis sets were used, represented as a numerical tabulation: a DND double numerical basis set with polarisation functions for carbon was used. A large number of energy calculations are necessary, and because we are not concerned with "wavenumber accuracy" in the present work, we restricted ourselves to the Local Density Approximation LDA (Perdew-Wang). The vibrational spectra were calculated in the harmonic approximation using the finite displacement technique to obtain the dynamical matrix. Starting from the energy-minimized models, each atom was displaced by ±.005Å in turn along the three Cartesian directions for which the total energy is recalculated. The total calculation when all atoms have been displaced gives the Hellmann-Feynman forces on all the atoms from which the force constants are obtained by dividing by the displacement. Positive and negative displacements were used in order to obtain accurate central finite differences. The force constant matrix **F** was transformed to mass-dependent coordinates by the **G** matrix giving the dynamical matrix. Diagonalization of the dynamical matrix gives the vibrational eigenvalues and eigenvectors. Our basic interest is in a correct assignment of the eigenvectors, which is easily made by comparison of observed and calculated INS intensities, so we make no effort to improve spectral agreement by scaling. The program Climax [32] was used to calculate the neutron spectral profile corresponding to the measured spectrum, from the normal modes above. The normal vibrational coordinates are mass-weighted, the scattering cross-sections of the different atoms are taken into account, overtone and combination frequencies are included, and recoil of molecules are incorporated by convoluting the calculated peaks with the measured phonon spectrum. Because the neutron scattering cross-section for H nucleus is about 20 times greater than for other nuclei, spectra are dominated by H-atom displacements. Deuteration thus essentially removes the contribution of the corresponding atoms from the INS spectra. However, deuteration does increase the mass of the normal modes and this indirect effect can be taken into account via the matrix **G**.

9.4 Results and Discussion

The oligomer: lithium triflate diglyme complex (LTD)

The crystal structure of the complex LTD ($LiCF_3SO_3 \cdot [CH_3OCH_2CH_2]_2O$) has been determined by x-ray diffraction [80] which provides a convenient starting model for analysis of the vibrational spectra of complexes containing less salt. We have recorded the INS spectra of LTD at 3 different salt concentrations corresponding to 10, 15 and 20 ether oxygens per lithium ion. We compare these spectra with those of pure diglyme in figure 9.1.

There are only slight differences between the spectra of the 3 mixtures of LTD in the region above 350 cm^{-1}, from which it follows that the presence of lithium ions even at the ratio of 1:20 (Li:EO) is sufficient to change the backbone conformation (compared to pure diglyme) in the whole sample. The region below 350 cm^{-1} will be discussed shortly. The crystallographic study [80] of LTD with 3 ether oxygens per lithium ion revealed the presence of 2 distinguishable dimers (labelled I and II), and in figure 9.2 we compare the calculated INS spectra for each of these with the experimental spectrum for the 10:1 compound.

Dimer II is in rather better agreement with the experimental spectrum, and it seems that at these lower salt concentrations this is the preferred local structure. We note that the calculated total energy of the isolated dimer II was lower than that of dimer I by 2.19 kcal/mol. For completion we include the observed and calculated spectra for pure diglyme in figure 9.2 and collect the different molecular geometries in Table 1 so that the way in which the local structures affect the INS spectrum can be gauged. This initial part of the study establishes the link between INS spectra in the 350 to 1000 cm^{-1} region and the backbone conformation of the diglyme, and also the ability of DFT calculations to provide a reasonable analytical tool for local structure, even within the isolated-molecule approximation. Our interest is now to look more closely at the interactions between the various species. Since structural data and DFT calculations are available for the dimer II, we can proceed to make a topological analysis of the calculated electron density between the ions and molecular fragments of the dimer II. We have made this analysis based on the ideas of Bader [15] using the program Fast [39] to determine the critical points in the electron density of the

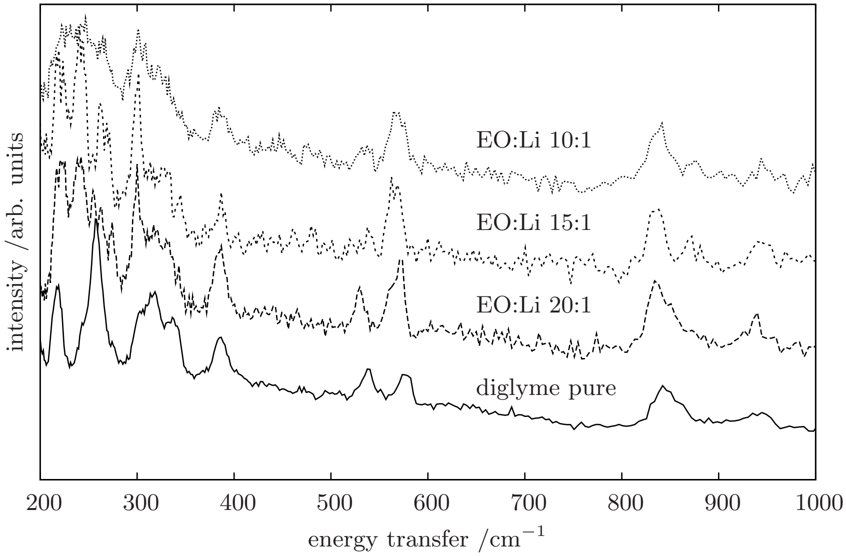

Figure 9.1: Comparison of the observed INS spectra for pure diglyme and mixtures with lithium triflate at various ether-oxygen:Li ratios. The spectral region above 350 cm^{-1} is sensitive to conformational changes of the diglyme molecule where only slight changes are observed. Below 350 cm^{-1}, the low salt concentration samples (20:1) shows sharp features, that disappear at high concentrations (10:1).

electrolyte and the bond-paths linking these. The results of this analysis, shown in figure 9.3, clearly show not only the expected intramolecular bonds-paths and bond-paths from the lithium to the ether oxygens, but also paths between the ions, and even from the F atom of the anion to the H atoms of the diglyme.
Large singly charged anions are usually regarded as globular and weakly interacting due to the delocalisation of the single charge over a large molecular surface. The interactions shown here are rather more directional than this simple picture might suggest showing very clear ion-pairing as well as interactions between each ion and

Table 9.1: Distances in the different models used; between the outer oxygen atoms (Oo) of the diglyme molecule and distances from the cation center to the center- and outer- oxygens (Oc,Oo respectively.) in Ångstroms. All diglyme molecules are in a tgt-tg't conformation.

Model	Oo - Oo /Å	Cation-Oc /Å	Cation-Oo /Å	
LiTf-diglyme dimer(I)	4.094	2.044	2.166	2.113
LiTf-diglyme dimer(II)	3.980	2.075	2.105	2.105
{NH$_4$ diglyme}$^+$	4.567	2.867	2.655	2.664
{NH$_4$ diglyme}^{0}	4.783	3.052	2.862	2.848
diglyme pure	4.993	-	-	-

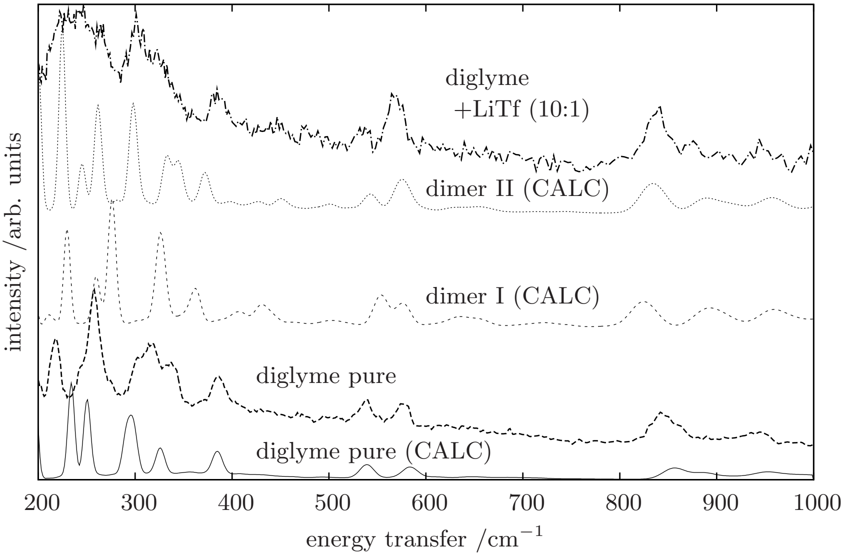

Figure 9.2: Comparison between observed and calculated INS spectra. For pure diglyme the calculated optimal conformation shows good spectral agreement with the observed. The two dimers with Li (I and II) are calculated from the XRD-derived structures. These structures differ only slightly, yet the spectral consequences are observable.

the diglyme. These interactions play a role in the vibrations of the diglyme molecule. Comparing the various spectra below 350 cm^{-1} in figure 9.1, we observe that the peaks in spectra of the most diluted mixture loose sharpness when the salt concentration is increased. It is difficult to conclude how the sharpness is lost, however from our vibrational calculation of dimer II we do know that these peaks arise from CH_2 and methyl rocking modes. For those CH_2 and methyl groups we have found a bond-path to the anion as seen in figure 9.3. This strongly suggests that the increase in salt concentration hinders the vibrations in this low energy region via anion-diglyme interactions, where the F atom on the anion has a bond-path to three H atoms on the diglyme molecule. The Li^+, being bonded to oxygens of diglyme, is unlikely to have an effect on this type of vibrations.

The effect of nanocrystalline TiO_2 on LTD The measured INS spectra of pure diglyme and LTD with and without TiO_2 nanoparticles are shown in figure 9.4. Above 350 cm^{-1} there are virtually no spectral differences between the samples with and without the nano-particles indicating that either there are no changes on the backbone conformation, or that by chance, the changes have no spectral consequences. Our previous work [79] would suggest that the latter is unlikely. In figure 9.4, below 350 cm^{-1} we compare the effect of TiO_2 on pure diglyme and the 10:1 LTD mixture. Only small changes are observed for pure diglyme, where as the addition of TiO_2 to the LTD mixture causes a significant sharpening of the peaks. The comparison of the different concentrations of figure 9.1, discussed above, led us to conclude that the reduced sharpness of the peaks in this region below 350 cm^{-1} is due to diglyme-

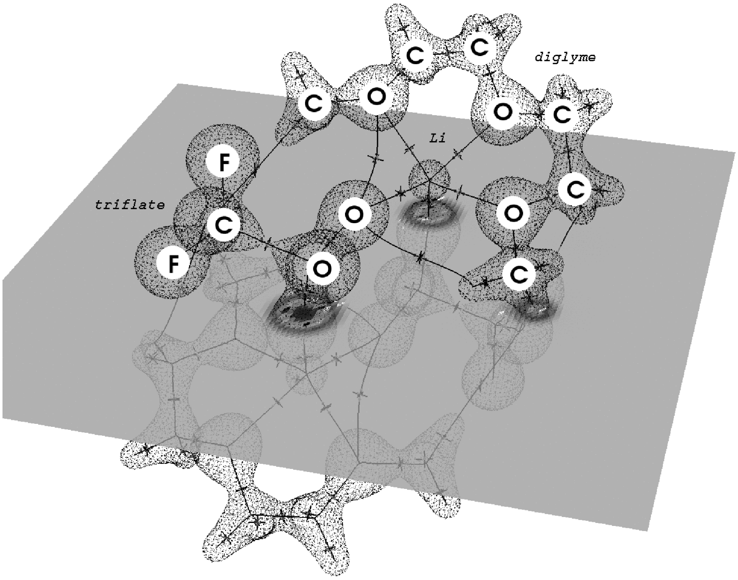

Figure 9.3: Iso-density surfaces and calculated bond-paths of dimer II. The semitransparent square surface is shown for clarity: it cuts the dimer in two and is centered at the symmetry inversion point of the dimer. In addition to the intramolecular bond-paths, there are 3 paths between the Li^+ and diglyme oxygens: 1 between each triflate (CF_3SO_3) oxygen and the Li^+, and 3 between a triflate fluorine atom and the CH_3- and CH_2-end group hydrogen of diglyme. We also find 2 weak bonds from the triflate oxygen to the outer diglyme oxygen and the opposite methyl hydrogen.

CF_3SO_3 interactions and that the addition of TiO_2 recovers this spectral definition. These combined observations in figure 9.1 and figure 9.4 (below 350 cm^{-1}) suggest that the diglyme-anion interaction is reduced by the addition of TiO_2.

The cation: ammonium iodide diglyme complex (AID)

Ideally, we would like to determine the effect of the nano-particles on the environment of the Li^+, but this is experimentally rather challenging. In order to overcome these problems, we have used the ammonium as a cation in place of the lithium because its dynamics are easily studied by neutron scattering. Further, by using deuterated diglyme, $(CD_3OCD_2CD_2)_2O$, we are able to follow the dynamics of the ammonium hydrogen atoms directly as the scattering from diglyme molecules is essentially eliminated. The spectra of the ammonium iodide in deuterated diglyme, with and without the nanoparticles, are compared in figure 9.5. In the spectral region of figure 9.5 pure NH rocking curves would show around 700−900 cm^{-1}. We observe ammonium rocking modes at lower energies suggesting that, as expected, the ammonium-ion vibrations are coupled to those of the diglyme molecule. In order to understand this in more detail we require a model for the $(CD_3OCD_2CD_2)_2O \cdot NH_4^+$ species since there are no crystallographic data available for the AID mixture. We have taken the known

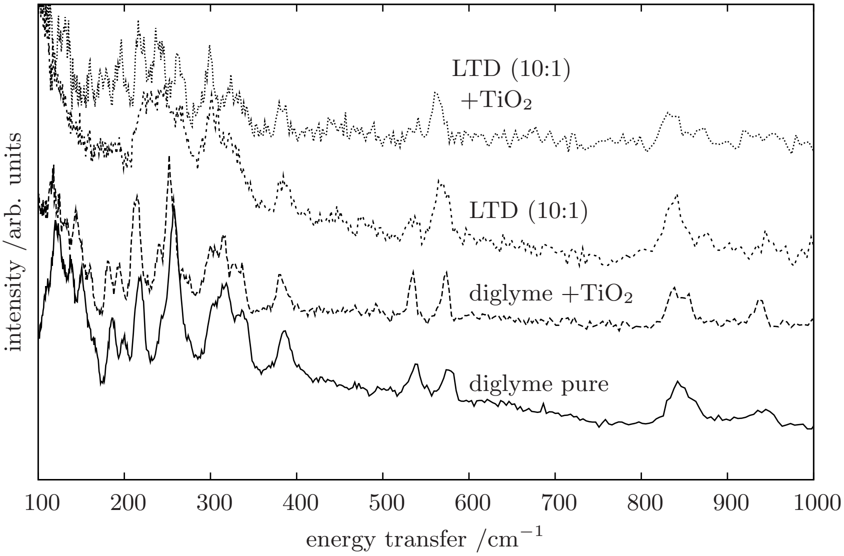

Figure 9.4: The influence of TiO_2 nano-particles on diglyme. The observed INS spectra show that the diglyme dynamics are only slightly changed on the addition of the nanoparticles, where as the diglyme-salt mixture LTD shows a sharpening of peaks below 350 cm^{-1} on addition of TiO_2.

molecular fragment of a Li^+ with a single diglyme molecule, and replaced the Li^+ with NH_4^+. This structure was minimised with respect to total energy, the final geometry being given in table 9.1. The diglyme molecule has the same tg$^+$t-tg-t conformation as dimer II measured by Rhodes [80]. The INS vibrational spectrum of this selectively deuterated model was calculated, and is compared with the measured spectrum in figure 9.5. When we include in our calculation the deuteration of the diglyme molecule, it causes a downward shift in the calculated NH_4^+ peaks, which clearly shows the coupling in the dynamics of NH_4^+ and diglyme. Although the quality of the experimental data is somewhat limited, there is quite reasonable agreement between observed and calculated spectra.

The effect of nanocrystalline TiO_2 on AID

Our final molecular model for $([CD_3OCD_2CD_2]_2O \cdot NH_4)^+$ is energetically reasonable and reproduces the measured vibrational dynamics so we would now like to change this model in order to understand the spectral changes that arise on addition of TiO_2 nanoparticles. There are too many unknowns to produce a model including the anion and the TiO_2 particle, and further the spectral quality is poor. Nevertheless, we have deduced a simple but realistic model based on the available experimental observations. Firstly, we have shown that the INS spectrum of LTD with and without nano-particles are virtually indistinguishable in the 350 to 1000 cm^{-1} region, suggesting that the basic backbone conformation of the diglyme is unchanged on the addition

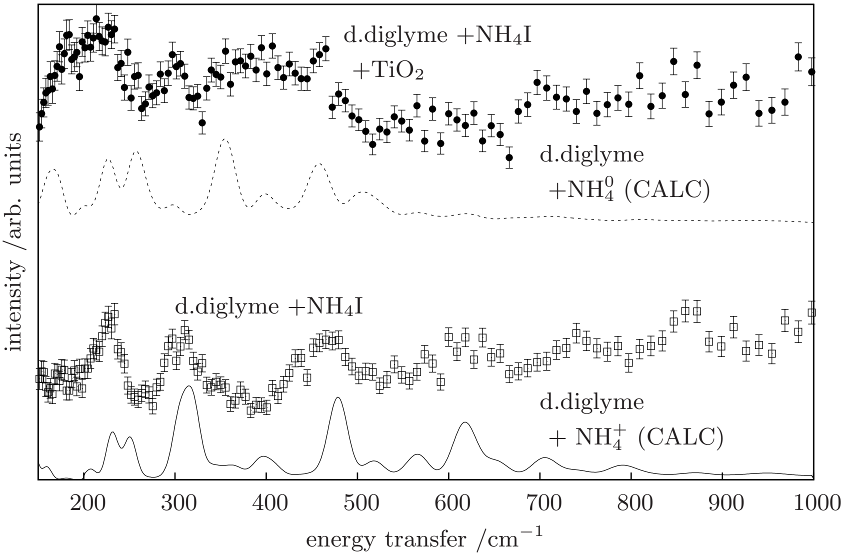

Figure 9.5: Observed and calculated INS spectra for the deuterated diglyme (d.diglyme) ammonium iodide complexes. The calculation from the diglyme-NH_4^+ model incorporates the frequency-shift due to deuteration of the diglyme molecule. When the positive charge is removed from the model, the peaks shift to lower frequencies.

of TiO_2. Secondly, the ionic conductivity increases on addition of TiO_2 nanoparticles [66], from which we can propose that the cations become less strongly held in their local environments. Finally, the INS spectrum of $(CD_3OCD_2CD_2)_2O \cdot NH_4^+$ is that of the ammonium ion coupled to the backbone modes of the diglyme, and these do not change significantly on addition of nano-particles. By these arguments we suggest that the ammonium ion is still surrounded by the diglyme molecule in a tg^+t-tg-t conformation when the TiO_2 nano-particles are added. The general trend shown in figure 9.5 is a shift of spectral intensity to lower frequencies, suggesting that the ammonium-ion experiences a more smooth potential-energy environment. This is probably due to changes in Coulomb interactions and a simple means of reducing these is to take a ”mean-field” approach by altering the formal charge on the model from +1 to 0. The geometry of this model was optimized, the results being given in table 9.1, and the INS vibrational spectrum was calculated, this being compared with the experimental spectrum of $(CD_3OCD_2CD_2)_2O \cdot NH_4I$ in figure 9.5. The agreement is far from perfect, but nevertheless, this simple approach is consistent with the backbone conformation, increased mobility of the cation, and with the general shift of spectral intensity to lower energies. The picture that emerges is of ions that are solvated by the diglyme molecules where Coulombic interactions play an important part, but van der Waals interactions are also involved in the details of the packing. The overall backbone conformation of the diglyme is changed by the addition of salt, but little by the nano-particles. However, the latter clearly modify the dynamics of the cations as seen in figure 9.5. The evidence presented here supports the idea that the surface of the nano-particles modify the mean Coulombic field of the cation, and probably also the anion, leading to a smoother potential-energy landscape and thus increased mobility. This may well arise from space-charges that exist at the surface of the nano-particles.

9.5 Conclusions

The essential message contained in the data is that the vibrational spectrum in the 350 to 1000 cm^{-1} region is largely determined by the backbone configuration of the diglyme species, $(\mathrm{CH_3OCH_2CH_2})_2\mathrm{O}$. It turns out that this conformation is similar both in the pure material, with salt, with nano-particles, or with both. The U-shape of this conformation tightens on addition of salt (see table 9.1) and for the $\mathrm{CF_3SO_3^-}$ anion there are a number of bonding interactions with both the $\mathrm{Li^+}$ ion and the diglyme molecule, and the vibrational consequences of these being seen in both the observed and calculated INS spectra. These effects are strong, and even samples with an ether-oxygen to $\mathrm{Li^+}$ ratio of 15:1 still show the spectral characteristics of LTD rather than a mixture of LTD and pure diglyme. This is probably a templating effect rather then the direct effect of one ion over such a long range. The spectra below 350 cm^{-1} show the soft rocking modes of the diglyme molecule that seem to be affected by the anion-diglyme interactions, which we find as bond-paths in the calculated electron density. The spectral changes of these modes with salt concentration strengthens this hypothesis. The effect of the $\mathrm{TiO_2}$ nano-particles is very difficult to model because little is known of which crystal planes are involved, or even how the surface is terminated. Defects and space-charges will also clearly play an important role, but modeling these is well beyond the scope of the present paper. From a previous study [79] we know that the soft rocking modes of pure diglyme are not significantly influenced by the addition of $\mathrm{TiO_2}$ compared to the effect the $\mathrm{TiO_2}$ has on the LTD mixture in this spectral region. According to our electron-density bond-paths the anion is directly connected to the H atoms that participate in these rocking modes. The $\mathrm{TiO_2}$ nano-particles thus seem to remove the anion-diglyme interactions. We therefore suggest that the effect of $\mathrm{TiO_2}$ on the cation is indirect and thus difficult to model, but a more general explanation in terms of space-charge is appropriate. The potential-energy surface for diffusion of the ions is the sum of the various Van der Waals and Coulomb terms. It is unlikely that the former is affected by the nano-particles so any increase in ion mobility will be through a smoothing of the Coulomb potential-energy surface of the cation.

Acknowledgements

We are grateful to FOM for financial support (in the TFF program 97TF18) of L.v.E., to A.J. Ramirez-Cuestra from ISIS RAL (UK) for help and advice with the neutron scattering experiments, and to NWO for financing the experiment at ISIS.

Chapter 10

Softening of the potential-energy surface on the addition of nanoparticles

published in: *Chem. Phys. 317, 282 (2005),*
L. van Eijck, A. S. Best, J. Stride and G. J. Kearley

Abstract

The conductivity of polymer electrolytes is enhanced by an order of magnitude or more upon addition of a few weight percent nanoparticulate TiO_2, but the mechanism by which the conductivity increase occurs is still under debate. Considerable effort has been put in understanding the influence of this TiO_2 filler on the dynamics of the polymer, but in this work we focus solely on the local cation dynamics. We use a model system that consists of NH_4I dissolved in a deuterated oligomer of PEO, so that we can use inelastic and quasielastic neutron scattering to study the rotational dynamics of the $NH_4{}^+$ ion, without the complicated signal from the oligomer. Analysis of the local rotational potential of the $NH_4{}^+$ ion by comparison of the experimental data with the H-atom trajectories from a molecular dynamics simulation, reveals an overall reduction of the interaction between the $NH_4{}^+$ ion and the ether-oxygens of the diglyme. Although the extension to cation diffusion in PEO cannot be made directly, our results are entirely consistent with the observed increase in conductivity on addition of nanoparticles. The experimental neutron-scattering data and the molecular dynamics simulation are all consistent with the presence of groups of 2 basic environments for $NH_4{}^+$ ions, at least in the diglyme system. On a timescale of about 10ps these environments are visited by all $NH_4{}^+$ ions, and the addition of nanoparticles softens the more hindered environments making the two groups more similar to each other.

Our results strongly suggest that the observed increase in conductivity of polymer electrolytes on addition of nanoparticles is due to a reduction of the interaction between ether-oxygens and the cations, rather than an increase in the polymer dynamics.

10.1 Introduction

The increase in conductivity of polymer electrolytes upon addition of nanocrystalline TiO_2 as a filler is still poorly understood, despite the considerable body of research on this effect that has been performed over the past few years. In the present article we will use the term filler to denote nanocrystalline materials that are used in this way. Lithium salts dissolved in the polymer polyethyleneoxide (PEO, $[C_2H_4O]_n$) are frequently used as model systems for polymer electrolytes, in which Li^+ is the mobile cation, and a large polarisable molecular species, such as triflate (CF_3SO_3) or TFSI ($[CF_3SO_2]N^-$), is chosen as the anion. The ether oxygens of the polymer coordinate the Li^+ (typically 5-fold) [74] and the various dynamics of the polymer chain modulate the Li^+ coordination assisting cation mobility. Upon addition of nanoparticulate TiO_2 (typically 5−8 wt%) to the polymer electrolyte the conductivity is increased by an order of magnitude or more, for which several mechanisms have been suggested, such as inhibition of crystallisation of PEO [2], increase in free volume in the polymer electrolyte [76] and introduction of charge carrier pathways near the nanoparticle surface [76, 82, 83], possibly via interactions with Lewis acid or base type centers of the filler material. However, none of the models are able to explain the increase in conductivity unambiguously. An increase in conductivity due to the filler has also been observed for a fully amorphous system [82, 83] and Karlsson et al. have suggested from their QENS experiments [67] that an immobile layer of polymer chains forms at the surface of the filler. This suggestion was supported by the MD simulations of Kasemägi et al. [68] and more recently by Borodin et al. [69]. However, the mechanism behind the increase of conductivity by charge carrier pathways is unclear from these simulations because if the polymer at the surface-layer were immobilised, charge-carrier pathways would actually be reduced at the filler surface, leading to a reduction, rather than an increase, in conductivity. In order to improve our understanding of the effect of the nanoparticles on the conductivity of polymer electrolytes we have chosen to study the picosecond dynamics of the cation directly via quasi-elastic neutron scattering (QENS). This technique however, derives its strength from its sensitivity to motion of hydrogen atoms so in the current work we use the pseudo alkali-metal ion $NH_4{}^+$ in place of the more usual Li^+ ion. In order to study the system at a fundamental level we use an oligomer of PEO:diglyme (rather than PEO itself), which can be conveniently deuterated, ($C_6O_3D_{14}$), making the molecule practically invisible in the QENS signal so that we see only the motion of the ammonium cation. Whilst translational diffusion of the cation is important for conductivity in PEO, in the present work we are concerned with the interaction of the cation with the ether oxygens and the anions that may be modified by the presence of the filler. To this end we focus on the localised rotational dynamics of the cation at a convenient temperature (200 K) for the QENS experiments. The rotational dynamics of $NH_4{}^+$ is particularly sensitive to its local environment and both the rotational vibrations and rotational diffusion from MD simulations can be compared with experiments, within the limits of available structural information. The choice of an oligomer also enables us to compare the QENS results with previous inelastic neutron scattering (INS) experiments and *ab initio* calculations [84]. We choose the salt NH_4I because the iodide ion is large and polarisable as required, yet much simpler to model than the molecular ions normally used in polymer electrolytes. The system

under investigation can be formulated as: $(C_6O_3D_{14})_8 \cdot (NH_4I)_3$.
In a previous work [84] we focused on the vibrational dynamics of both the diglyme and the cation separately. By combining *ab initio* calculations with INS spectra, we were able to assign a minimum energy conformation of the diglyme+cation cluster to the observed spectra. The calculations revealed that the vibrational spectra of the $(C_6O_3H_{14})$ moiety in the 200 to 600 cm^{-1} region are rather sensitive to changes in the backbone conformation of the diglyme and charge-distribution of the model. From this we were able to conclude that the backbone conformation of diglyme is almost independent of salt concentrations, and that one diglyme folds around the cation as shown in figure 10.1. In that work we also showed that diglyme also maintains much the same conformation upon addition of nanoparticles. The vibrational dynamics of an ammonium cation were reproduced using this minimum energy conformation of 1 diglyme and 1 cation (figure 10.1), which was also able to reproduce the spectral trends observed for the cation dynamics upon addition of the filler. From these conclusions we proposed that addition of the filler smoothes the potential-energy landscape of the cation, especially with regard to Coulomb interactions. The same model system, $(C_6O_3D_{14})_8 \cdot (NH_4I)_3$, is used in the current work, but here we asses changes to interactions of the cation with the ether oxygens and the anion by comparing the measured QENS spectra, with and without the filler, with the results of molecular dynamics simulations (MD). For consistency we also compare the librational motions of the $NH_4{}^+$ ion from the MD simulation with our previous INS vibrational spectra. Because many properties of the nanoparticles are unknown (surface structure, termination and roughness) we make no attempt to include these particles in the MD simulation. Our aim is to use the MD simulations to understand the $NH_4{}^+$ dynamics in deuterated diglyme so that we can then have some idea of the dynamics that give rise to the observed changes in the QENS signal when the filler is added. The angular velocity autocorrelation function (VACF) of the $NH_4{}^+$ ions in the simulation reveals heterogeneous dynamics in which the rotational-barrier of a given $NH_4{}^+$ ion evolves

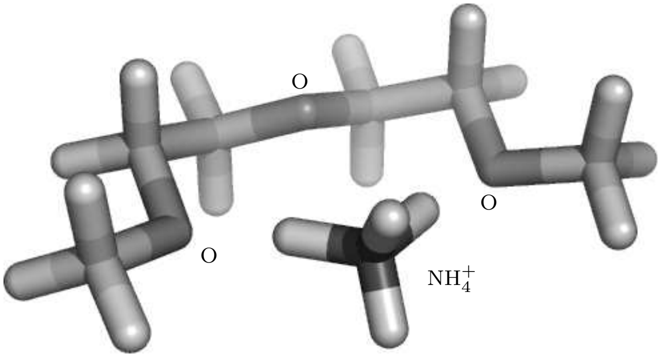

Figure 10.1: One deuterated diglyme surrounding an NH_4^+ ion. This model describes vibrational dynamics satisfactory and was used in the current work as input to build an amorphous cell for MD simulations.

with time. This behavior is common to many glassy and amorphous systems. The most striking change in the QENS spectrum on the addition of the filler is an increase in quasielastic intensity, with rather little change in the width. Our MD simulations support the idea that this intensity increase arises from a regrouping of dispersion in the dynamics. Groups that fall within the resolution function in the pure electrolyte become comparable with those that fall outside the resolution function when the filler is added. Essentially, addition of the filler generates more NH_4^+ ions with similar relaxational dynamics.

10.2 Methodology and Experiments

Because of the rather surprising observations (above) QENS measurements were made at two different instruments: the time-of-flight spectrometer IN5 at ILL, France, and the backscattering spectrometer Iris at Isis, United Kingdom that can access higher momentum transfers. The instruments were used with a similar resolution function (FWHM=17 μeV), the pyrolytic graphite 002 reflection being used on Iris in conjunction with a beryllium filter, and on IN5 an incident neutron wavelength of 10 Å was selected. For Iris this provided an energy and momentum transfer range of $0.6 < E < 6.6$ meV and $0.3 < Q < 1.8\text{Å}^{-1}$, whilst for IN5 the corresponding ranges were $150 < E < 0.4$ meV and $0.26 < Q < 1\text{Å}^{-1}$ respectively. Samples were packed in standard aluminium containers, and temperature control was achieved using standard cryostats.

The deuterated diglyme was purchased from Icon Isotope Inc (deuteration 98+%) and the TiO_2 anatase nanoparticles (diameter 40 nm) from Altair (dried 24h). All samples were used without further purification and mixtures were prepared under dry nitrogen conditions. The NH_4I (Aldrich, 99+%) was dissolved in diglyme to an ether-oxygen:ammonium ratio of 8:1 and TiO_2 nanoparticles (approx. 60 wt%) were added to form a smooth paste at room temperature. All samples were sealed airtight in the sample cans.

Raw data were converted to $S(Q, \omega)$ using the correction software provided for these instruments by Isis and ILL. A vanadium slab was used to correct for detector efficiencies and to provide a numerical definition of the resolution functions, and an empty container was measured to correct for background scattering. Corrections were also made for self-shielding. Least-squares fitting procedures for the analysis were written locally for the analysis of the observed profiles in terms of a stretched exponential [85, 86] and a boson peak [87]. In order to improve the counting statistics spectra were grouped to eight Q-values before analysis. In the present work we only fit the boson peak so that it can be extracted from the QENS signal and do not discuss its origin or behavior.

MD simulations were made using the Tinker package version 4.2 written by J.W. Ponder [47]. The van der Waals interactions are described by the Buckingham potential and the MM3/2000 [47] force-field was used with some modifications: atomic charges of the ammonium and diglyme molecule were adapted using the Hirschfeld charge partitioning of *ab initio* calculations of our previous work [84] but with the simplification of averaging the charge per force-field type and maintaining the overall charge neutrality of the model (see table 10.1).

Since the structure of the electrolyte of our experiments is not known, with or without the nanofiller, we built an amorphous cell of diglyme and NH_4I with a density of 1.4 g/cm^3 (as in the experiments) and an EO:ammonium ratio of 9:1 which corresponds reasonably with the experimental ratio of 8:1 (due to the stoichiometry of three ether oxygens per diglyme and the limited number of molecules in the model). The AMORPHOUS CELL utility of Accelrys [50] was used to build a cubic amorphous cell (18.654 Å) containing 10 cations and anions, and 30 diglyme molecules. To adapt the cell to the force-field parameters used in the molecular dynamics simulation, the cell was annealed using these parameters in 2000 steps of 1 fs from 1000 K to 200 K to ensure that the thermodynamic equilibrium state was obtained in the simulations. These simulations were done at 200 K, (NVT ensemble) for 200 ps (1 fs timestep) using the Beeman algorithm in TINKER with a cutoff for non-bonded interactions of 9 Å and using Ewald summation for Coulombic interactions (smooth PME, Ewald coefficient 0.42, charge grid 30 × 30 × 30, B-spline order 8). The analysis of the trajectories to obtain angular velocity autocorrelation functions of the ${NH_4}^+$ ions and $S(Q, \omega)$ were made using the nMOLDYN package written by Kneller et al.[88].

10.3 Experimental results

In QENS spectrum the observed broadening is proportional the Fourier transform of the van Hove time-autocorrelation function of the dynamics that are being probed. In the present case the ${NH_4}^+$ ion dynamics are probed since the diglyme molecule is deuterated. The width of the quasielastic broadening is inversely proportional to the characteristic time of these dynamics [89]. We have measured the quasi-elastic broadening at 150, 175, and 200 K with and without nanoparticles, and it turns out that these spectra can be fitted satisfactorily using the sum of a Bergman function [86], which is a good approximation to the Fourier transform of a stretched exponential or Kohlrausch-Williams-Watts (KWW) function [85], and a boson peak [87]. The result was then convoluted with the measured resolution function. The whole function fitted

Table 10.1: Charges per atom type in the MM3/2000 force-field as used in the simulations. The charge partitioning is based on a Hirschfeld analysis of *ab initio* calculations of our previous work [84]. The overal charge of the model containing 3 diglyme molecules per cation is 0.002 $|q_{\mathrm{electron}}|$.

MM3/2000 FF type	charge (in $|q_{\mathrm{electron}}|$)
(diglyme) ether oxygen	-0.10
(diglyme) carbon	0.0
(diglyme) hydrogen	0.0319
(anion) iodine	-1.0
(cation) nitrogen	0.0
(cation) hydrogen	0.14

to the data was:

$$S(\mathbf{Q},\omega) = R(\mathbf{Q},\omega)\otimes \\ \left(\frac{1}{\omega}\frac{X''_{SE}}{1-b+\frac{b}{1+b}\left(b\frac{\omega_{SE}}{\omega}+\left(\frac{\omega}{\omega_{SE}}\right)^{b}\right)} + \frac{\exp\left(-\frac{\log|\omega|-\log|\omega_{BP}|}{2\sigma^2}\right)}{\sqrt{2\pi\sigma^2}} + \delta_{EP} \right), \quad (10.1)$$

where X''_{SE} is the coefficient of the imaginary part of the susceptibility, ω_{SE} is the position of the maximum susceptibility and b is related to the stretching parameter, β, of the KWW-equation (see ref [86]). The boson peak was fitted via its position ω_{BP} and its width,σ, and together with the elastic peak intensity, δ_{EP} these functions were convoluted with a numerical description of the resolution function $R(\mathbf{Q},\omega)$, that was obtained for each detector-angle from the vanadium run. The resulting parameter values are collected in table 10.2.

Table 10.2: Parameters of the functions fitted to the QENS data with and without TiO_2 nanoparticles at 3 temperatures. A stretched exponential (SE) function and boson peak (boson) function were sufficient to fit all the observed QENS spectra of the cation. As the fitting is done in the frequency domain, the stretched exponential is approximated by the Bergman function and the resulting parameters are transformed to stretched exponential parameters as described in [86].

			NH_4I-d.dg			NH_4I-d.dg+TiO_2		
	Temperature	/K	150	175	200	150	175	200
SE	intensity	/arb.units	0.25	0.25	0.30	0.35	0.45	0.65
	τ_{avg}	/ps	66	52	40	56	54	53
	β		0.70	0.70	0.65	0.60	0.55	0.50
boson	intensity	/arb.units	0.12	0.14	0.15	0.2	0.2	0.2
	width	/meV	1.2	1.2	1.2	1.1	1.15	1.2
	position	/meV	2.1	2.1	2.1	1.9	1.9	1.9

10.4 Discussion

The empirical functions used to fit the boson and quasielastic scattering are characteristic for glassy systems, and their presence here reflects the presence of a glassy state. This type of relaxation behavior is often found in polymers and many other glassy and amorphous systems, and is even observed for water in some environments [90]. The stretched exponential function, $\exp(-(t/\tau)^{\beta})$, can be interpreted as a generalized description of the dynamics of a relaxational process in which a certain spread in the relaxation time τ is introduced by the shape parameter β. Colmenero et al. [91] have suggested that this phenomenological function can originate from different physical scenarios and concludes that for glass-forming polymers the relaxational dynamics are caused by a homogeneous sub-linear diffusion process, which in our system should result in anomalous relaxation for each cation that contributes to the observed dynamics. There is no reason that this type of dynamics should be restricted to polymers, and indeed, our simulations show dynamics, for each NH_4^+ ion, that are intrinsically non-exponential. We do not attempt to impose a description of processes from our fits of the shape parameter and only mention here that addition of the filler reduces β from about 0.70 to 0.55, which implies that the addition of filler leads to a further extension in the range of relaxation pathways. Further discussion of this aspect of the dynamics goes beyond the objectives of the current paper. Inspection of table 10.1 reveals that both the characteristic time and the QENS peak intensity increase with temperature. The most important observation is that at all temperatures, the addition of the filler has only a slight effect on the characteristic time τ of the NH_4^+ dynamics, but the intensity of the quasi-elastic scattering increases significantly.

These observations would indicate that the addition of nanocrystalline TiO_2 particles increases the population of those NH_4^+ ions that have the specific dynamics characterized by the quasielastic broadening within the spectral window of the current experiment. Before proceeding to the MD simulation we will first give a brief overview of published work on the effect of fillers in polymer electrolytes. Karlsson et al. [67] made QENS measurement on the polymer (not the cation) from which they suggested that an immobile layer of polymer forms around the filler particle. This hypothesis is supported by MD simulations performed by Kasemägi et al. [68] and also simulations of Borodin et al. [69] for the PEO/$LiBF_4$/nanoparticle system. From these simulations they also find a lower concentration of ions close to the stationary layer than in the bulk polymer electrolyte. The following layer however, has an increased ion concentration. Whilst there seems to be general agreement about the stationary layer of polymer at the particle surface, there is some contradiction between these groups concerning the effect of the nanoparticle on the ion dynamics, and no clear picture emerges. This is one of the main incentives for the current work in which we use an MD simulation to gain some insight into the underlying interactions of the cation, in this case NH_4^+.

In figure 10.2 we show a comparison of the observed QENS and that derived from the MD simulation for $Q = 1.0\text{Å}^{-1}$ at 200 K. In order to simplify comparison of the observed and calculated quasielastic signal, we have subtracted the fitted boson peak from the observed data. The agreement between the resulting quasi-elastic broadening and simulation is quite satisfactory at this temperature and Q value, but we find that the temperature and Q-dependence of our simulated spectra do not agree well with those observed.

Despite the use of different force-fields and treatments of Coulomb interactions we were unable to improve the agreement with the temperature and Q-dependence. It should be remembered that there are no structural data and that we have based our model on an amorphous construction. This model for a glassy system is of course only one of a vast number that are present in the real system and we have no straightforward way of ensuring that it is representative of the average without building a large number of different amorphous cells. Nevertheless, our interest in the MD simulation is to determine whether the NH_4^+ dynamics fall into groups, even for a restricted amorphous model, and if so, could changes in the grouping account for the observed increase in quasielastic intensity on the addition of filler? We would anticipate that even the limited model contains significantly more NH_4^+ ions than groups of these

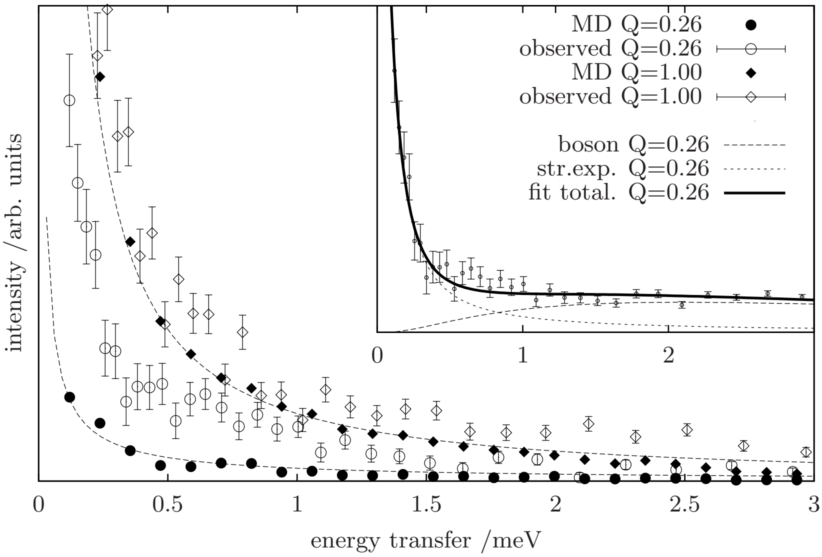

Figure 10.2: Observed and calculated QENS spectra for two Q values measured. Main plot: the observed spectra are plotted with error bars and the boson peak contribution is subtracted; simulated data is plotted with filled symbols and a dashed line as guide to the eye. The simulation at $Q = 0.26\text{Å}^{-1}$ has significantly less quasi elastic broadening than the observed spectrum, but the simulation at $Q = 1.0\text{Å}^{-1}$ corresponds reasonably well with the observed broadening at that Q value. The inset shows how the fitted function for $Q = 0.26\text{Å}^{-1}$ is generated from its components: a boson peak and a stretched exponential.

in the resulting dynamics. Potential energy contributions in the trajectories were dominated by an attractive charge-charge interaction and a repulsive Buckingham exponential-6-term, making the dynamics probed by QENS nearly temperature independent.

10.5 Rotational dynamics

Inspection of the animated trajectories revealed that the cation typically coordinates to one or two ether oxygens or an iodine ion. Within the time frame of the simulation (200 ps) the cation undergoes limited translation within its surroundings and rotates continuously, thereby modifying its coordination with its environment. Although both the translational and rotational dynamics are important, at present we wish to separate the rotational part in order to characterize different environments and to compare with our previous vibrational study [84]. The angular VACF was extracted from the trajectories for each individual cation, convoluted with a Gaussian resolution function and Fourier transformed to obtain the power spectrum of the angular frequencies.

Trajectories from different starting structures were analysed, and a typical example of an angular VACF spectrum is illustrated in figure 10.3. It contains rotation-librational peaks of the NH_4^+ ion in its local potential energy landscape and can be compared with the low-energy part of the vibrational spectrum of the cation. In our previous work [84] we discussed this observed INS spectrum, which compared rather well with the vibrational spectrum calculated by em ab-initio methods using the model in figure 10.1 in the 25 to 75 meV region. However, the librations are in a rather softer potential that is outside the scope of the isolated model shown figure 10.1. Essentially, an analysis using *ab initio* methods with this model is only of value in establishing that the major spectral features below 20 meV in part **(b)** of figure 10.3 are due to NH_4^+ librational motions. In contrast, the model used for MD simulations, the potential-energy landscape for rotational dynamics is determined by the non-bonding potentials of the cation with several surrounding molecules, and is expected to give a reasonable approximation to the INS spectrum below 20 meV. The simulated spectra of angular frequencies in part **(a)** of figure 10.3 are shown per cation, and the maxima and shoulders can be represented by 2 groups centered at approximately 12 and 17 meV. These two energies compares reasonably well with the INS experimental data (part **(b)** in figure 10.3) in which peaks arise at 9 and 14 meV, despite the limitations of the model and considering the difference between the simulation and experimental temperatures. On the addition of filler, the spectral intensity in the low-energy part of the experimental data shifts to lower frequency with a noticeable reduction of the splitting between the two main features, reflecting a general softening and reduction in the range of NH_4^+ rotational potentials.

In order to extract more information from the quasielastic spectra we need to connect the rotational barriers determined from the librational motions to the more diffusive rotational dynamics. Animation of the trajectory of the simulation shows typically one- or twofold coordination of the cations and we can simplify our discussion by restricting our analysis to cations in environments of approximately 3-fold symmetry.

10.6 Extrapolation of barrier heights

Within these constraints we can calculate a barrier height from a given librational energy using a rotational potential energy of the form:

$$\mathcal{H} = -\frac{\hbar}{2I}\frac{\partial^2}{\partial\phi^2} + V\left(\phi\right), \tag{10.2}$$

where I is the moment of inertia for rotation of the NH_4^+ ion around one of its 3-fold axes. $V(\phi)$ is determined as the potential that gives the required difference between the eigenvalues: 9 and 14 meV. These barriers are 21 and 42 meV respectively, the lower barrier comparing rather well with the limited temperature-dependence data from the quasielastic scattering measurements (figure 10.4), assuming an Arrhenius-like temperature dependence $\tau = \tau_0 \exp(E_a/kT)$. In the graph E_1 is fitted to the data of the pure electrolyte using the intercept with the y-axis as the only variable. This intercept is a measure of the inverse attempt frequency τ_0, and we will assume that this value is valid for all NH_4^+ ions in the sample, which allows us to estimate the quasielastic broadening that would correspond the higher frequency librational peak at around 14 meV in part **(b)** of figure 10.3. The line E_2 in figure 10.4 connects the attempt frequency and the rotational barrier of 42 meV to the relaxation time τ_2 in the temperature range probed by our experiments. This range is $144 < \tau_2 < 324$ ps, and the corresponding quasi-elastic broadening would fall well within the resolution functions of both of the instruments used. The observed librational spectra and the MD simulation are thus both consistent with the presence of 2 approximate groups of ammonium ion environments, both groups being visited by all ammonium ions over a timescale of 10s of picoseconds. Addition of nanoparticles reduces the rotational barrier of the more hindered environments making the two groups of environments more similar to each other.

10.7 Conclusions

The present work is entirely concerned with using the local rotational dynamics of an ammonium ion in the environment of ether oxygens of diglyme molecules and the iodide to probe the effects of nanoparticles on the local interactions. We obtain a consistent picture from the quasielastic spectra, librational spectra and molecular dynamics simulations. The ammonium ion environments evolve with time and can be classified into two groups: more and less hindered. Addition of nanoparticles has little effect on the less hindered environments, but reduces the barrier to rotation for the more hindered environments. Whilst rotational and librational dynamics are not a direct measure of cation mobility in polymer electrolytes, they do reflect a reduction of the interaction between the cation and the ether oxygens on the addition of nanoparticles, which is entirely consistent with the observed increase in conductivity in the polymeric system. Given the information from this work it might now be possible to separate the translation and rotation motion of NH_4^+ ions in quasielastic spectrum of the fully deuterated polymer.

The main difficulty of the current work has been the lack of structural data and the inherently non-crystalline nature of these systems, which restricts the performance of the model. The agreement of the MD simulation with the observed QENS spectrum could be improved by adjustment of charges and force-field parameters, but this goes beyond the aim of the current work, which tries to elucidate a more general model. Importantly however, there is rather good consistency with the librational spectra that reflect local interactions, which are the main concern of the current study. Whilst we do not enter a detailed analysis of the stretching parameter, (β), it is interesting to note that it decreases significantly on addition of the filler. This is again consistent with an increase in the range of relaxation processes that fall into the time-window that is accessible to the QENS experiment as more hindered environments soften on addition of the filler. This overall consistency illustrates that even in the absence of reliable structural information, MD simulations using approximate models can lead to a good understanding of the changes in dynamics when nanoparticles are added.

Acknowledgement

We are grateful to FOM for financial support (in the TFF program 97TF18) of L.v.E., to A.J. Ramirez-Cuesta, M.A. Adams and F. Fernandez-Alonso from ISIS RAL (UK) for help and advice with the neutron scattering experiments, to the ILL (France) for awarded beam time and to NWO for financing the experiment at Isis.

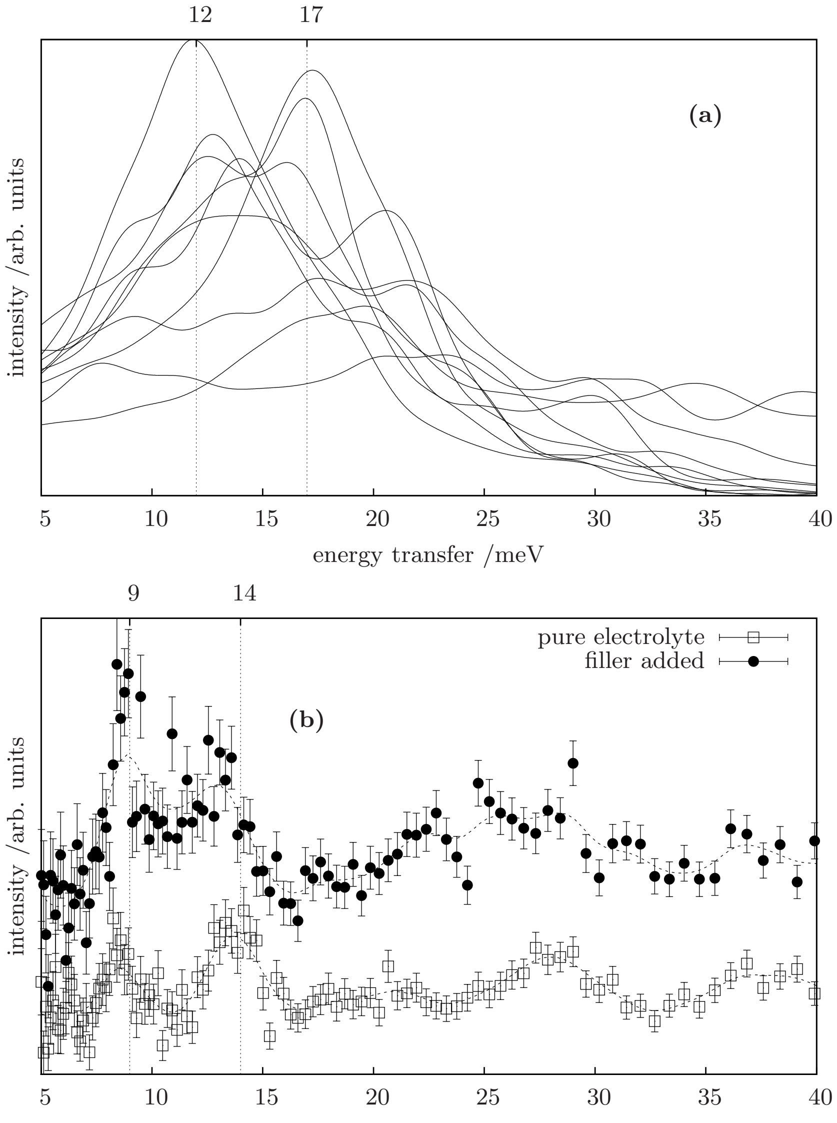

Figure 10.3: Calculated **(a)** and observed **(b)** librational spectra of the cations. **(a)** shows the librational spectra calculated for each of the 10 cations in the model separately, as derived from the simulation of pure electrolyte. Considering the limited number of cations, the cations can be assigned to two groups (12 and 17 meV) that can be compared with the data in **(b)**. The two peaks in the observed spectra around 9 and 14 meV redistribute their intensity when the filler is added and shift slightly towards each other (dashed lines are merely a guide to the eye).

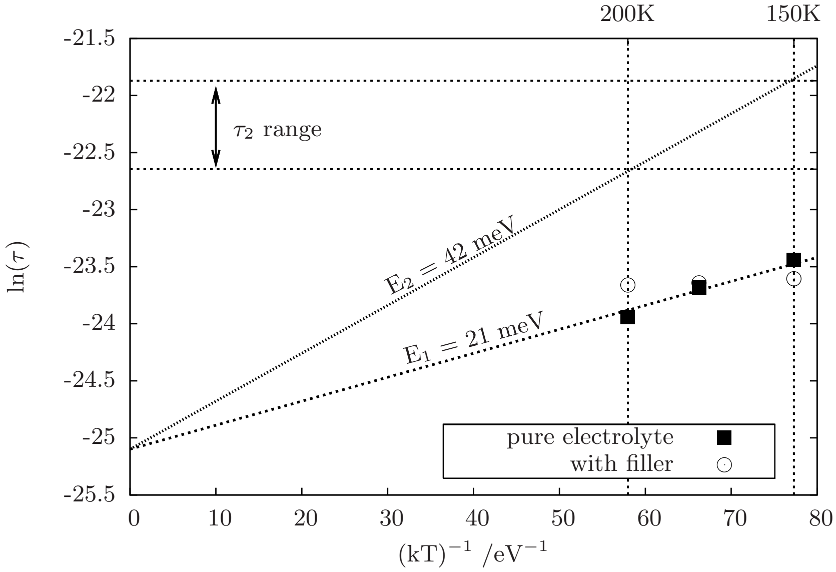

Figure 10.4: Arrhenius plot of the QENS data and estimated activation energies from INS spectra. Starting from the y-axis intercept of E_1, an estimation can be made of the relaxation times typical of the high barrier E_2: the horizontal dotted lines mark the region of relaxation times τ_2 for the temperature range of the experiments. These dynamics are too slow to be probed by the instruments used.

Chapter 11

Conclusions

In this chapter we report of the conclusions that we could draw on either of the two subjects of this thesis: conductivity and dynamics of (semi-) conducting polymers and polymer electrolytes. When these materials are applied in respectively solar cells and batteries, their molecular structure will be either amorphous of poorly crystalline, due to both static and dynamics disorder.

In solar cells based on π-conjugated polymers, the polymer can be functionalised to optimize its light harvesting performance and after dissociation of the exciton, it will act as a charge carrier transport medium. The transport of either the exciton or the polaron will be hindered by the molecular deformations in its vicinity and these deformations in turn can be static or dynamically induced by the quasi particle itself or the ambient temperature dynamics. Furthermore, we can expect the functionalisation of polymer backbone to impede proper crystallisation and hinder the transport as well. Similarly, in batteries with polymer electrolytes the crystallinity will be strongly distorted by the introduction of $\mathrm{TiO_2}$ nanoparticles.

From a scientific point of view, the poor crystallinity will complicate the investigation of the molecular structure. Our aim in general was to investigate the conductivity in terms of the interactions in these materials on a local molecular scale. From these investigations we derive a local structure and local dynamics by combining neutron scattering experiments with numerical methods. The applicability of this indirect method of determining local structure is tested starting from known structures. For bithiophene we found one example where the discrepancy of a particular part of the spectrum ($\Delta E > 600\mathrm{cm}^{-1}$) can be explained by assuming a certain amount of disorder in the sample. However, the most recent calculations using plane wave DFT show that the same discrepancy can be removed by altering the k-point scheme in the calculation. Although the spectral agreement is excellent, recently published IR spectra contradict these calculations in favour of our disorder hypothesis. This particular case illustrates the care that is required in understanding the origin of detailed spectral changes.

11.1 Conducting polymers

The charge transfer in conducting polymers is strongly dependent on the molecular conformation and in general the inter-ring torsional deformation has been held largely responsible for reduced transfer rates. From our investigations, however, we conclude that the electron-phonon coupling in these molecules should be assigned to a combination of normal modes, rather than any of the $3N-6$ fundamental normal modes specifically. We have performed DFT calculations of INS spectra of bithiophene to show the spectral sensitivity to this specific deformation coordinate, even though it is itself not a fundamental mode of vibration of the molecule. Using this sensitivity, we can confirm the planarity of bithiophene in the crystal structure by DFT calculation of the INS spectrum (200−550 cm^{-1}) on a single isolated molecule. We continued to investigate the effect of the actual normal mode deformations on the charge transfer and find that the strong dependence of the charge-transfer integral can not be solely attributed to the inter-ring dihedral deformation. Many normal modes of vibration contribute to the variation in the charge-transfer integral, a measure of the charge transfer rate. We aim to correlate the intra-chain charge transfer to the molecular dynamics at ambient temperatures, via the molecular dynamic deformations.

The molecular vibrations can be calculated from DFT methods on an isolated molecule, but to describe the softer modes of vibration, the intermolecular interactions need to be taken into account. Typically, the calculated spectra underestimated the vibrational frequencies above 600 cm^{-1}. Periodic DFT calculations were done to calculated the density of states of the phonon dispersion curves, which significantly improves the spectral agreement at low energies and makes negligible difference for the modes above 600 cm^{-1}. We find bond paths in the electron density between specific molecules, and recent papers [24, 13] confirm that these paths are likely to be responsible for intermolecular charge transfer in polythiophene. With increasing oligomer length, the energy gain of the delocalized orbitals overcomes the steric hindrance and forces the molecule to a planar conformation.

Both bithiophene and polythiophene crystal structures were derived in literature from restricted XRD data and a fractional amount of disorder (15 % *cis* monomer orientation) was reported to refine the structure of bithiophene [40]. In the spectral region of the INS data above 600 cm^{-1} we find improved agreement, when assuming a *cis*-like orientation of consecutive thiophene ring, and these finding seem to suggest an amount of static disorder in the crystal. In the polymer, the crystal periodicity combined with the *cis* conformation introduces a strain that can be released by moving away from either restriction. We have investigated a non-periodic quasi-polymer of 20 thiophene units, that forms a helical structure when implying the *cis* conformation, and found a quite remarkable spectral spectral correspondence of this rather restricted model. Further investigations of the disorder in these materials would greatly benefit from structural information at temperatures comparable to the INS experiments and DFT calculations.

A correct description of the modes above 600 cm^{-1} would not only clarify the apparent existence of a certain amount of disorder, but would also be related to the charge transfer more directly. The normal modes in this energy region concern large hydrogen displacements out of the plane of its molecule. We recall that we found bond paths in the electron density of our DFT calculation connecting a hydrogen atom to a carbon atom on the neighbouring molecule, and that this connection is largely responsible for intermolecular charge transfer. The out-of-plane normal modes can be expected to have a major impact on this charge transfer.

Returning to the intra-molecular charge transfer, we have determined the molecular dynamics including anharmonicities due to crystal packing and taking into account the approximate thermodynamic population of states, by molecular dynamics simulations. The corresponding force-field was adapted by DFT derived potentials and the resulting dynamics showed an improved agreement with the INS spectrum. From this simulation trajectory a subset of non-equilibrium molecular conformations was extracted that served to calculate the charge-transfer integral. By Fourier transformation we compare the frequency dependence of the charge-transfer integral to the observed spectrum and found that only certain vibrational modes couple to the charge transfer. The analysis needs to be taken further to polythiophene, in order to find the coupling of intramolecular charge transfer in the polymer. The Fourier transform of the charge-transfer integral would benefit from more sampling. To relate its main features back to specific vibrational modes, the spectral agreement between the MD and observed spectrum can be improved, by further adaptation of the force-field parameters (via DFT). Alternatively, it would be of interest to perform the molecular dynamics simulation by DFT methods and investigate the correlations of charge transfer fluctuations with the evolution of certain coordinates in the simulation trajectory. In this way, one may avoid the rather involved adaptation of the force-field to accomplish the spectral agreement that is required when assigning the spectral features of the charge-transfer integral to specific overtones or combinations.

11.2 Polymer electrolytes

Several authors have reported on the effect of titanium dioxide nanoparticles on the ionic conductivity in polymer electrolytes, but the mechanism by which the increase in conductivity (several orders of magnitude) can be explained is still under debate. Different papers have been published on trends in the conductivity and in the increase of conductivity, by preparation methods, choice of materials and particle size distribution, but from these trends no clear picture emerges that explains the phenomenon, though one may conclude that the effect is of a more general nature.

Therefore, we have investigated the effect on an atomic scale by studying a model system that contains the basic components of a polymer electrolyte. We have performed INS and QENS measurements on this model system which we compare with DFT calculations and MD simulations. By complementing the measurements with computations we study the effect on a local (atomic) scale. To enable accurate calculations the typical polymer PEO was substituted with its oligomer diglyme, which is the shortest section of the polymer that still contains the coordination properties of polymer on the local scale that was studied. The local scale of the dynamics was imposed by performing the experiments below room temperature, so that the diffusional dynamics in the model polymer electrolyte were largely suppressed.

The experimental INS spectrum of the model polymer electrolyte was reproduced by DFT calculations and the calculations show a marked sensitivity to the conformation of the diglyme folded around the lithium cation. Both the INS and QENS experiments, reporting the femtosecond and picosecond timescale, respectively, showed that the addition of nanoparticles hardly influences the diglyme dynamics. From this observation, combined with the spectral sensitivity to conformational changes, we conclude that the polymer backbone is, on average, not changed by the nanoparticles.

We then change the model system by deuterating the diglyme and substituting the lithium salt with ammonium iodide. Incoherent neutron scattering reports only the dynamics of the model system via the hydrogens and we thus probe mostly the cation dynamics in such a system. The INS experiments reveal a softening of the local potential energy landscape of the cation upon addition of nanoparticles. We have avoided to incorporate a (part of) the nanoparticle in our DFT calculations, since its properties and the dispersion of these properties are not known to us at the level suitable for our calculations at the atomic scale. Instead, we have mimicked the effect it could have on the diglyme-cation cluster in our calculations, by removing the charge of the model. Within the limitations of the spectral quality of our experiment, the observed trend upon addition of the nanoparticle is reproduced in our calculation by removing the charge of the model. The geometry relaxation prior to the calculation of the vibrational spectrum, showed a slight increase of diglyme-cation coordination distance, in accordance with the smoothing of the potential energy landscape as reported by the experiments.

Molecular dynamics simulations on the model electrolyte were performed on an amorphous supercell to investigate the rotational diffusion of the ammonium cation at the finite temperature of the QENS experiments. The amorphous cell was selected as the lowest energy structure from a set of ten generated structures, but it should be noted that it is one of many possible structures that can occur in the experimental conditions. The librational modes of the ammonium cations calculated from the MD simulations show a marked grouping that resembles the librational modes as observed in the INS spectrum of the electrolyte. Using the experimental peak positions of the librational modes, the temperature dependence of rotational diffusion can be estimated, once the barrier height is estimated from these librational energies. Of one of these two librational modes, we measured the diffusional component at different temperatures, and it corresponds rather well with the estimated temperature dependence. Of the other librational mode (at higher energy) the diffusional equivalent can not be probed due to the instrumental resolution of the spectrometer. Upon addition of the nanoparticles the observed librational peaks redistribute their energies and shift toward each other. Translating this trend to rotational diffusion, one can expect an increase in the intensity of the quasi-elastic broadening, as is confirmed by our QENS experiment upon addition of the nanoparticles.

The picture that emerges from our experiments combined with calculations is that the nanoparticle leaves the polymer backbone and the corresponding dynamics nearly unaltered, but releases the cation to some extent. In the experimental setting that we have chosen, this reveals itself as an increase in the intensity of the local rotational diffusion, which will result in an increased number of cations that contribute to the ionic conductivity at elevated temperatures.

Bibliography

[1] Directorate-General for Energy European Commission and Transport. *2003, Annual Energy and Transport Review*. 2004.

[2] F. Croce, G. B. Appetecchi, L. Persi, and B. Scrosati. *Nature*, 394:456, 1998.

[3] H. Shirakawa, E.J. Louis, A. G. MacDiarmid, C. K. Chiang, and A. J. Heeger. *J. Chem. Soc. Chem. Comm.*, 16:578, 1977.

[4] G. H. Gelinck, H. Edzer, A. Huitema, E. van Veenendaal, E. Cantatore, L. Schrijnemakers, J. B. P. H. van der Putten, T. C. T. Geuns, M. Beenhakkers, J. B. Giesbers, B.-H. Huisman, E. J. Meijer, E. Mena Benito, F. J. Touwslager, A. W. Marsman, B. J. E. van Rens, and D. M. de Leeuw. *Nature Mat.*, 3:106, 2004.

[5] N. Stingelin-Stutzmann, E. Smits, H. Wondergem, C. Tanase, P. Blom, P. Smith, and D. de Leeuw. *Nature Mat.*, 4:601, 2005.

[6] B. O'Regan and M. Grätzel. *Nature*, 353:737, 1991.

[7] P. Ravirajan, S. A. Haque, J. R. Durrant, D. Poplavskyy, D. D. C. Bradley, and J. Nelson. *J. Appl. Phys.*, 95:1473, 2004.

[8] C. Y. Kwong, W. C. H. Choy, A. B. Djurišić, P. C. Chui, and K. W. Cheng. *Nanotechnology*, 15:1156, 2004.

[9] S. Karabunarliev E. R. Bittner, J. G. Santon Ramon. *ArXiv. Cond. Mat. Phys*, arXiv:cond-mat/0506065, 2005.

[10] M. Granström, K. Petritsch, A. C. Arias, A. Lux, M. R. Andersson, and R. H. Friend. *Nature*, 395:257, 1998.

[11] H. Shirakawa. *Nobel Lectures Chemistry*, 1996-2000:453, 2003.

[12] K. D. Meisel, H. Vocks, and P. A. Bobbert. Polarons in semiconducting polymers: Study within an extended holstein model. *Phys. Rev. B*, 71(20):205206, 2005.

[13] A. Ferretti, A. Ruini, G. Bussi, and E. Molinari. *Phys. Rev. B*, 69:205205, 2004.

[14] F. C. Grozema, P. T. van Duijnen, Y. A. Berlin, M. A. Ratner, and L. D. A. Siebbeles. *J. Phys. Chem. B*, 106:7791, 2002.

[15] R. F. W. Bader. *Atoms in Molecules, a Quantum Theory*. Clarendon Press, Oxford, 1990.

[16] D. Brouillette, D. E. Irish, N. J. Taylor, G. Perron, M. Odziemkowski, and J. E. Desnoyers. *Phys. Chem. Chem. Phys*, 4:6063, 2002.

[17] E. B. Wilson, J. C. Decius, and P. C. Cross. *Molecular Vibrations*. McGraw-Hill, New York, 1955.

[18] L. van Hove. *Phys. Rev.*, 95:249, 1954.

[19] G. L. Squires. *Introduction to the theory of thermal neutron scattering*. Dover, New York, 1978.

[20] P. Hohenberg and W. Kohn. *Phys. Rev.*, 136:B864, 1964.

[21] W. Kohn and L.J. Sham. *Phys. Rev.*, 140:A1133, 1965.

[22] A. D. Becke. *Phys. Rev. A*, 38:3098, 1988.

[23] J. L. Brédas, J. P. Calbert, D. A. da Silva Filho, and J. Cornil. *Proc. Nat. Ac. Sci.*, 99:5804, 2002.

[24] P. Puschnig and C. Ambrosch-Draxl. *Synth. Met.*, 119:245, 2001.

[25] T. Siegrist, C. Kloc, R. A. Laudise, H. E. Katz, and R. C. Haddon. *Adv. Mat.*, 10:379, 1998.

[26] Z. G. Yu, D. L. Smith, A. Saxena, R. L. Martin, and A. R. Bishop. *Phys. Rev. Lett.*, 84:721, 2000.

[27] F. C. Grozema, P. T. Van Duijnen, and L. D. A. Siebbeles. *Phys. Rev. Lett.*, subm.

[28] G.J. Kearley, M.R. Johnson, M. Plazanet, and E. Suard. *J. Chem. Phys.*, 115, 2001.

[29] A. D. Esposti and F. Zerbetto. *J. Phys. Chem. A*, 101:7283, 1997.

[30] B. Delley. *J. Chem. Phys.*, 92:508, 1990.

[31] M. Pelletier and F. Brisse. *Acta Crystallogr. C*, 50:1942, 1994.

[32] G.J. Kearley. *Nucl. Instr. Meth. Phys. Res. A*, 53:354, 1995.

[33] M. Plazanet, M. R. Johnson, J. D. Gale, T. Yildirim, G. J. Kearley, M. T. Fernández-Díaz, D. Sánchez-Portal, E. Artacho, J. M. Soler, P. Ordejón, A. Garcia, and H. P. Trommsdorff. *J. Chem. Phys*, 261:189, 2000.

[34] G. Kresse, J. Furthmuller. Software VASP, and Vienna 1999. *Phys. Rev. B*, 54:169, 1996.

[35] B. Delley. *J. Chem. Phys*, 113:7756, 2000.

[36] K. Parlinski. *Am. Inst. Phys. Conf. Proc.*, 479:121, 1999.

[37] L. van Eijck, L. D. A. Siebbeles, F. C. Grozema, I. M. de Schepper, and G. J. Kearley. *App. Phys. A*, 74:S694, 2002.

[38] H. Sun. *J. Phys. Chem. B*, 102:7338, 1998.

[39] http://www.nas.nasa.gov/Software/FAST/.

[40] P. A. Chaloner, S. R. Gunatungaand, and P. B. Hitchcock. *Acta Crystallogr. C*, 50:1941, 1994.

[41] C. X. Cui and M. Kertesz. *Phys. Rev. B*, 40:9661, 1989.

[42] J. P. Perdew, K. Burke, and M. Ernzerhof. *Phys. Rev. Lett.*, 77:3865, 1996.

[43] P. Hermet, J.-L. Bantignies, A. Rahmani, J.-L. Sauvajol, M. R. Johnson, and F. Serein. *J. Phys. Chem. A*, 109:1684, 2005.

[44] E. R. Johnson, R. A. Wolkow, and G. A. DiLabio. *Chem. Phys. Lett.*, 394:334, 2004.

[45] P. Hermet, J.-L. Bantignies, A. Rahmani, J.-L. Sauvajol, and M. R. Johnson. *J. Phys. Cond. Matt.*, 16:7385, 2004.

[46] S. Brükner and W. Porzio. *MakroMol. Chem.*, 189:961, 1988.

[47] J. W. Ponder. Tinker: Software tools for molecular design, 4.2.

[48] N. L. Allinger, Y. H. Yuh, and J.-H. Lii. *Chem. Soc.*, 111:8551, 1989.

[49] J. P. Perdew, K. Burke, and Y. Wang. *Phys. Rev. B*, 54:16533, 1996.

[50] http://www.accelrys.com.

[51] J. P. Aime, F. Bargain, M. Schott, H. Eckhardt, G. G. Miller, and R. L. Elsenbaumer. *Phys. Rev. Lett.*, 62:55, 1989.

[52] K. P. R. Nilsson, M. R. Andersson, and O. Inganäs. *J. Phys. Condens. Matt.*, 14:10011, 2002.

[53] A. M. Cristie, S. J. Lilley, E. Staunton, Y. G. Andreev, and P. G. Bruce. *Nature*, 433:50, 2005.

[54] L. van Eijck, M. R. Johnson, and G. J. Kearley. *J. Phys. Chem. A*, 107:8980, 2003.

[55] http://www.isis.rl.ac.uk/molecularspectroscopy/tosca/.

[56] E.A. Silinsh. *Organic Molecular Crystals*. Springer, Berlin, 1980.

[57] G. Te Velde, F. M. Bickelhaupt, E. J. Baerends, C. Fonseca Guerra, S. J. A. Van Gisbergen, J. G. Snijders, and T. Ziegler. *J. Comp. Chem.*, 22:931, 2001.

[58] J. Cornil, D. Beljonne, J.-P. Calbert, and J.-L. Brédas. *Adv. Mat.*, 13:1053, 2001.

[59] M. Pavanello, S. Bubin, M. Molski, and L. Adamowicz. *J. Chem. Phys.*, 123:104306, 2005.

[60] M. J. Frisch, G. W. Trucks, and H. B. Schlegel et al. Gaussian 98, 1998.

[61] M. W. Schmidt, K. K. Baldridge, J. A. Boatz, S. T. Elbert, M. S. Gordon, J. J. Jensen, S. Koseki, N. Matsunaga, K. A. Nguyen, S. Su, T. L. Windus, M. Dupuis, and J. A. Montgomery. *J. Comput. Chem.*, 14:1347, 1993.

[62] A. D. Becke. *J. Chem. Phys.*, 98:5648.

[63] W. J. Hehre, R. Ditchfield, and J. A. Pople. *J. Chem. Phys.*, 56:2257, 1972.

[64] K. Drew, G. Girishkumar, K. Vinodgopal, and Prashant V. Kamat. *J. Phys. Chem. B*, 109:11851, 2005.

[65] W. Krawiec, L. G. Scalon Jr., J. P. Fellner, R. A. Vaia, S. Vasudevan, and E. P. Giannelis. *J. Power Sources*, 54:310, 1995.

[66] M. Marcinek, A. Bac, P. Lipka, A. Zalewska, G. Żukowska, R. Borkowska, and W. Wieczorek. *J. Phys. Chem. B*, 104:11088, 2000.

[67] C. Karlsson, A. S. Best, J. Swenson, W. S. Howells, and L. Björsson. *J. Chem. Phys.*, 118:4206, 2003.

[68] H. Kasemägi, M. Klintenberg, A. Aabloo, and J. O. Thomas. *Solid State Ionics*, 147:367, 2002.

[69] O. Borodin, G. D. Smith, R. Bandyopadhyaya, P. Redfern, and L. A. Curtiss. *Modelling Simul. Mater. Sci. Eng.*, 12:S73, 2004.

[70] A.S. Best, J. Adebahr, P. Jacobsson, D. R. MacFarlane, and M. Forsyth. *Macromolecules*, 34:4549, 2001.

[71] J. Grondin, L. Ducasse, J-L Bruneel, L. Servant, and J-C. Lassègues. *Solid State Ionics*, 166:441, 2004.

[72] L. Edman. *J. Phys. Chem. B*, 104:7254, 2000.

[73] W. A. Henderson, N. R. Brooks, W. W. Brennessel, and V. G. Young Jr. *J. Phys. Chem. A*, 108:225, 2004.

[74] G. Mao, M. L. Saboungi, D. L. Price, M. B. Armand, and W. S. Howells. *Phys. Rev. Letters*, 84:5536, 2000.

[75] F.M. Gray. *Polymer Electrolytes.* VCH Publisher Inc., New York, 1997.

[76] M. Forsyth, D. R. MacFarlane, A. S. Best, J. Adebahr, P. Jacobsson, and A. J. Hill. *Solid State Ionics*, 147:203, 2002.

[77] J. Adebahr, A. S. Best, N. Byrne, P. Jacobsson, D. R. MacFarlane, and M. Forsyth. *Phys. Chem. Chem. Phys*, 5:720, 2003.

[78] P. Johansson and P Jacobsson. *Solid State Ionics*, 170:73, 2004.

[79] G.J. Kearley, P. Johansson, R.G. Delaplane, and J. Lindgren. *Solid State Ionics*, 147:237, 2002.

[80] C. P. Rhodes and R. Frech. *Macromolecules*, 34:2660, 2001.

[81] G.J. Kearley, L. van Eijck, and A.A. van Well. *Physica B*, 350:E987, 2004.

[82] F.Croce, L. Persi, B. Scrosati, F. Serraino-Fiory, E. Plichta, M. A., and Hendrickson. *Electrochimica Acta*, 46:2457, 2001.

[83] P. Mustarelli, C. Capiglia, E. Quartarone, C. Tomasi, and P. Ferloni. *Phys. Rev. B*, 60:7228, 1999.

[84] L. van Eijck, A. S. Best, and G. J. Kearley. *Macromolecules*, 37:9591, 2004.

[85] G. Williams and D. C. Watts. *Trans. Faraday Soc.*, 66:80, 1970.

[86] R. Bergman. *J. Appl. Phys.*, 88:1356, 2000.

[87] V. K. Malinovski, V. N. Novikov, and A. P. Sokolov. *Physics Letters A*, 153:63, 1991.

[88] G. R. Kneller, V. Keiner, M. Kneller, and M. Schiller. *Comp. Phys. Comm*, 91:191, 1995.

[89] M. Beé. *Quasi Elastic Neutron Scattering, Principle and Applications.* IOP Publishing Ltd, Bristol, 1988.

[90] E. Fratini, A. Faraone, P. Baglioni, M.-C. Bellissent-Funel, and S.-H. Chen. *Phys. A*, 304:1, 2002.

[91] J. Colmenero, A. Arbe, A. Alegría, M. Monkenbusch, and D. Richter. *J. Phys. Cond. Matt.*, 11:A363, 1999.

Appendices

Appendix A

Summary

In this thesis we study the local dynamics of polymers, together with the coupling of these dynamics to the dynamics of electrical charge. This work is related to batteries and solar cells, both of which can be fabricated using polymers. The use of conventional solar cells is hindered by the expensive production proceesses that are inherent to solid state semiconductor technology. An economical alternative to the conventional solar cell is on that is based on polymers. Moreover, the processability and applicability of polymer solar cells is larger due to the ease with which one can tune the material properties of polymers. The energy conversion yield of this type of solar cells is limited by the low electrical conductivity of the polymer via static and dynamical disorder of the polymer chain. In part I of this thesis the coupling of the conductivity with the local molecular dynamics is investigated. Also, we investigate if the local static conformation can be derived from the vibrational spectrum in this type of material that often has a non-crystalline ordering in applications like solar cells.

The electrolyte of a battery is situated between the two electrodes and enables an internal ionic charge transport. When using polymer electrolytes the ionic conductivity is too low for most battery applications. The addition of a small amount of titaniumdioxide nano-crystalline particles to the polymer electrolytes enhances its conductivity by a few orders of magnitude. The mechanism behind this increase is still poorly understood, and in part II of this thesis we present our investigations where we study the local interactions on a molecular scale of a polymer electrolyte and the effect that nanoparticles have on these interactions.

The materials that we have chosen, are model systems of which the properties on a local molecular scale are similar to the properties of the materials in their applications (hole conductor in solar cells and electrolyte polymer in batteries). Additionally, the model systems are chosen such that our research can be done with quantum mechanical density functional theory (DFT), molecular dynamics simulations and neutron scattering techniques: inelastic (INS) and quasi-elastic (QENS).

Conducting polymers

From our research we conclude that the local conformation of the molecule can be derived using the combination of DFT calculations with INS experiments. Based on this combined analysis we propose a significant amount of $trans - cis$ disorder in the sample that we investigated. In terms of electron-phonon coupling in these materials we study the effect of vibrational normal modes on the conductivity and find that the conductivity is not directly related to any specific normal mode of vibration. Based on these findings we calculated the conductivity as a function of time from a molecular dynamics simulation, thereby including the assembled dynamics of a cluster of molecules and the resulting anharmonic effects. The classical thermodynamic distribution of normal modes is now taken into account and it enables us to calculate the intermolecular conductivity. The Fourier transform of the time-dependent conductivity $\mathcal{F}(J)$ shows some spectral features that can be assigned to a combination of normal modes (or higher harmonics), rather than any of the individual normal modes. The correlation of the $\mathcal{F}(J)$ to a combination or higher harmonics awaits a better spectral correspondence of the simulation with the DFT calculations.

Polymer electrolytes

The titanium dioxide nanocrystalline particle that enhances the conductivity of the polymer electrolyte with several orders of magnitude is not included in the calculations on the electrolyte polymer or cation. To make the calculations on the model system feasible, we substituted the polymer with its oligomer and for the study of the cation dynamics, the conventional lithium cation is replaced by ammonium (NH_4^+) and the oligomer is deuterated. From our investigations on the oligomer dynamics we find that the DFT calculations of a vibrational spectrum are remarkably sensitive to the conformation of the molecule and of two local minimum structures the vibrational spectrum of the lowest energy structure corresponds best with the observed INS spectrum, even though these structures are quite similar. The calculation model of one cation that is surrounded by one oligomer is sufficient to describe the main features of the observed INS spectrum. The observed INS spectrum does change significantly upon the addition of nanoparticles and the same effect is observed for the QENS experiments, where we study the picosecond timescale dynamics. The study of the cation dynamics is hindered by the poor quality of the INS spectrum, although the spectra reveal a shift of the intensity upon addition of the nanoparticles. The potential energy landscape of the cation softens, though the oligomer conformation around the cation was found to remain intact. Here too, the calculation model of one oligomer with one cation (ammonium) is sufficient to obtain a reasonable spectral correspondence with the observed INS spectrum. The trend of the intensity shift in the observed spectra upon addition of the nanoparticles can be reproduced in the DFT calculations by removing the charge ($+1e$) from the model, in correspondence with the hypothesis that the potential energy landscape of the cation softens. In order to study the effect of the nanoparticles on the dynamics of the cation on a picosecond timescale, we performed QENS experiments at such temperatures that the observed dynamics of the cation is mostly rotational diffusion. Remarkably, the addition of the nanoparticles increases the intensity of the quasi-elastic signal, but it hardly effects the characteristic correlation time for diffusion. The rotional diffusion of the cation also appears from molecular dynamics simulations, from which we also calculate the librational spectrum. This librational spectrum show a good correspondence with the observed INS spectrum, in which the intensity of the librational modes shift upon addition of the nanoparticles. Using these librational modes, we determine the activation energy for rotational diffusion. Of the two barriers for diffusion only one appears to be observable with the instrumental setting of our QENS experiments and the increase of the quasi-elastic intensity corresponds to the shift in intensity of the INS librational modes. The picture that emerges from the findings is that only a fraction of the cations contributes to the conductivity of the polymer electrolyte and that the addition of nanocrystalline titaniumdioxide particles enlarges this fraction without influencing the local conformation of the polymer or its corresponding dynamics.

The methods used in this research were applied to conducting polymers for solar cells and to polymer electrolytes for batteries. The applicability of the method was demonstrated, but is not limited to these two subjects. Polymer systems typically show poor crystallinity which complicates the study on a molecular scale, and by making use of the methods described in this thesis one can investigate such systems on a local molecular scale.

Bijlage B

Samenvatting

In dit proefschrift wordt de lokale dynamica van polymeren bestudeerd en de koppeling van die dynamica met de dynamica van elektrische lading. Het onderzoek is gerelateerd aan batterijen en zonnecellen die beide gefabriceerd kunnen worden met polymeren.

Het gebruik van conventionele zonnecellen wordt gehinderd door het kostbare productieproces dat inherent is aan vastestofhalfgeleidertechnologie. Een goedkoper alternatief voor de conventionele zonnecel is een zonnecel die gebaseerd is op polymeren. Bovendien is de verwerkbaarheid en het toepassingsgebied van polymeerzonnecellen groter door de materiaaleigenschappen van polymeren. De energieopbrengst van dit type zonnecellen wordt onder meer beperkt door de lage elektrische geleiding van het polymeer via de statische en dynamische wanorde van de polymeerketen. In deel I van dit proefschrift wordt de koppeling van de geleiding met de lokale moleculaire dynamica onderzocht en tevens wordt gekeken in welke mate de lokale statische conformatie kan worden herleid uit het vibratiespectrum in dit type materiaal dat vaak niet kristallijn oriënteert in toepassingen als zonnecellen.

Tussen de elektroden van een batterij zit het elektrolyt dat de inwendige ionische geleiding bewerkstelligt. In het geval van een polymeerelektrolyt is de geleiding voor veel batterijtoepassingen te laag. Wanneer er een kleine hoeveelheid nanokristallijn titaniumdioxide wordt vermengd in het polymeerelektrolyt, dan zal de geleiding met enkele ordes van grootte toenemen. Het mechanisme dat verantwoordelijk is voor het effect van geleidingstoename is nog niet eenduidig verklaard en in deel II van dit proefschrift wordt het onderzoek gepresenteerd waarin de lokale interacties worden bestudeerd van het electrolyt op moleculair schaal en het effect van de nanodeeltjes op die interacties.

De materialen waarmee gewerkt is, zijn modelsystemen die op een lokale moleculaire schaal vergelijkbare eigenschappen bezitten als de polymeren in de respectievelijke toepassingen (gatengeleider in zonnecellen en elektrolytpolymeer in batterijen). De modelsystemen zijn bovendien zo gekozen dat het onderzoek gedaan kan worden met behulp van kwantummechanische dichtheidsfunctionaal theorie (DFT), moleculaire dynamica simulaties en neutronenverstrooiïngstechnieken: inelastisch (INS) en quasielastisch (QENS).

Geleidende polymeren

Uit het onderzoek blijkt dat met behulp van de combinatie DFT en INS de lokale conformatie van het molecuul te herleiden is en naar aanleiding van deze combinatie van berekeningen en metingen stellen we dat het proefmateriaal waaraan gewerkt is een significante hoeveelheid $trans - cis$ wanorde bevat. In het kader van elektron-fonon koppeling in dit type materiaal is het effect bestudeerd van verschillende vibratie-modi op de geleiding en blijkt de geleiding niet direct gekoppeld te zijn aan één van de normaal modi van vibratie. Naar aanleiding van dit resultaat is de geleiding als functie van tijd berekend uit een moleculaire dynamica simulatie, waardoor de samengestelde dynamica van een cluster moleculen inbegrepen is, inclusief de resulterende anharmonische effecten. Hiermee is tevens de klassieke thermodynamische distributie van normaal modi inbegrepen en kan de intermoleculaire geleiding berekend worden. De Fourier getransformeerde van de tijdsafhankelijke geleiding $\mathcal{F}(J)$ toont enkele spectrale karakteristieken die, vergeleken met het INS spectrum, eerder aan een combinatie van normaal modi toegekend kunnen worden dan aan één van de afzonderlinge modi. De correlatie van $\mathcal{F}(J)$ met combinaties of hogere harmonische van normaal modi uit DFT berekeningen wacht een betere spectrale overeenkomst van de simulatie met de DFT berekeningen. Anderzijds kan $\mathcal{F}(J)$ gecorreleerd worden aan interne coördinaten.

Polymeerelektrolyten

Het titaniumdioxide nanokristallijnen deeltje dat de geleiding in polymeerelektrolyten met grootteordes verhoogt, is niet meegenomen in de berekeningen aan het elektrolytpolymeer en het cation. Om de berekeningen hanteerbaar te maken is het polymeer vervangen door een oligomeer en in de studie van de cationdynamica is het conventionele cation lithium vervangen door ammonium (NH_4^+) en het oligomeer gedeutereerd. Uit het onderzoek naar de dynamica van het oligomeer blijkt dat de DFT-berekeningen van een vibratiespectrum opmerkelijk gevoelig zijn voor de conformatie van het molecuul. Van twee lokaalminimumstructuren stemt het vibratiespectrum van de structuur met de laagste energie het best overeen met het gemeten INS spectrum, hoewel de conformaties zeer veel overeenkomst vertonen. Het model van één cation dat omsloten wordt door één oligomeer is voldoende om de hoofdkarakteristieken van het gemeten spectrum te beschrijven. Het gemeten INS spectrum verandert niet significant door toevoeging van de nanodeeltjes en het zelfde effect nemen we waar bij de QENS metingen waarmee we de picosecondedynamica bestuderen. De studie naar de cationdynamica wordt gehinderd door de lage kwaliteit van het INS spectrum, hoewel duidelijk blijkt uit de metingen dat de intensiteit van het gemeten spectrum verschuift na toevoeging van de nanodeeltjes. Het potentiaallandschap van het cation wordt vlakker, terwijl gebleken is dat de conformatie van het oligomeer rondom het cation intact blijft. Ook hier blijkt het berekeningsmodel van één oligomeer met één cation (ammonium) voldoende om een redelijke spectrale overeenkomst te verkrijgen met de INS meting. De trend van de intensiteitsverschuiving in de metingen door toevoeging van de nanodeeltjes kan in de DFT berekeningen worden bewerkstelligd door de lading ($+1e$) van het model in de berekening te verwijderen, in overeenstemming met de stelling dat het potentiaallandschap van het cation vlakker wordt. Om het effect van de nanodeeltjes op de dynamica van het cation te bestuderen op de picosecondetijdschaal zijn QENS metingen verricht, waarmee bij de gekozen temperaturen vooral de rotationele diffusie van het cation gerapporteerd wordt. Met de toevoeging van de nanodeeltjes wordt, opmerkelijk, de intensiteit van het quasi-elastische signaal verhoogd en in veel mindere mate wordt de karakteristieke correlatietijd voor diffusie beïnvloed. De rotationele diffusie van het cation blijkt ook uit een moleculaire dynamica simulatie waaruit tevens het libratiespectrum berekend is. Dit libratiespectrum vertoont opmerkelijke overeenkomsten met het gemeten INS spectrum, waarin de intensiteit van de libratie-modi verschuift door toevoeging van de nanodeeltjes. Met behulp van deze libratie-modi is de activeringsenergie voor rotationele diffusie bepaald. Van de twee barrières voor diffusie blijkt slechts de laagste meetbaar in de gekozen QENS-instrumentinstellingen en het toenemen van de intensiteit van het quasi-elastische signaal in de metingen correspondeert met verschuiving van de INS libratie-modi. Het beeld dat uit deze waarnemingen ontstaat is dat slechts een fractie van de cationen bijdraagt aan de geleiding van het polymeerelektrolyt en dat het toevoegen van nanokristallijnen titaniumdioxide deeltjes deze fractie verhoogt zonder de lokale conformatie van het polymeer of de corresponderende dynamica te beïnvloeden.

De methodes die in dit onderzoek gebruikt zijn, werden toegepast op geleidende polymeren voor zonnecellen en polymeerelektrolyten voor batterijen. De toepasbaarheid van de methode is gedemonstreerd, maar is niet beperkt tot deze twee onderwerpen. Polymeer systemen hebben meestal een weinig kristallijnen structuur wat de studie op een moleculair niveau bemoeilijkt en door de methodes zoals beschreven in dit proefschrift toe te passen, kan men zulke systemen op een lokaal moleculair schaal onderzoeken.

Bijlage C

Dankwoord

Het is niet voordehand liggend om als hts'er aan een promotieonderzoek te beginnen. Omdat ik als hts'er werkzaam was op de universiteit kwam ik in contact met promovendi en het werk wat ze doen en daarmee was mijn interesse in promoveren gewekt. Uiteindelijk ben ik mede dankzij Ewout over stag gegaan en hebben Ignatz en Don het daadwerkelijk geregeld dat ik op 1 september 2001 aan mijn promotieonderzoek kon beginnen. Met Don als promotor en dagelijks begeleider begon ik aan "plastic zonnecellen", waarin we het effect van de moleculaire dynamica op de elektrische geleiding bestudeerden. De methodes die we gebruikten, konden we ook toepassen op "plastic batterijen" en zodoende hebben we het vierjarige onderzoek verspreid over deze twee milieuvriendelijke mobiele energiebronnen.
Zoals bij vele onderzoeksinstituten is de werkomgeving internationaal en bovendien is het aantal plaatsen in de wereld waar met neutronen onderzoek gedaan kan worden klein. Als promovendus ben je daardoor vaak buiten de deur om je onderzoek te doen of voor een cursus.
Het werk van promovendi wordt vaak gekenmerkt door een grote mate van specialisatie, wat met mee zich meebrengt dat het erg moeilijk is om echt samen te werken met de mensen binnen je afdeling. Tot mijn eigen verbazing zijn tóch veel van mijn vakanties of uitjes van de afgelopen jaren samen met collega's geweest en dat maakt de werksfeer vervolgens weer een stuk informeler.
Terugblikkend op de afgelopen jaren heb ik mijn horizon flink kunnen verbreden en in eerste instantie bedank ik Don daarvoor. Hij heeft niet alleen mij aangenomen als promovendus, maar heeft als dagelijks begeleider mij "het vak" geleerd en richting gegeven aan het onderzoek. Bij dat onderzoek horen publicaties, cursussen, conferenties, proposals en proper english en de wegwijs in deze wondere wetenschapswereld: dank aan Don!
Om vanuit mijn achtergrond te levellen met collega promovendi heb ik veel moeten studeren en wat daar ontzettend bij geholpen heeft, zijn de vele discussies met en geïmproviseerde examineringen van mijn medepromovendi. Marnix was vaak het kritische klankbord voor k-points en andere knelpunten en Gijs bovendien voor de krantbesprekingen en mijn koffiezetkunde. Met Adam ben ik vaak naar 't buitenland geweest voor experimenten, die ons vaak tot diep in de nacht ophielden. De ontberingen deden me denken aan een studentenontgroening, hoewel de instrument verantwoordelij-

ken Timmy Ramirez-Cuestra, Stewart Parker, Mark Adams, Felix Fernandez-Alonso, Mark Telling en John Stride ons goed geholpen hebben met onze experimenten en tijdens de discussies.
Om mijn eigen specialistische werk te plaatsen in een breder kader, is ’t enorm belangrijk om ook dit kader te verkennen en daarbij heeft zowel Alexander als Ewout mij heel veel geholpen. Meer niet dan wel gingen de gezamelijke discussies en excursies over wetenschap, hoewel onderweg altijd wel een standbeeld of theorie van de Groten der Aarde opdook.
Thuis aangekomen liep ik vaak tegen het probleem op dat je je specialisatie nou eenmaal niet kunt delen met velen. Daarom dank ik heel veel mensen, in dit kader van mijn proefschrift, voor hun geduld met mijn verworven vervreemding van echte dingen, mijn aangeleerde eigenwijsheid. In het bijzonder wil ik mijn moeder en Debbie, Bea en Thora danken, die het allemaal hebben zien gebeuren, maar er niets aan konden doen. Zij kunnen begrijpen dat een deel van die eigenwijsheid genetisch bepaald is en aangeleerd door een vader die zijn scheve schuifdeuren verklaarde met tijd-ruimte-kromming. Mede door zijn doen ben ik natuurkunde gaan studeren en helaas is hij er niet meer! Mijn lieve Yvonne heeft mij leren kennen in mijn laatste promotiejaar en zag mij dus vaak in stress en frustratie over mijn eigen werk. Heel veel dank voor je medeleven en liefde en support en kritiek!

Op allerlei manieren nog veel lof aan mensen die ik hier niet noem!

Lambert

Appendix D

Curriculum Vitae

Lambert van Eijck was born the 29th of January 1973 in Tilburg, The Netherlands. He attended the secondary school in Sprang-Capelle where he obtained his mavo diploma in 1989. After a three year electrician education at the MTS in Tilburg he started his applied physics study at the Hogeschool Eindhoven. In 1996 he obtained his bachelor degree in applied physics. He worked as a physics engineer in Nano EXperiments and Technology (NEXT) lab at the University of Technology Delft from 1997 to 1998. Starting from 1998 he worked as a second instrument responsible of the time-of-fight reflectometer at the Reactor Institute Delft of the same university, after which he started his PhD research project in 2001. The project was financed by the foundation Fundamenteel Onderzoek der Materie (FOM) in the Netherlands via the TFF program (97TF18) led by prof. dr. S. W. de Leeuw. The research was performed in the group of prof. dr. G. J. Kearley, Fundamentals Aspects of Materials and Energy (FAME), who was the supervisor and promotor of Lambert. The research project ended in 2005 and this thesis is a result of the research.

Appendix E

List of Publications

Localization of ferrocene in NaY zeolite by powder x-ray and neutron diffraction
E. Kemner, A. R. Overweg, and L. van Eijck, A. N. Fitch, E. Suard,
I. M. de Schepper and G. J. Kearley.
J. Chem. Phys. **116**, 10838 (2002).

INS as a probe of inter-monomer angles in polymers
L. van Eijck , L.D.A. Siebbeles, F.C. Grozema, I.M. de Schepper, G.J. Kearley.
Appl. Phys. A **74** [**Suppl.**], S496 (2002).

Intermolecular Interactions in Bithiophene as a Model for Polythiophene
Lambert van Eijck, Mark R. Johnson, and Gordon J. Kearley.
J. Phys. Chem. A **107**, 8980 (2003).

A quantative study of the charge-transfer between conjugated thiophene rings in vibrationally excited states
L. van Eijck, K. Senthilkumar, L.D.A. Siebbeles, G.J. Kearley.
Physica B **350**, 220 (2004).

The effect of Nanocrystalline Materials on Ionic Interactions in Polymer Electrolytes
Lambert van Eijck, Adam S. Best, and Gordon J. Kearley.
Macromolecules **37**, 9591 (2004).

Dynamics and Lithium Binding Energies of Polyelectrolytes Based on Functionalized Poly(para-phenylene terephthalamide)
F. C. Grozema, A. S. Best, L. van Eijck, J. Stride,
G. J. Kearley, S. W. de Leeuw and S. J. Picken.
J. Phys. Chem. B **109**, 7705 (2005).

Softening of the potential-energy surface in polymer electrolytes on the addition of nanoparticles
Lambert van Eijck, Adam S. Best, John Stride, Gordon J. Kearley.
Chemical Physics **317**, 282 (2005).

Glossary

2T: bithiophene

chemical structure bithiophene $[C_4SH_3]_2$ 6, 56, 70

4T: quaterthiophene

chemical structure quaterthiophene $C_{16}S_4H_{10}$ 56

6T: sexithiophene

chemical structure $C_{24}S_6H_{14}$ 56

CTI: charge-transfer integral

Off-diagonal matrix element of the Hamiltonian of the time-independent Schrödinger equation 6–8, 35, 36, 65, 69, 73

DFT: density functional theory

(see section 2.3.1) 6, 7, 12, 13, 15, 17, 22–24, 36, 44, 56, 59, 67, 69, 109, 117, 121

diglyme: di-glycol-methyl

oligomer of PEO; chemical structure $[CH_3OCH_2CH_2]_2O$ 13, 80, 83, 96, 109

FWHM: full width at half maximum

measure of the width of an arbitrarily shaped peak 29, 96

HOMO: higest occupied molecular orbital

Higest occupied molecular orbital 8, 35, 67

INS: inelastic neutron scattering

(see section 2.2) 6–8, 12, 13, 17, 37, 39, 44, 55, 58, 59, 70, 109, 117, 121

LDA: local density approximation

(see section 2.3.1) 24, 38

MD: molecular dynamics

(see section 2.3.2) 6, 12, 70, 94, 109, 110

OLED: organic light emitting diode

an organic LED is build from “organic molecules” instead of “solid state materials” like silicon 2

PEO: poly-ethyleneoxide

chemical structure poly-ethyleneoxide $[CH_2CH_2O]_n$ 11, 13, 109

PES: potential energy surface

The size of the molecule(s) determine the multidimensionality of this surface 70

pPV: poly-phenylenevinylene

chemical structure poly-phenylenevinylene $[C_8H_6]_n$ 5

pT: polythiophene

chemical structure polythiophene $[C_4SH_2]_n$ 5, 7, 56, 60, 61, 69

QENS: quasi-elastic neutron scattering

(see section 2.2) 12, 13, 27, 31, 70, 94, 109, 117, 121

SANS: small angle neutron scattering

(see section 2.2) 62

SCF: self consistent field

(see section 2.3.1) 23

TOF: time-of-flight

The kinetic energy of the particle is determined by its travel time over a defined path. 27, 28